DUNE Phase II:
Scientific Opportunities, Detector Concepts, Technological Solutions

The DUNE Collaboration[*]

August 26, 2024

[*]Editors: Sowjanya Gollapinni, Anne Heavey, Stefan Söldner-Rembold, Michel Sorel

Authors

A. Abed Abud,[35] B. Abi,[156] R. Acciarri,[66] M. A. Acero,[12] M. R. Adames,[193] G. Adamov,[72] M. Adamowski,[66] D. Adams,[20] M. Adinolfi,[19] C. Adriano,[30] A. Aduszkiewicz,[81] J. Aguilar,[126] F. Akbar,[175] K. Allison,[43] S. Alonso Monsalve,[35] M. Alrashed,[119] A. Alton,[13] R. Alvarez,[39] T. Alves,[88] H. Amar,[84] P. Amedo,[85, 84] J. Anderson,[8] C. Andreopoulos,[128] M. Andreotti,[94, 67] M. P. Andrews,[66] F. Andrianala,[5] S. Andringa,[127] N. Anfimov [ORCID], A. Ankowski,[184] D. Antic,[19] M. Antoniassi,[193] M. Antonova,[84] A. Antoshkin [ORCID], A. Aranda-Fernandez,[42] L. Arellano,[135] E. Arrieta Diaz,[180] M. A. Arroyave,[66] J. Asaadi,[197] A. Ashkenazi,[194] D. M. Asner,[20] L. Asquith,[191] E. Atkin,[88] D. Auguste,[160] A. Aurisano,[40] V. Aushev,[124] D. Autiero,[110] M. B. Azam,[87] F. Azfar,[156] A. Back,[91] H. Back,[157] J. J. Back,[209] I. Bagaturia,[72] L. Bagby,[66] N. Balashov [ORCID], S. Balasubramanian,[66] P. Baldi,[24] W. Baldini,[94] J. Baldonedo,[206] B. Baller,[66] B. Bambah,[82] R. Banerjee,[216] F. Barao,[127, 112] D. Barbu,[21] G. Barenboim,[84] P. Barham Alzás,[35] G. J. Barker,[209] W. Barkhouse,[148] G. Barr,[156] J. Barranco Monarca,[77] A. Barros,[193] N. Barros,[127, 61] D. Barrow,[156] J. L. Barrow,[143] A. Basharina-Freshville,[203] A. Bashyal,[8] V. Basque,[66] C. Batchelor,[57] L. Bathe-Peters,[156] J.B.R. Battat,[210] F. Battisti,[156] F. Bay,[4] M. C. Q. Bazetto,[30] J. L. L. Bazo Alba,[169] J. F. Beacom,[154] E. Bechetoille,[110] B. Behera,[186] E. Belchior,[130] G. Bell,[52] L. Bellantoni,[66] G. Bellettini,[103, 167] V. Bellini,[93, 31] O. Beltramello,[35] N. Benekos,[35] C. Benitez Montiel,[84, 10] D. Benjamin,[20] F. Bento Neves,[127] J. Berger,[44] S. Berkman,[139] J. Bernal,[10] P. Bernardini,[97, 179] A. Bersani,[96] S. Bertolucci,[92, 17] M. Betancourt,[66] A. Betancur Rodríguez,[58] A. Bevan,[172] Y. Bezawada,[23] A. T. Bezerra,[62] T. J. Bezerra,[191] A. Bhat,[37] V. Bhatnagar,[159] J. Bhatt,[203] M. Bhattacharjee,[89] M. Bhattacharya,[66] S. Bhuller,[19] B. Bhuyan,[89] S. Biagi,[105] J. Bian,[24] K. Biery,[66] B. Bilki,[15, 108] M. Bishai,[20] A. Bitadze,[135] A. Blake,[125] F. D. Blaszczyk,[66] G. C. Blazey,[149] E. Blucher,[37] A. Bodek,[175] J. Bogenschuetz,[197] J. Boissevain,[129] S. Bolognesi,[34] T. Bolton,[119] L. Bomben,[98, 107] M. Bonesini,[98, 140] C. Bonilla-Diaz,[32] F. Bonini,[20] A. Booth,[172] F. Boran,[91] S. Bordoni,[35] R. Borges Merlo,[30] A. Borkum,[191] N. Bostan,[108] R. Bouet,[131] J. Boza,[44] J. Bracinik,[16] B. Brahma,[90] D. Brailsford,[125] F. Bramati,[98] A. Branca,[98] A. Brandt,[197] J. Bremer,[35] C. Brew,[178] S. J. Brice,[66] V. Brio,[93] C. Brizzolari,[98, 140] C. Bromberg,[139] J. Brooke,[19] A. Bross,[66] G. Brunetti,[98, 140] M. Brunetti,[209] N. Buchanan,[44] H. Budd,[175] J. Buergi,[14] A. Bundock,[19] D. Burgardt,[211] S. Butchart,[191] G. Caceres V.,[23] I. Cagnoli,[92, 17] T. Cai,[216] R. Calabrese,[100] R. Calabrese,[94, 67] J. Calcutt,[155] L. Calivers,[14] E. Calvo,[39] A. Caminata,[96] A. F. Camino,[168] W. Campanelli,[127] A. Campani,[96, 71] A. Campos Benitez,[207] N. Canci,[100] J. Capó,[84] I. Caracas,[134] D. Caratelli,[27] D. Carber,[44] J. M. Carceller,[35] G. Carini,[20] B. Carlus,[110] M. F. Carneiro,[20] P. Carniti,[98] I. Caro Terrazas,[44] H. Carranza,[197] N. Carrara,[23] L. Carroll,[119] T. Carroll,[213] A. Carter,[176] E. Casarejos,[206] D. Casazza,[94] J. F. Castaño Forero,[7] F. A. Castaño,[6] A. Castillo,[182] C. Castromonte,[106] E. Catano-Mur,[212] C. Cattadori,[98] F. Cavalier,[160] F. Cavanna,[66] S. Centro,[158] G. Cerati,[66] C. Cerna,[131] A. Cervelli,[92] A. Cervera Villanueva,[84] K. Chakraborty,[166] S. Chakraborty,[86] M. Chalifour,[35] A. Chappell,[209] N. Charitonidis,[35] A. Chatterjee,[166] H. Chen,[20] M. Chen,[24] W. C. Chen,[199] Y. Chen,[184] Z. Chen-Wishart,[176] D. Cherdack,[81] C. Chi,[45] F. Chiapponi,[92] R. Chirco,[87] N. Chitirasreemadam,[103, 167] K. Cho,[122] S. Choate,[108] D. Chokheli,[72] P. S. Chong,[164] B. Chowdhury,[8] D. Christian,[66] A. Chukanov [ORCID], M. Chung,[202] E. Church,[157] M. F. Cicala,[203] M. Cicerchia,[158] V. Cicero,[92, 17] R. Ciolini,[103] P. Clarke,[57] G. Cline,[126] T. E. Coan,[188] A. G. Cocco,[100] J. A. B. Coelho,[161] A. Cohen,[161] J. Collazo,[206] J. Collot,[76] E. Conley,[55] J. M. Conrad,[136] M. Convery,[184] S. Copello,[96] A. F. V. Cortez,[217] P. Cova,[99, 162] C. Cox,[176] L. Cremaldi,[144] L. Cremonesi,[172] J. I. Crespo-Anadón,[39] M. Crisler,[66] E. Cristaldo,[98, 10] J. Crnkovic,[66] G. Crone,[203] R. Cross,[209] A. Cudd,[43] C. Cuesta,[39] Y. Cui,[26] F. Curciarello,[95] D. Cussans,[19] J. Dai,[76] O. Dalager,[66] R. Dallavalle,[161] W. Dallaway,[199] R. D'Amico,[94, 67] H. da Motta,[33] Z. A. Dar,[212] R. Darby,[191] L. Da Silva Peres,[65] Q. David,[110] G. S. Davies,[144] S. Davini,[96] J. Dawson,[161] R. De Aguiar,[30] P. De Almeida,[30] P. Debbins,[108] I. De Bonis,[51] M. P. Decowski,[146, 3] A. de Gouvêa,[150] P. C. De Holanda,[30] I. L. De Icaza Astiz,[191] P. De Jong,[146, 3] P. Del Amo Sanchez,[51] A. De la Torre,[39] G. De Lauretis,[110] A. Delbart,[34] D. Delepine,[77] M. Delgado,[98, 140] A. Dell'Acqua,[35] G. Delle Monache,[95] N. Delmonte,[99, 162] P. De Lurgio,[8] R. Demario,[139] G. De Matteis,[97, 179] J. R. T. de Mello Neto,[65] D. M. DeMuth,[205] S. Dennis,[29] C. Densham,[178] P. Denton,[20] G. W. Deptuch,[20] A. De Roeck,[35] V. De Romeri,[84] J. P. Detje,[29] J. Devine,[35] R. Dharmapalan,[79] M. Dias,[201] A. Diaz,[28] J. S. Díaz,[91] F. Díaz,[169] F. Di Capua,[100, 145] A. Di Domenico,[181, 104] S. Di Domizio,[96, 71] S. Di Falco,[103] L. Di Giulio,[35] P. Ding,[66] L. Di Noto,[96, 71] E. Diociaiuti,[95] C. Distefano,[105] R. Diurba,[14] M. Diwan,[20] Z. Djurcic,[8] D. Doering,[184] S. Dolan,[35] F. Dolek,[207] M. J. Dolinski,[54] D. Domenici,[95] L. Domine,[184] S. Donati,[103, 167] Y. Donon,[35] S. Doran,[109] D. Douglas,[184] T.A. Doyle,[189] A. Dragone,[184] F. Drielsma,[184] L. Duarte,[201] D. Duchesneau,[51] K. Duffy,[156] K. Dugas,[24] P. Dunne,[88] B. Dutta,[195] H. Duyang,[185] D. A. Dwyer,[126] A. S. Dyshkant,[149] S. Dytman,[168] M. Eads,[149] A. Earle,[191] S. Edayath,[109] D. Edmunds,[139] J. Eisch,[66] P. Englezos,[177] A. Ereditato,[37] T. Erjavec,[23] C. O. Escobar,[66] J. J. Evans,[135] E. Ewart,[91] A. C. Ezeribe,[183] K. Fahey,[66] L. Fajt,[35]

A. Falcone,[98, 140] M. Fani',[143, 129] C. Farnese,[101] S. Farrell,[174] Y. Farzan,[111] D. Fedoseev [id], J. Felix,[77] Y. Feng,[109]
E. Fernandez-Martinez,[133] D. Fernández-Posada,[85] G. Ferry,[160] E. Fialova,[50] L. Fields,[151] P. Filip,[49] A. Filkins,[192]
F. Filthaut,[146, 173] R. Fine,[129] G. Fiorillo,[100, 145] M. Fiorini,[94, 67] S. Fogarty,[44] W. Foreman,[87] J. Fowler,[55]
J. Franc,[50] K. Francis,[149] D. Franco,[37] J. Franklin,[56] J. Freeman,[66] J. Fried,[20] A. Friedland,[184] S. Fuess,[66]
I. K. Furic,[68] K. Furman,[172] A. P. Furmanski,[143] R. Gaba,[159] A. Gabrielli,[92, 17] A. M Gago,[169] F. Galizzi,[98]
H. Gallagher,[200] N. Gallice,[20] V. Galymov,[110] E. Gamberini,[35] T. Gamble,[183] F. Ganacim,[193] R. Gandhi,[78]
S. Ganguly,[66] F. Gao,[27] S. Gao,[20] D. Garcia-Gamez,[73] M. Á. García-Peris,[84] F. Gardim,[62] S. Gardiner,[66]
D. Gastler,[18] A. Gauch,[14] J. Gauvreau,[153] P. Gauzzi,[181, 104] S. Gazzana,[95] G. Ge,[45] N. Geffroy,[51] B. Gelli,[30]
S. Gent,[187] L. Gerlach,[20] Z. Ghorbani-Moghaddam,[96] T. Giammaria,[94, 67] D. Gibin,[158, 101] I. Gil-Botella,[39]
S. Gilligan,[155] A. Gioiosa,[103] S. Giovannella,[95] C. Girerd,[110] A. K. Giri,[90] C. Giugliano,[94] V. Giusti,[103] D. Gnani,[126]
O. Gogota,[124] S. Gollapinni,[129] K. Gollwitzer,[66] R. A. Gomes,[63] L. V. Gomez Bermeo,[182] L. S. Gomez Fajardo,[182]
F. Gonnella,[16] D. Gonzalez-Diaz,[85] M. Gonzalez-Lopez,[133] M. C. Goodman,[8] S. Goswami,[166] C. Gotti,[98]
J. Goudeau,[130] E. Goudzovski,[16] C. Grace,[126] E. Gramellini,[135] R. Gran,[142] E. Granados,[77] P. Granger,[161]
C. Grant,[18] D. R. Gratieri,[70, 30] G. Grauso,[100] P. Green,[156] S. Greenberg,[126, 22] J. Greer,[19] W. C. Griffith,[191]
F. T. Groetschla,[35] K. Grzelak,[208] L. Gu,[125] W. Gu,[20] V. Guarino,[8] M. Guarise,[94, 67] R. Guenette,[135] M. Guerzoni,[92]
D. Guffanti,[98, 140] A. Guglielmi,[101] B. Guo,[185] F. Y. Guo,[189] A. Gupta,[184] V. Gupta,[146, 3] G. Gurung,[197]
D. Gutierrez,[170] P. Guzowski,[135] M. M. Guzzo,[30] S. Gwon,[38] A. Habig,[142] H. Hadavand,[197] L. Haegel,[110]
R. Haenni,[14] L. Hagaman,[214] A. Hahn,[66] J. Haiston,[186] J. Hakenmüller,[55] T. Hamernik,[66] P. Hamilton,[88]
J. Hancock,[16] F. Happacher,[95] D. A. Harris,[216, 66] A. Hart,[172] J. Hartnell,[191] T. Hartnett,[178] J. Harton,[44]
T. Hasegawa,[121] C. M. Hasnip,[35] R. Hatcher,[66] K. Hayrapetyan,[172] J. Hays,[172] E. Hazen,[18] M. He,[81] A. Heavey,[66]
K. M. Heeger,[214] J. Heise,[190] P. Hellmuth,[131] S. Henry,[175] J. Hernández-García,[84] K. Herner,[66] V. Hewes,[40]
A. Higuera,[174] C. Hilgenberg,[143] S. J. Hillier,[16] A. Himmel,[66] E. Hinkle,[37] L.R. Hirsch,[193] J. Ho,[53] J. Hoff,[66]
A. Holin,[178] T. Holvey,[156] E. Hoppe,[157] S. Horiuchi,[207] G. A. Horton-Smith,[119] T. Houdy,[160] B. Howard,[216]
R. Howell,[175] I. Hristova,[178] M. S. Hronek,[66] J. Huang,[23] R.G. Huang,[126] Z. Hulcher,[184] M. Ibrahim,[59] G. Iles,[88]
N. Ilic,[199] A. M. Iliescu,[95] R. Illingworth,[66] G. Ingratta,[92, 17] A. Ioannisian,[215] B. Irwin,[143] L. Isenhower,[1]
M. Ismerio Oliveira,[65] R. Itay,[184] C.M. Jackson,[157] V. Jain,[2] E. James,[66] W. Jang,[197] B. Jargowsky,[24] D. Jena,[66]
I. Jentz,[213] X. Ji,[20] C. Jiang,[115] J. Jiang,[189] L. Jiang,[207] A. Jipa,[21] J. H. Jo,[20] F. R. Joaquim,[127, 112] W. Johnson,[186]
C. Jollet,[131] B. Jones,[197] R. Jones,[183] N. Jovancevic,[152] M. Judah,[168] C. K. Jung,[189] T. Junk,[66] Y. Jwa,[184, 45]
M. Kabirnezhad,[88] A. C. Kaboth,[176, 178] I. Kadenko,[124] I. Kakorin [id], A. Kalitkina [id], D. Kalra,[45] M. Kandemir,[60]
D. M. Kaplan,[87] G. Karagiorgi,[45] G. Karaman,[108] A. Karcher,[126] Y. Karyotakis,[51] S. Kasai,[123] S. P. Kasetti,[130]
L. Kashur,[44] I. Katsioulas,[16] A. Kauther,[149] N. Kazaryan,[215] L. Ke,[20] E. Kearns,[18] P.T. Keener,[164] K.J. Kelly,[195]
E. Kemp,[30] O. Kemularia,[72] Y. Kermaidic,[160] W. Ketchum,[66] S. H. Kettell,[20] M. Khabibullin [id], N. Khan,[88]
A. Khvedelidze,[72] D. Kim,[195] J. Kim,[175] M. J. Kim,[66] B. King,[66] B. Kirby,[45] M. Kirby,[20] A. Kish,[66] J. Klein,[164]
J. Kleykamp,[144] A. Klustova,[88] T. Kobilarcik,[66] L. Koch,[134] K. Koehler,[213] L. W. Koerner,[81] D. H. Koh,[184]
L. Kolupaeva [id], D. Korablev [id], M. Kordosky,[212] T. Kosc,[76] U. Kose,[35] V. A. Kostelecký,[91] K. Kothekar,[19]
I. Kotler,[54] M. Kovalcuk,[49] V. Kozhukalov [id], W. Krah,[146] R. Kralik,[191] M. Kramer,[126] L. Kreczko,[19]
F. Krennrich,[109] I. Kreslo,[14] T. Kroupova,[164] S. Kubota,[135] M. Kubu,[35] Y. Kudenko [id], V. A. Kudryavtsev,[183]
G. Kufatty,[69] S. Kuhlmann,[8] S. Kulagin [id], J. Kumar,[79] P. Kumar,[183] S. Kumaran,[24] J. Kunzmann,[14] R. Kuravi,[126]
N. Kurita,[184] C. Kuruppu,[185] V. Kus,[50] T. Kutter,[130] M. Kuźniak,[217] J. Kvasnicka,[49] T. Labree,[149] T. Lackey,[66]
I. Lalău,[21] A. Lambert,[126] B. J. Land,[164] C. E. Lane,[54] N. Lane,[135] K. Lang,[198] T. Langford,[214] M. Langstaff,[135]
F. Lanni,[35] O. Lantwin,[51] J. Larkin,[20] P. Lasorak,[88] D. Last,[164] A. Laudrain,[134] A. Laundrie,[213] G. Laurenti,[92]
E. Lavaut,[160] P. Laycock,[20] I. Lazanu,[21] R. LaZur,[44] M. Lazzaroni,[99, 141] T. Le,[200] S. Leardini,[85] J. Learned,[79]
T. LeCompte,[184] V. Legin,[124] G. Lehmann Miotto,[35] R. Lehnert,[91] M. A. Leigui de Oliveira,[64] M. Leitner,[126]
D. Leon Silverio,[186] L. M. Lepin,[69] J.-Y Li,[57] S. W. Li,[24] Y. Li,[20] H. Liao,[119] C. S. Lin,[126] D. Lindebaum,[19]
S. Linden,[20] R. A. Lineros,[32] A. Lister,[213] B. R. Littlejohn,[87] H. Liu,[20] J. Liu,[24] Y. Liu,[37] S. Lockwitz,[66]
M. Lokajicek,[49] I. Lomidze,[72] K. Long,[88] T. V. Lopes,[62] J.Lopez,[6] I. López de Rego,[39] N. López-March,[84]
T. Lord,[209] J. M. LoSecco,[151] W. C. Louis,[129] A. Lozano Sanchez,[54] X.-G. Lu,[209] K.B. Luk,[80, 126, 22] B. Lunday,[164]
X. Luo,[27] E. Luppi,[94, 67] D. MacFarlane,[184] A. A. Machado,[30] P. Machado,[66] C. T. Macias,[91] J. R. Macier,[66]
M. MacMahon,[203] A. Maddalena,[75] A. Madera,[35] P. Madigan,[22, 126] S. Magill,[8] C. Magueur,[160] K. Mahn,[139]
A. Maio,[127, 61] A. Major,[55] K. Majumdar,[128] S. Mameli,[103] M. Man,[199] R. C. Mandujano,[24] J. Maneira,[127, 61]
S. Manly,[175] A. Mann,[200] K. Manolopoulos,[178] M. Manrique Plata,[91] S. Manthey Corchado,[39] V. N. Manyam,[20]
M. Marchan,[66] A. Marchionni,[66] W. Marciano,[20] D. Marfatia,[79] C. Mariani,[207] J. Maricic,[79] F. Marinho,[113]
A. D. Marino,[43] T. Markiewicz,[184] F. Das Chagas Marques,[30] C. Marquet,[131] M. Marshak,[143] C. M. Marshall,[175]

J. Marshall,[209] L. Martina,[97, 179] J. Martín-Albo,[84] N. Martinez,[119] D.A. Martinez Caicedo,[186] F. Martínez López,[172] P. Martínez Miravé,[84] S. Martynenko,[20] V. Mascagna,[98] C. Massari,[98] A. Mastbaum,[177] F. Matichard,[126] S. Matsuno,[79] G. Matteucci,[100, 145] J. Matthews,[130] C. Mauger,[164] N. Mauri,[92, 17] K. Mavrokoridis,[128] I. Mawby,[125] R. Mazza,[98] T. McAskill,[210] N. McConkey,[172, 203] K. S. McFarland,[175] C. McGrew,[189] A. McNab,[135] L. Meazza,[98] V. C. N. Meddage,[68] A. Mefodiev ⓞ, B. Mehta,[159] P. Mehta,[116] P. Melas,[11] O. Mena,[84] H. Mendez,[170] P. Mendez,[35] D. P. Méndez,[20] A. Menegolli,[102, 163] G. Meng,[101] A. C. E. A. Mercuri,[193] A. Meregaglia,[131] M. D. Messier,[91] S. Metallo,[143] W. Metcalf,[130] M. Mewes,[91] H. Meyer,[211] T. Miao,[66] J. Micallef,[200, 136] A. Miccoli,[97] G. Michna,[187] R. Milincic,[79] F. Miller,[213] G. Miller,[135] W. Miller,[143] O. Mineev ⓞ, A. Minotti,[98, 140] L. Miralles,[35] O. G. Miranda,[41] C. Mironov,[161] S. Miryala,[20] S. Miscetti,[95] C. S. Mishra,[66] P. Mishra,[82] S. R. Mishra,[185] A. Mislivec,[143] M. Mitchell,[130] D. Mladenov,[35] I. Mocioiu,[165] A. Mogan,[66] N. Moggi,[92, 17] R. Mohanta,[82] T. A. Mohayai,[91] N. Mokhov,[66] J. Molina,[10] L. Molina Bueno,[84] E. Montagna,[92, 17] A. Montanari,[92] C. Montanari,[102, 66, 163] D. Montanari,[66] D. Montanino,[97, 179] L. M. Montaño Zetina,[41] M. Mooney,[44] A. F. Moor,[183] Z. Moore,[192] D. Moreno,[7] O. Moreno-Palacios,[212] L. Morescalchi,[103] D. Moretti,[98] R. Moretti,[98] C. Morris,[81] C. Mossey,[66] C. A. Moura,[64] G. Mouster,[125] W. Mu,[66] L. Mualem,[28] J. Mueller,[44] M. Muether,[211] F. Muheim,[57] A. Muir,[52] M. Mulhearn,[23] D. Munford,[81] L. J. Munteanu,[35] H. Muramatsu,[143] J. Muraz,[76] M. Murphy,[207] T. Murphy,[192] J. Muse,[143] A. Mytilinaki,[178] J. Nachtman,[108] Y. Nagai,[59] S. Nagu,[132] R. Nandakumar,[178] D. Naples,[168] S. Narita,[114] A. Navrer-Agasson,[88, 135] N. Nayak,[20] M. Nebot-Guinot,[57] A. Nehm,[134] J. K. Nelson,[212] O. Neogi,[108] J. Nesbit,[213] M. Nessi,[66, 35] D. Newbold,[178] M. Newcomer,[164] R. Nichol,[203] F. Nicolas-Arnaldos,[73] A. Nikolica,[164] J. Nikolov,[152] E. Niner,[66] K. Nishimura,[79] A. Norman,[66] A. Norrick,[66] P. Novella,[84] A. Nowak,[125] J. A. Nowak,[125] M. Oberling,[8] J. P. Ochoa-Ricoux,[24] S. Oh,[55] S.B. Oh,[66] A. Olivier,[151] A. Olshevskiy ⓞ, T. Olson,[81] Y. Onel,[108] Y. Onishchuk,[124] A. Oranday,[91] G. D. Orebi Gann,[22, 126] M. Osbiston,[209] J. A. Osorio Vélez,[6] L. O'Sullivan,[134] L. Otiniano Ormachea,[46, 106] J. Ott,[24] L. Pagani,[23] G. Palacio,[58] O. Palamara,[66] S. Palestini,[35] J. M. Paley,[66] M. Pallavicini,[96, 71] C. Palomares,[39] S. Pan,[166] P. Panda,[82] W. Panduro Vazquez,[176] E. Pantic,[23] V. Paolone,[168] R. Papaleo,[105] A. Papanestis,[178] D. Papoulias,[11] S. Paramesvaran,[19] A. Paris,[170] S. Parke,[66] E. Parozzi,[98, 140] S. Parsa,[14] Z. Parsa,[20] S. Parveen,[116] M. Parvu,[21] D. Pasciuto,[103] S. Pascoli,[92, 17] L. Pasqualini,[92, 17] J. Pasternak,[88] C. Patrick,[57, 203] L. Patrizii,[92] R. B. Patterson,[28] T. Patzak,[161] A. Paudel,[66] L. Paulucci,[64] Z. Pavlovic,[66] G. Pawloski,[143] D. Payne,[128] V. Pec,[49] E. Pedreschi,[103] S. J. M. Peeters,[191] W. Pellico,[66] A. Pena Perez,[184] E. Pennacchio,[110] A. Penzo,[108] O. L. G. Peres,[30] Y. F. Perez Gonzalez,[56] L. Pérez-Molina,[39] C. Pernas,[212] J. Perry,[57] D. Pershey,[69] G. Pessina,[98] G. Petrillo,[184] C. Petta,[93, 31] R. Petti,[185] M. Pfaff,[88] V. Pia,[92, 17] L. Pickering,[178, 176] F. Pietropaolo,[35, 101] V.L.Pimentel,[47, 30] G. Pinaroli,[20] S. Pincha,[89] J. Pinchault,[51] K. Pitts,[207] K. Plows,[156] C. Pollack,[170] T. Pollman,[146, 3] F. Pompa,[84] X. Pons,[35] N. Poonthottathil,[86, 109] V. Popov,[194] F. Poppi,[92, 17] J. Porter,[191] L. G. Porto Paixão,[30] M. Potekhin,[20] R. Potenza,[93, 31] J. Pozimski,[88] M. Pozzato,[92, 17] T. Prakash,[126] C. Pratt,[23] M. Prest,[98] F. Psihas,[66] D. Pugnere,[110] X. Qian,[20] J. Queen,[55] J. L. Raaf,[66] V. Radeka,[20] J. Rademacker,[19] B. Radics,[216] F. Raffaelli,[103] A. Rafique,[8] E. Raguzin,[20] M. Rai,[209] S. Rajagopalan,[20] J. Rajaoalisoa,[40] I. Rakhno,[66] L. Rakotondravohitra,[5] L. Ralte,[90] M. A. Ramirez Delgado,[164] B. Ramson,[66] A. Rappoldi,[102, 163] G. Raselli,[102, 163] P. Ratoff,[125] R. Ray,[66] H. Razafinime,[40] E. M. Rea,[143] J. S. Real,[76] B. Rebel,[213, 66] R. Rechenmacher,[66] J. Reichenbacher,[186] S. D. Reitzner,[66] H. Rejeb Sfar,[35] E. Renner,[129] A. Renshaw,[81] S. Rescia,[20] F. Resnati,[35] Diego Restrepo,[6] C. Reynolds,[172] M. Ribas,[193] S. Riboldi,[99] C. Riccio,[189] G. Riccobene,[105] J. S. Ricol,[76] M. Rigan,[191] E. V. Rincón,[58] A. Ritchie-Yates,[176] S. Ritter,[134] D. Rivera,[129] R. Rivera,[66] A. Robert,[76] J. L. Rocabado Rocha,[84] L. Rochester,[184] M. Roda,[128] P. Rodrigues,[156] M. J. Rodriguez Alonso,[35] J. Rodriguez Rondon,[186] S. Rosauro-Alcaraz,[160] P. Rosier,[160] D. Ross,[139] M. Rossella,[102, 163] M. Rossi,[35] M. Ross-Lonergan,[129] N. Roy,[216] P. Roy,[211] C. Rubbia,[74] A. Ruggeri,[92] G. Ruiz,[135] B. Russell,[136] D. Ruterbories,[175] A. Rybnikov ⓞ, S. Sacerdoti,[161] S. Saha,[168] S. K. Sahoo,[90] N. Sahu,[90] P. Sala,[66] N. Samios,[20] O. Samoylov ⓞ, M. C. Sanchez,[69] A. Sánchez Bravo,[84] A. Sánchez-Castillo,[73] P. Sanchez-Lucas,[73] V. Sandberg,[129] D. A. Sanders,[144] S. Sanfilippo,[105] D. Sankey,[178] D. Santoro,[99, 162] N. Saoulidou,[11] P. Sapienza,[105] C. Sarasty,[40] I. Sarcevic,[9] I. Sarra,[95] G. Savage,[66] V. Savinov,[168] G. Scanavini,[214] A. Scaramelli,[102] A. Scarff,[183] T. Schefke,[130] H. Schellman,[155, 66] S. Schifano,[94, 67] P. Schlabach,[66] D. Schmitz,[37] A. W. Schneider,[136] K. Scholberg,[55] A. Schukraft,[66] B. Schuld,[43] A. Segade,[206] E. Segreto,[30] A. Selyunin ⓞ, D. Senadheera,[168] S. H. Seo,[66] C. R. Senise,[201] J. Sensenig,[164] M. H. Shaevitz,[45] P. Shanahan,[66] P. Sharma,[159] R. Kumar,[171] S. Sharma Poudel,[186] K. Shaw,[191] T. Shaw,[66] K. Shchablo,[110] J. Shen,[164] C. Shepherd-Themistocleous,[178] A. Sheshukov ⓞ, J. Shi,[29] W. Shi,[189] S. Shin,[117] S. Shivakoti,[211] I. Shoemaker,[207] D. Shooltz,[139] R. Shrock,[189] B. Siddi,[94] M. Siden,[44] J. Silber,[126] L. Simard,[160] J. Sinclair,[184] G. Sinev,[186] J. Singh,[23] L. Singh,[48] P. Singh,[172] V. Singh,[48] S. Singh Chauhan,[159] R. Sipos,[35] C. Sironneau,[161] G. Sirri,[92] K. Siyeon,[38] K. Skarpaas,[184] J. Smedley,[175]

E. Smith,[91] J. Smith,[189] P. Smith,[91] J. Smolik,[50, 49] M. Smy,[24] M. Snape,[209] E.L. Snider,[66] P. Snopok,[87]
D. Snowden-Ifft,[153] M. Soares Nunes,[66] H. Sobel,[24] M. Soderberg,[192] S. Sokolov , C. J. Solano Salinas,[204, 106]
S. Söldner-Rembold,[88, 135] N. Solomey,[211] V. Solovov,[127] W. E. Sondheim,[129] M. Sorel,[84] A. Sotnikov ,
J. Soto-Oton,[84] A. Sousa,[40] K. Soustruznik,[36] F. Spinella,[103] J. Spitz,[138] N. J. C. Spooner,[183] K. Spurgeon,[192]
D. Stalder,[10] M. Stancari,[66] L. Stanco,[158, 101] J. Steenis,[23] R. Stein,[19] H. M. Steiner,[126] A. F. Steklain Lisbôa,[193]
A. Stepanova , J. Stewart,[20] B. Stillwell,[37] J. Stock,[186] F. Stocker,[35] T. Stokes,[130] M. Strait,[143] T. Strauss,[66]
L. Strigari,[195] A. Stuart,[42] J. G. Suarez,[58] J. Subash,[16] A. Surdo,[97] L. Suter,[66] C. M. Sutera,[93, 31] K. Sutton,[28]
Y. Suvorov,[100, 145] R. Svoboda,[23] S. K. Swain,[147] B. Szczerbinska,[196] A. M. Szelc,[57] A. Sztuc,[203] A. Taffara,[103]
N. Talukdar,[185] J. Tamara,[7] H. A. Tanaka,[184] S. Tang,[20] N. Taniuchi,[29] A. M. Tapia Casanova,[137] B. Tapia
Oregui,[198] A. Tapper,[88] S. Tariq,[66] E. Tarpara,[20] E. Tatar,[83] R. Tayloe,[91] D. Tedeschi,[185] A. M. Teklu,[189] J. Tena
Vidal,[194] P. Tennessen,[126, 4] M. Tenti,[92] K. Terao,[184] F. Terranova,[98, 140] G. Testera,[96] T. Thakore,[40] A. Thea,[178]
S. Thomas,[192] A. Thompson,[195] C. Thorn,[20] S. C. Timm,[66] E. Tiras,[60, 108] V. Tishchenko,[20] N. Todorović,[152]
L. Tomassetti,[94, 67] A. Tonazzo,[161] D. Torbunov,[20] M. Torti,[98, 140] M. Tortola,[84] F. Tortorici,[93, 31] N. Tosi,[92]
D. Totani,[27] M. Toups,[66] C. Touramanis,[128] D. Tran,[81] R. Travaglini,[92] J. Trevor,[28] E. Triller,[139] S. Trilov,[19]
J. Truchon,[213] D. Truncali,[181, 104] W. H. Trzaska,[118] Y. Tsai,[24] Y.-T. Tsai,[184] Z. Tsamalaidze,[72] K. V. Tsang,[184]
N. Tsverava,[72] S. Z. Tu,[115] S. Tufanli,[35] C. Tunnell,[174] S. Turnberg,[87] J. Turner,[56] M. Tuzi,[84] J. Tyler,[119]
E. Tyley,[183] M. Tzanov,[130] M. A. Uchida,[29] J. Ureña González,[84] J. Urheim,[91] T. Usher,[184] H. Utaegbulam,[175]
S. Uzunyan,[149] M. R. Vagins,[120, 24] P. Vahle,[212] S. Valder,[191] G. A. Valdiviesso,[62] E. Valencia,[77] R. Valentim,[201]
Z. Vallari,[28] E. Vallazza,[98] J. W. F. Valle,[84] R. Van Berg,[164] R. G. Van de Water,[129] D. V. Forero,[137]
A. Vannozzi,[95] M. Van Nuland-Troost,[146] F. Varanini,[101] D. Vargas Oliva,[199] S. Vasina , N. Vaughan,[155]
K. Vaziri,[66] A. Vázquez-Ramos,[73] J. Vega,[46] S. Ventura,[101] A. Verdugo,[39] S. Vergani,[203] M. Verzocchi,[66]
K. Vetter,[66] M. Vicenzi,[20] H. Vieira de Souza,[161] C. Vignoli,[75] C. Vilela,[127] E. Villa,[35] S. Viola,[105] B. Viren,[20]
A. P. Vizcaya Hernandez,[44] Q. Vuong,[175] A. V. Waldron,[172] M. Wallbank,[40] J. Walsh,[139] T. Walton,[66] H. Wang,[25]
J. Wang,[186] L. Wang,[126] M.H.L.S. Wang,[66] X. Wang,[66] Y. Wang,[25] K. Warburton,[109] D. Warner,[44] L. Warsame,[88]
M.O. Wascko,[156, 178] D. Waters,[203] A. Watson,[16] K. Wawrowska,[178, 191] A. Weber,[134, 66] C. M. Weber,[143]
M. Weber,[14] H. Wei,[130] A. Weinstein,[109] S. Westerdale,[26] M. Wetstein,[109] K. Whalen,[178] A. White,[197] A. White,[214]
L. H. Whitehead,[29] D. Whittington,[192] J. Wilhlemi,[214] M. J. Wilking,[143] A. Wilkinson,[203] C. Wilkinson,[126]
F. Wilson,[178] R. J. Wilson,[44] P. Winter,[8] W. Wisniewski,[184] J. Wolcott,[200] J. Wolfs,[175] T. Wongjirad,[200]
A. Wood,[81] K. Wood,[126] E. Worcester,[20] M. Worcester,[20] M. Wospakrik,[66] K. Wresilo,[29] C. Wret,[175] S. Wu,[143]
W. Wu,[66] W. Wu,[24] M. Wurm,[134] J. Wyenberg,[53] Y. Xiao,[24] I. Xiotidis,[88] B. Yaeggy,[40] N. Yahlali,[84]
E. Yandel,[27] J. Yang,[80] K. Yang,[156] T. Yang,[66] A. Yankelevich,[24] N. Yershov , K. Yonehara,[66] T. Young,[148]
B. Yu,[20] H. Yu,[20] J. Yu,[197] Y. Yu,[87] W. Yuan,[57] R. Zaki,[216] J. Zalesak,[49] L. Zambelli,[51] B. Zamorano,[73]
A. Zani,[99] O. Zapata,[6] L. Zazueta,[192] G. P. Zeller,[66] J. Zennamo,[66] K. Zeug,[213] C. Zhang,[20] S. Zhang,[91]
M. Zhao,[20] E. Zhivun,[20] E. D. Zimmerman,[43] S. Zucchelli,[92, 17] J. Zuklin,[49] V. Zutshi,[149] and R. Zwaska[66]

(The DUNE Collaboration)

[1]Abilene Christian University, Abilene, TX 79601, USA
[2]University at Albany, SUNY, Albany, NY 12222, USA
[3]University of Amsterdam, NL-1098 XG Amsterdam, The Netherlands
[4]Antalya Bilim University, 07190 Döşemealtı/Antalya, Turkey
[5]University of Antananarivo, Antananarivo 101, Madagascar
[6]University of Antioquia, Medellín, Colombia
[7]Universidad Antonio Nariño, Bogotá, Colombia
[8]Argonne National Laboratory, Argonne, IL 60439, USA
[9]University of Arizona, Tucson, AZ 85721, USA
[10]Universidad Nacional de Asunción, San Lorenzo, Paraguay
[11]University of Athens, Zografou GR 157 84, Greece
[12]Universidad del Atlántico, Barranquilla, Atlántico, Colombia
[13]Augustana University, Sioux Falls, SD 57197, USA
[14]University of Bern, CH-3012 Bern, Switzerland
[15]Beykent University, Istanbul, Turkey
[16]University of Birmingham, Birmingham B15 2TT, United Kingdom
[17]Università di Bologna, 40127 Bologna, Italy
[18]Boston University, Boston, MA 02215, USA
[19]University of Bristol, Bristol BS8 1TL, United Kingdom
[20]Brookhaven National Laboratory, Upton, NY 11973, USA
[21]University of Bucharest, Bucharest, Romania
[22]University of California Berkeley, Berkeley, CA 94720, USA

[23] University of California Davis, Davis, CA 95616, USA

[24] University of California Irvine, Irvine, CA 92697, USA

[25] University of California Los Angeles, Los Angeles, CA 90095, USA

[26] University of California Riverside, Riverside CA 92521, USA

[27] University of California Santa Barbara, Santa Barbara, CA 93106, USA

[28] California Institute of Technology, Pasadena, CA 91125, USA

[29] University of Cambridge, Cambridge CB3 0HE, United Kingdom

[30] Universidade Estadual de Campinas, Campinas - SP, 13083-970, Brazil

[31] Università di Catania, 2 - 95131 Catania, Italy

[32] Universidad Católica del Norte, Antofagasta, Chile

[33] Centro Brasileiro de Pesquisas Físicas, Rio de Janeiro, RJ 22290-180, Brazil

[34] IRFU, CEA, Université Paris-Saclay, F-91191 Gif-sur-Yvette, France

[35] CERN, The European Organization for Nuclear Research, 1211 Meyrin, Switzerland

[36] Institute of Particle and Nuclear Physics of the Faculty of Mathematics
and Physics of the Charles University, 180 00 Prague 8, Czech Republic

[37] University of Chicago, Chicago, IL 60637, USA

[38] Chung-Ang University, Seoul 06974, South Korea

[39] CIEMAT, Centro de Investigaciones Energéticas, Medioambientales y Tecnológicas, E-28040 Madrid, Spain

[40] University of Cincinnati, Cincinnati, OH 45221, USA

[41] Centro de Investigación y de Estudios Avanzados del Instituto Politécnico Nacional (Cinvestav), Mexico City, Mexico

[42] Universidad de Colima, Colima, Mexico

[43] University of Colorado Boulder, Boulder, CO 80309, USA

[44] Colorado State University, Fort Collins, CO 80523, USA

[45] Columbia University, New York, NY 10027, USA

[46] Comisión Nacional de Investigación y Desarrollo Aeroespacial, Lima, Peru

[47] Centro de Tecnologia da Informacao Renato Archer, Amarais - Campinas, SP - CEP 13069-901

[48] Central University of South Bihar, Gaya, 824236, India

[49] Institute of Physics, Czech Academy of Sciences, 182 00 Prague 8, Czech Republic

[50] Czech Technical University, 115 19 Prague 1, Czech Republic

[51] Laboratoire d'Annecy de Physique des Particules, Université Savoie Mont Blanc, CNRS, LAPP-IN2P3, 74000 Annecy, France

[52] Daresbury Laboratory, Cheshire WA4 4AD, United Kingdom

[53] Dordt University, Sioux Center, IA 51250, USA

[54] Drexel University, Philadelphia, PA 19104, USA

[55] Duke University, Durham, NC 27708, USA

[56] Durham University, Durham DH1 3LE, United Kingdom

[57] University of Edinburgh, Edinburgh EH8 9YL, United Kingdom

[58] Universidad EIA, Envigado, Antioquia, Colombia

[59] Eötvös Loránd University, 1053 Budapest, Hungary

[60] Erciyes University, Kayseri, Turkey

[61] Faculdade de Ciências da Universidade de Lisboa - FCUL, 1749-016 Lisboa, Portugal

[62] Universidade Federal de Alfenas, Poços de Caldas - MG, 37715-400, Brazil

[63] Universidade Federal de Goias, Goiania, GO 74690-900, Brazil

[64] Universidade Federal do ABC, Santo André - SP, 09210-580, Brazil

[65] Universidade Federal do Rio de Janeiro, Rio de Janeiro - RJ, 21941-901, Brazil

[66] Fermi National Accelerator Laboratory, Batavia, IL 60510, USA

[67] University of Ferrara, Ferrara, Italy

[68] University of Florida, Gainesville, FL 32611-8440, USA

[69] Florida State University, Tallahassee, FL, 32306 USA

[70] Fluminense Federal University, 9 Icaraí Niterói - RJ, 24220-900, Brazil

[71] Università degli Studi di Genova, Genova, Italy

[72] Georgian Technical University, Tbilisi, Georgia

[73] University of Granada & CAFPE, 18002 Granada, Spain

[74] Gran Sasso Science Institute, L'Aquila, Italy

[75] Laboratori Nazionali del Gran Sasso, L'Aquila AQ, Italy

[76] University Grenoble Alpes, CNRS, Grenoble INP, LPSC-IN2P3, 38000 Grenoble, France

[77] Universidad de Guanajuato, Guanajuato, C.P. 37000, Mexico

[78] Harish-Chandra Research Institute, Jhunsi, Allahabad 211 019, India

[79] University of Hawaii, Honolulu, HI 96822, USA

[80] Hong Kong University of Science and Technology, Kowloon, Hong Kong, China

[81] University of Houston, Houston, TX 77204, USA

[82] University of Hyderabad, Gachibowli, Hyderabad - 500 046, India

[83] Idaho State University, Pocatello, ID 83209, USA

[84] Instituto de Física Corpuscular, CSIC and Universitat de València, 46980 Paterna, Valencia, Spain

[85] Instituto Galego de Física de Altas Enerxías, University of Santiago de Compostela, Santiago de Compostela, 15782, Spain

[86]Indian Institute of Technology Kanpur, Uttar Pradesh 208016, India
[87]Illinois Institute of Technology, Chicago, IL 60616, USA
[88]Imperial College of Science, Technology and Medicine, London SW7 2BZ, United Kingdom
[89]Indian Institute of Technology Guwahati, Guwahati, 781 039, India
[90]Indian Institute of Technology Hyderabad, Hyderabad, 502285, India
[91]Indiana University, Bloomington, IN 47405, USA
[92]Istituto Nazionale di Fisica Nucleare Sezione di Bologna, 40127 Bologna BO, Italy
[93]Istituto Nazionale di Fisica Nucleare Sezione di Catania, I-95123 Catania, Italy
[94]Istituto Nazionale di Fisica Nucleare Sezione di Ferrara, I-44122 Ferrara, Italy
[95]Istituto Nazionale di Fisica Nucleare Laboratori Nazionali di Frascati, Frascati, Roma, Italy
[96]Istituto Nazionale di Fisica Nucleare Sezione di Genova, 16146 Genova GE, Italy
[97]Istituto Nazionale di Fisica Nucleare Sezione di Lecce, 73100 - Lecce, Italy
[98]Istituto Nazionale di Fisica Nucleare Sezione di Milano Bicocca, 3 - I-20126 Milano, Italy
[99]Istituto Nazionale di Fisica Nucleare Sezione di Milano, 20133 Milano, Italy
[100]Istituto Nazionale di Fisica Nucleare Sezione di Napoli, I-80126 Napoli, Italy
[101]Istituto Nazionale di Fisica Nucleare Sezione di Padova, 35131 Padova, Italy
[102]Istituto Nazionale di Fisica Nucleare Sezione di Pavia, I-27100 Pavia, Italy
[103]Istituto Nazionale di Fisica Nucleare Laboratori Nazionali di Pisa, Pisa PI, Italy
[104]Istituto Nazionale di Fisica Nucleare Sezione di Roma, 00185 Roma RM, Italy
[105]Istituto Nazionale di Fisica Nucleare Laboratori Nazionali del Sud, 95123 Catania, Italy
[106]Universidad Nacional de Ingeniería, Lima 25, Perú
[107]University of Insubria, Via Ravasi, 2, 21100 Varese VA, Italy
[108]University of Iowa, Iowa City, IA 52242, USA
[109]Iowa State University, Ames, Iowa 50011, USA
[110]Institut de Physique des 2 Infinis de Lyon, 69622 Villeurbanne, France
[111]Institute for Research in Fundamental Sciences, Tehran, Iran
[112]Instituto Superior Técnico - IST, Universidade de Lisboa, 1049-001 Lisboa, Portugal
[113]Instituto Tecnológico de Aeronáutica, Sao Jose dos Campos, Brazil
[114]Iwate University, Morioka, Iwate 020-8551, Japan
[115]Jackson State University, Jackson, MS 39217, USA
[116]Jawaharlal Nehru University, New Delhi 110067, India
[117]Jeonbuk National University, Jeonrabuk-do 54896, South Korea
[118]Jyväskylä University, FI-40014 Jyväskylä, Finland
[119]Kansas State University, Manhattan, KS 66506, USA
[120]Kavli Institute for the Physics and Mathematics of the Universe, Kashiwa, Chiba 277-8583, Japan
[121]High Energy Accelerator Research Organization (KEK), Ibaraki, 305-0801, Japan
[122]Korea Institute of Science and Technology Information, Daejeon, 34141, South Korea
[123]National Institute of Technology, Kure College, Hiroshima, 737-8506, Japan
[124]Taras Shevchenko National University of Kyiv, 01601 Kyiv, Ukraine
[125]Lancaster University, Lancaster LA1 4YB, United Kingdom
[126]Lawrence Berkeley National Laboratory, Berkeley, CA 94720, USA
[127]Laboratório de Instrumentação e Física Experimental de Partículas, 1649-003 Lisboa and 3004-516 Coimbra, Portugal
[128]University of Liverpool, L69 7ZE, Liverpool, United Kingdom
[129]Los Alamos National Laboratory, Los Alamos, NM 87545, USA
[130]Louisiana State University, Baton Rouge, LA 70803, USA
[131]Laboratoire de Physique des Deux Infinis Bordeaux - IN2P3, F-33175 Gradignan, Bordeaux, France,
[132]University of Lucknow, Uttar Pradesh 226007, India
[133]Madrid Autonoma University and IFT UAM/CSIC, 28049 Madrid, Spain
[134]Johannes Gutenberg-Universität Mainz, 55122 Mainz, Germany
[135]University of Manchester, Manchester M13 9PL, United Kingdom
[136]Massachusetts Institute of Technology, Cambridge, MA 02139, USA
[137]University of Medellín, Medellín, 050026 Colombia
[138]University of Michigan, Ann Arbor, MI 48109, USA
[139]Michigan State University, East Lansing, MI 48824, USA
[140]Università di Milano Bicocca , 20126 Milano, Italy
[141]Università degli Studi di Milano, I-20133 Milano, Italy
[142]University of Minnesota Duluth, Duluth, MN 55812, USA
[143]University of Minnesota Twin Cities, Minneapolis, MN 55455, USA
[144]University of Mississippi, University, MS 38677 USA
[145]Università degli Studi di Napoli Federico II , 80138 Napoli NA, Italy
[146]Nikhef National Institute of Subatomic Physics, 1098 XG Amsterdam, Netherlands
[147]National Institute of Science Education and Research (NISER), Odisha 752050, India
[148]University of North Dakota, Grand Forks, ND 58202-8357, USA
[149]Northern Illinois University, DeKalb, IL 60115, USA

[150]Northwestern University, Evanston, Il 60208, USA

[151]University of Notre Dame, Notre Dame, IN 46556, USA

[152]University of Novi Sad, 21102 Novi Sad, Serbia

[153]Occidental College, Los Angeles, CA 90041

[154]Ohio State University, Columbus, OH 43210, USA

[155]Oregon State University, Corvallis, OR 97331, USA

[156]University of Oxford, Oxford, OX1 3RH, United Kingdom

[157]Pacific Northwest National Laboratory, Richland, WA 99352, USA

[158]Universtà degli Studi di Padova, I-35131 Padova, Italy

[159]Panjab University, Chandigarh, 160014, India

[160]Université Paris-Saclay, CNRS/IN2P3, IJCLab, 91405 Orsay, France

[161]Université Paris Cité, CNRS, Astroparticule et Cosmologie, Paris, France

[162]University of Parma, 43121 Parma PR, Italy

[163]Università degli Studi di Pavia, 27100 Pavia PV, Italy

[164]University of Pennsylvania, Philadelphia, PA 19104, USA

[165]Pennsylvania State University, University Park, PA 16802, USA

[166]Physical Research Laboratory, Ahmedabad 380 009, India

[167]Università di Pisa, I-56127 Pisa, Italy

[168]University of Pittsburgh, Pittsburgh, PA 15260, USA

[169]Pontificia Universidad Católica del Perú, Lima, Perú

[170]University of Puerto Rico, Mayaguez 00681, Puerto Rico, USA

[171]Punjab Agricultural University, Ludhiana 141004, India

[172]Queen Mary University of London, London E1 4NS, United Kingdom

[173]Radboud University, NL-6525 AJ Nijmegen, Netherlands

[174]Rice University, Houston, TX 77005

[175]University of Rochester, Rochester, NY 14627, USA

[176]Royal Holloway College London, London, TW20 0EX, United Kingdom

[177]Rutgers University, Piscataway, NJ, 08854, USA

[178]STFC Rutherford Appleton Laboratory, Didcot OX11 0QX, United Kingdom

[179]Università del Salento, 73100 Lecce, Italy

[180]Universidad del Magdalena, Santa Marta - Colombia

[181]Sapienza University of Rome, 00185 Roma RM, Italy

[182]Universidad Sergio Arboleda, 11022 Bogotá, Colombia

[183]University of Sheffield, Sheffield S3 7RH, United Kingdom

[184]SLAC National Accelerator Laboratory, Menlo Park, CA 94025, USA

[185]University of South Carolina, Columbia, SC 29208, USA

[186]South Dakota School of Mines and Technology, Rapid City, SD 57701, USA

[187]South Dakota State University, Brookings, SD 57007, USA

[188]Southern Methodist University, Dallas, TX 75275, USA

[189]Stony Brook University, SUNY, Stony Brook, NY 11794, USA

[190]Sanford Underground Research Facility, Lead, SD, 57754, USA

[191]University of Sussex, Brighton, BN1 9RH, United Kingdom

[192]Syracuse University, Syracuse, NY 13244, USA

[193]Universidade Tecnológica Federal do Paraná, Curitiba, Brazil

[194]Tel Aviv University, Tel Aviv-Yafo, Israel

[195]Texas A&M University, College Station, Texas 77840

[196]Texas A&M University - Corpus Christi, Corpus Christi, TX 78412, USA

[197]University of Texas at Arlington, Arlington, TX 76019, USA

[198]University of Texas at Austin, Austin, TX 78712, USA

[199]University of Toronto, Toronto, Ontario M5S 1A1, Canada

[200]Tufts University, Medford, MA 02155, USA

[201]Universidade Federal de São Paulo, 09913-030, São Paulo, Brazil

[202]Ulsan National Institute of Science and Technology, Ulsan 689-798, South Korea

[203]University College London, London, WC1E 6BT, United Kingdom

[204]Universidad Nacional Mayor de San Marcos, Lima, Peru

[205]Valley City State University, Valley City, ND 58072, USA

[206]University of Vigo, E- 36310 Vigo Spain

[207]Virginia Tech, Blacksburg, VA 24060, USA

[208]University of Warsaw, 02-093 Warsaw, Poland

[209]University of Warwick, Coventry CV4 7AL, United Kingdom

[210]Wellesley College, Wellesley, MA 02481, USA

[211]Wichita State University, Wichita, KS 67260, USA

[212]William and Mary, Williamsburg, VA 23187, USA

[213]University of Wisconsin Madison, Madison, WI 53706, USA

[214] *Yale University, New Haven, CT 06520, USA*

[215] *Yerevan Institute for Theoretical Physics and Modeling, Yerevan 0036, Armenia*

[216] *York University, Toronto M3J 1P3, Canada*

[217] *Astrocent, Nicolaus Copernicus Astronomical Center of the Polish Academy of Sciences, Warsaw 00-614, Poland*

Abstract

The international collaboration designing and constructing the Deep Underground Neutrino Experiment (DUNE) at the Long-Baseline Neutrino Facility (LBNF) has developed a two-phase strategy toward the implementation of this leading-edge, large-scale science project. The 2023 report of the US Particle Physics Project Prioritization Panel (P5) reaffirmed this vision and strongly endorsed DUNE Phase I and Phase II, as did the European Strategy for Particle Physics. While the construction of the DUNE Phase I is well underway, this White Paper focuses on DUNE Phase II planning. DUNE Phase-II consists of a third and fourth far detector (FD) module, an upgraded near detector complex, and an enhanced 2.1 MW beam. The fourth FD module is conceived as a "Module of Opportunity", aimed at expanding the physics opportunities, in addition to supporting the core DUNE science program, with more advanced technologies. This document highlights the increased science opportunities offered by the DUNE Phase II near and far detectors, including long-baseline neutrino oscillation physics, neutrino astrophysics, and physics beyond the standard model. It describes the DUNE Phase II near and far detector technologies and detector design concepts that are currently under consideration. A summary of key R&D goals and prototyping phases needed to realize the Phase II detector technical designs is also provided. DUNE's Phase II detectors, along with the increased beam power, will complete the full scope of DUNE, enabling a multi-decadal program of groundbreaking science with neutrinos.

Contents

Executive summary

The preponderance of matter over antimatter in the early universe, the dynamics of the supernova neutrino bursts (SNBs) that produced the heavy elements necessary for life, the nature of dark matter, and whether protons eventually decay – these mysteries at the forefront of particle physics and astrophysics are key to understanding the evolution of our universe.

The Deep Underground Neutrino Experiment (DUNE) will address these questions in a multidecadal science program with its world-leading liquid argon (LAr) detector technology. The international DUNE experiment, hosted by the Fermi National Accelerator Laboratory (Fermilab), is designing, developing, and constructing a near detector (ND) complex at Fermilab (the near site) and a suite of four large detector modules 1300 km downstream at the Sanford Underground Research Facility (SURF) in South Dakota (the far site). These detectors will record neutrinos over a wide energy range, originating from a new high-intensity neutrino beamline at Fermilab. The modular far detector (FD) will also detect neutrinos produced by cosmic rays in the atmosphere and from astrophysical sources. The ND and FD will also be sensitive to a broad range of phenomena beyond the standard model (). The beamline as well as the excavations, infrastructure, and facilities for housing and supporting the DUNE detectors are provided by the Long-Baseline Neutrino Facility (LBNF).

The DUNE Collaboration was launched in 2015, following the recommendations of the 2013 update of the European Strategy for Particle Physics [1] and of the 2014 Report of the US Particle Physics Project Prioritization Panel (P5) [2]. DUNE and LBNF will complete this project in two phases, based on the availability of resources and the ability to reach science milestones. The latest P5 report released in December 2023 reaffirmed this vision [3].

The construction of the first project phase (Phase I), funded through commitments by a coalition of international funding agencies, is well underway. Its successful completion is currently the Collaboration's main priority. Excavation at the far site is complete, and fabrication of various beamline and detector components for Phase I is progressing well. The facilities currently being constructed by LBNF at both the near and far sites are designed to host the full scope (Phase I and Phase II) of the DUNE experiment.

The Phase II of DUNE that encompasses an enhanced 2.1 MW beam, a third and fourth far detector (FD) module, and an upgraded ND complex, is the subject of this paper. The primary objective of DUNE Phase II is a set of precise measurements of the parameters of the neutrino mixing matrix, θ_{23}, θ_{13}, Δm^2_{32}, and δ_{CP}, to establish Charge Conjugation-Parity Symmetry Violation (CPV) over a broad range of possible values of δ_{CP}, and to search for new physics in neutrino oscillations. DUNE also seeks to detect neutrinos from low-energy astrophysical sources. The additional mass brought by the Phase II FD modules would increase the statistics of a supernova burst signal and extend DUNE's reach beyond the Milky Way. The Phase II FD module design concepts would also perform sensitive searches for new physics with solar neutrinos by lowering the detection threshold in the relevant MeV-scale energy range and by reducing the background rates in this energy regime. Finally, Phase II will expand DUNE's new physics discovery reach via more sensitive searches for rare processes at the ND and FD sites, and for non-standard neutrino oscillation phenomena.

This world-class physics program requires an increase in the statistical power of the de-

tectors, which will be achieved by increasing the FD target mass with the additional modules and by exceeding 2 MW beam power, as recommended by the 2023 P5 committee in the US. In addition, an upgraded ND will be required to control systematic uncertainties of neutrino interactions on argon (or other selected FD target nuclei). The design of the Phase II FD modules will incorporate lessons learned from the construction of the Phase I modules, with the goal of optimizing physics performance, reliability, and cost.

The design of the third FD module will build on that of the second, the single-phase technology used for far detector module 2 (FD2), optimizing for performance and cost. This design implements -based horizontal anode planes at the top and bottom of the liquid-argon time-projection chamber (LArTPC) drift volume with a cathode plane in the middle, and a that hangs from the cryostat roof on which photon detectors will be mounted.

The fourth FD module is conceived as a "Module of Opportunity", which would allow to address new physics questions, in addition to the primary science program, with more advanced technologies. R&D for the design of the fourth module focuses primarily on optimization of readout techniques for both charge and scintillation light. It also considers the possibility of LAr doping. A possible improvement of the LAr charge-readout technology is the replacement of the PCB-readout by pixels or by an optical-based charge readout. A hybrid approach to detect Cherenkov and scintillation light is also under investigation, motivated by a complementary program of low-energy physics. All technologies proposed for the Module of Opportunity are expected to provide additional and complementary CPV sensitivity. In addition, background control is an essential ingredient of all FD module designs.

The Phase II ND will ensure that DUNE's sensitivity to oscillation parameters is not limited by systematic uncertainties. It is optimized for highly performing particle ID (PID), low tracking thresholds for protons and pions, and acceptance over a wide range of momenta. A magnetized gaseous argon time-projection chamber (GArTPC) at the near site, which will replace the Muon Spectrometer (TMS), will provide these constraints by measuring the interaction of neutrinos on argon with unprecedented precision due to its low thresholds. It offers superior discrimination between neutrinos and antineutrinos, as well as momentum determination of particles exiting the detector.

These plans fully align with the recommendations of the 2023 P5 report [3], which proposes a "second phase of DUNE (Phase II) with an early implementation of an enhanced 2.1 MW beam, a third far detector (module), and an upgraded near detector complex as the definitive long-baseline neutrino oscillation experiment of its kind," as well as "research and development (R&D) towards an advanced fourth detector."

The Phase II R&D program is a global effort with contributions from all DUNE partners. New collaborators are also invited to participate in the development and design of the new detector technologies. Part of the R&D described in this document is carried out within the framework of the European Committee for Future Accelerators (ECFA) detector R&D collaborations hosted by the European Laboratory for Particle Physics (CERN) and those being formed under the umbrella of the Coordinating Panel for Advanced Detectors (CPAD) in the US. DUNE has been designed to become the "best-in-class" global neutrino observatory. The Phase II far and near detector components, and the increased beam power, will enable a new era of precision and discovery in neutrino physics.

1   The elements of DUNE Phase II

The DUNE experiment at the LBNF was conceived in 2015, following the recommendations of the 2013 update of the European Strategy for Particle Physics [1] and of the 2014 Report of the US Particle Physics Project Prioritization Panel (P5) [2]. The 2014 P5 Report recommended developing, in collaboration with international partners, a coherent long-baseline neutrino program hosted by Fermilab, with a mean sensitivity to leptonic CPV of better than three standard deviations (σ) over more than 75% of the range of possible values of the CP-violating phase δ_{CP}. The 2014 P5 Report also recommended a broad program of neutrino astrophysics and physics Beyond the Standard Model (BSM) as part of DUNE, including demonstrated capability to search for SNBs and for proton decay. Likewise, the 2013 Update of the European Strategy for Particle Physics and its 2020 update [4] recommended that Europe and CERN (through its Neutrino Platform) continue to collaborate towards the successful completion of the .

The DUNE Collaboration and the Project have made substantial progress toward the realization of this enterprise, with the aim to start the scientific exploitation in 2029. Based on recent estimates, including a flux prediction using a fully-engineered neutrino beamline, the ultimate CPV measurement goal put forward by the 2014 P5 Report can be reached with an exposure of about 1000 kt·MW·yr. This can be achieved in about 15 years of physics data-taking (see Sec. 2.1), assuming that Phase II elements as described in this document are pursued. DUNE's neutrino astrophysics and BSM physics programs also benefit from multidecadal operations, to realize DUNE's full physics potential and achieve its scientific goals.

For the successful implementation of DUNE and LBNF, we need to consider the full extent of the available resources and funding profiles, provide a realistic estimate of the project costs, and achieve a clear understanding of the experimental configurations and exposures that are necessary to reach various physics milestones. As a result of this exercise, the DUNE Collaboration and the LBNF/DUNE-US Project have decided to pursue the experiment in two phases, as summarized in Table 1.

Parameter	Phase I	Phase II	Impact
FD mass	2 FD modules (20 kt fiducial)	4 FD modules (40 kt fiducial LAr equivalent)	FD statistics
Beam power	1.2 MW	Up to 2.3 MW	FD statistics
ND configuration	ND-LAr+TMS, SAND	ND-LAr, ND-GAr, SAND	Systematics

Table 1: A high-level description of the two-phased approach to DUNE. The ND-LAr detector, including its capability to move sideways (DUNE Precision Reaction-Independent Spectrum Measurement (DUNE-PRISM)), and the System for on-Axis Neutrino Detection (SAND) are present in both phases of the ND. Note that the non-argon options currently under consideration for Phase II near and far detectors are not shown.

In developing this two-phase strategy, we are guided by the original recommendations for the DUNE program, which remain valid and timely. The latest P5 report released in December 2023 reaffirmed this vision and strongly endorsed DUNE Phase I and II. In its report [3], the

P5 panel reaffirmed that the highest priority in the coming decade, independent of budget scenarios, is the completion of construction of existing projects which includes LBNF and DUNE Phase I, and the Proton Improvement Plan II (PIP-II).

The panel also strongly recommended constructing a portfolio of major projects, of which the second-highest priority was a "re-envisioned second phase of DUNE (Phase II) with an early implementation of an enhanced 2.1 MW beam (*aka*), a far detector module 3 (FD3), and an upgraded ND complex as the definitive long-baseline neutrino oscillation experiment of its kind." The panel also endorsed DUNE's fourth FD module (far detector module 4 (FD4)) concept as a "Module of Opportunity" and recommended exploring a range of alternative targets, including low-radioactivity argon, xenon-doped argon, and novel organic or water-based liquid scintillators, to maximize the science reach, particularly in the low-energy regime. An accelerated and expanded R&D program in the next decade is recommended for FD4 and if budget scenarios are favorable, initiation of construction is also recommended.

The overall project design for Phase I is complete, and this project phase is funded through commitments by several international funding agencies and CERN. LBNF excavation at the far site is complete, and fabrication of various beamline and detector components for Phase I are well underway. An important component of the DUNE strategy is that the facilities constructed by LBNF at both the near and far sites are designed to support the full scope of the DUNE experiment from the beginning. During Phase I, the facilities at the near site are thus constructed to support a >2 MW primary beamline and neutrino beamline, as well as a hybrid ND for all DUNE experimental phases. Likewise, the far site design includes underground halls for four FD modules.

The Phase I beamline will produce a wide-band neutrino beam with up to 1.2 MW beam power, designed to be upgradable to 2.4 MW. The Phase I ND includes a moveable LArTPC with pixel readout called ND-LAr, integrated with a downstream muon spectrometer called TMS [5], and an on-axis magnetized neutrino detector called SAND further downstream. The ND-LAr+TMS detector can be moved sideways over a range of off-axis angles and neutrino energies (DUNE-PRISM concept), for an optimal characterization of the neutrino-argon interactions.

The Phase I FD includes two LArTPC modules, each containing 17 kt of liquid argon (LAr). The far detector module 1 (FD1) is a horizontal drift time projection chamber (TPC), as developed and operated in at the CERN Neutrino Platform and similar in concept to the , , and detectors [6]. The FD2 is a vertical drift TPC. Its design capitalizes on the experience with the demonstrator at CERN. For the cryogenic infrastructure in support of the two LArTPC modules, Phase I will include two large cryostats (one per FD module), 35 kt of LAr, and three nitrogen refrigeration units.

While several options are under consideration for the Phase II components of the far and near site detectors, key elements have already been defined:

- A core component of Phase II is a More Capable Near Detector (). The main improvement to the ND is the addition of a magnetized high-pressure gaseous argon TPC (HPgTPC), surrounded by an electromagnetic calorimeter and by a muon detector called . ND-GAr will serve both as a new muon spectrometer for ND-LAr, replacing the TMS in this capacity, and as a new neutrino detector to study neutrino-argon interactions occurring

in the HPgTPC. In addition, upgrades to the ND-LAr and SAND systems are considered, as well as potential ND options in the case of a non-argon technology for FD4.

- Two additional FD modules, FD3 and FD4, will be added at the far site, for a total of four. The DUNE FD2 vertical drift technology forms the basis for the envisioned designs for FD3 and FD4. A non-argon option such as liquid scintillator (e.g.,) is also under consideration as an alternative technology for FD4. The cryogenic infrastructure at the far site will be upgraded for Phase II with a fourth nitrogen refrigeration unit to provide capacity for up to an additional 35 kt of LAr.

- A beam upgrade to increase the intensity to >2 MW. This is achieved by ACE-MIRT, which increases the frequency of beam spills by nearly a factor of two. While this is part of Phase II, it is possible to implement the upgrades that comprise ACE-MIRT before DUNE beam data taking begins.

The R&D underpinning the Phase II concepts is performed as part of a global program. The Detector R&D () collaborations hosted by CERN, which have been established as part of the European Committee for Future Accelerators (ECFA) roadmap, cover many of the detector concepts under study for DUNE Phase II. The DRD1 collaboration focuses on gaseous detectors and the DRD2 focuses on liquid detectors. Both collaborations have been formed recently. They are expected to grow with collaborators from within and outside Europe. Both the DRD1 and DRD2 collaborations were approved in December 2023 as official CERN experiments and held their first collaboration meetings in February 2024 at CERN. The ECFA DRD collaborations are strongly aligned with the Detector R&D collaborations (s) being formed under the Coordinating Panel for Advanced Detectors (CPAD) umbrella in the US. There is an active effort underway to coordinate activities across the CERN-hosted and US-based collaborations on synergistic areas of R&D toward achieving common scientific and technological goals.

This document is organized as follows. Section 2 covers the science that DUNE will pursue with Phase II, covering long-baseline neutrino oscillation physics, neutrino astrophysics, and BSM physics. A progress report on DUNE's Phase II far and near neutrino detectors is given in Sections 3 and 4, respectively. These two sections cover our current understanding of the detector requirements to carry out the Phase II physics goals, and a current snapshot of the main detector design options that are under consideration. These sections also summarize the critical R&D elements that remain to be addressed and the prototyping phases to be realized before Phase II detector technical designs can be finalized.

2   DUNE Phase II physics

This section discusses selected DUNE science drivers in the areas of long-baseline physics, neutrino astrophysics, and BSM physics that uniquely benefit from an improved performance of Phase II beam and detectors. The physics sensitivities are typically shown as functions of high-level figures of merit, such as exposure time, detector mass, background levels or detector acceptance, mostly without entering into the detector technology details. Specific benefits

brought by certain technologies are highlighted in Sections 3 and 4, together with the descriptions of such technologies.

2.1 Long-baseline neutrino oscillation physics

The DUNE experiment is designed to measure the rate of appearance of electron (anti)neutrinos (ν_e or $\bar{\nu}_e$) and the rate of disappearance of muon (anti)neutrinos (ν_μ or $\bar{\nu}_\mu$), as functions of neutrino energy in a wide-band beam. DUNE is sensitive to all the parameters governing $\nu_1 - \nu_3$ and $\nu_2 - \nu_3$ mixing in the three-flavor model: θ_{23}, θ_{13}, Δm^2_{32} (including its sign, which is given by the neutrino mass ordering), and the phase δ_{CP}.

During Phase I, DUNE can accumulate approximately $100\,\mathrm{kt \cdot MW \cdot yr}$ of data in five years. This corresponds to ≈ 400 ν_e and 150 $\bar{\nu}_e$ candidates in the FD, depending on the value of the oscillation parameters and assuming equal fractions of neutrino and antineutrino running. While these data sets will still be statistically limited once Phase I ND systematic constraints are accounted for, they are sufficient to conclusively determine the neutrino mass ordering at $> 5\sigma$ significance, regardless of the true parameter values. If CPV is nearly maximal ($\delta_{\mathrm{CP}} \approx \pm\pi/2$), DUNE can establish CPV at 3σ in Phase I. DUNE will also make measurements of the disappearance parameters Δm^2_{32} and $\sin^2 2\theta_{23}$ that improve upon current uncertainties. However, the statistics of Phase I are too low to determine the octant of θ_{23} or to establish CPV except in the most favorable scenarios.

2.1.1 Goals of the oscillation physics program of Phase II

The goals of the oscillation physics program of Phase II are high-precision measurements of all four parameters: θ_{23}, θ_{13}, Δm^2_{32} and δ_{CP}, to establish CPV at high significance over a broad range of possible values of δ_{CP}, and to test the three-flavor paradigm as a way to search for new physics in neutrino oscillations. Achieving these goals requires $600 - 1000\,\mathrm{kt \cdot MW \cdot yr}$ of data statistics, depending on the measurement. This can be achieved by operating for $6 - 10$ additional calendar years with a greater than $2\,\mathrm{MW}$ beam and a FD of $40\,\mathrm{kt}$ LAr equivalent fiducial mass. Without doubling the FD mass and the beam intensity, the additional time required would be $24 - 40$ years.

In particular, the long-baseline sensitivities presented below make the following assumptions concerning the time evolution of the protons on target (POT) delivery, the fiducial FD mass and the ND systematic constraints. The beam power evolution is based on the assumptions of the Fermilab Proton Intensity Upgrade Central Design Group [7]. The average beam power during the first year of beam operations is $1.1\,\mathrm{MW}$, increasing to $1.6\,\mathrm{MW}$ during year 2, thanks to ACE-MIRT upgrades [7]. Further beam optimizations are assumed in subsequent years, yielding a beam power of $2.3\,\mathrm{MW}$ after approximately 15 years. The assumed POT delivery also includes a 57% average uptime [8]. As regards the fiducial FD mass, the experiment is assumed to take data with two FD modules ($20\,\mathrm{kt}$ fiducial mass) during the first three years. The FD3 and FD4 modules are assumed to become fully operational in years 4 and 6, respectively, to provide a nominal fiducial FD mass of $40\,\mathrm{kt}$. Figure 1 shows how the accumulated exposure, expressed in $\mathrm{kt \cdot MW \cdot yr}$ units, varies as a function of time with this assumed staging scenario. The 600 and
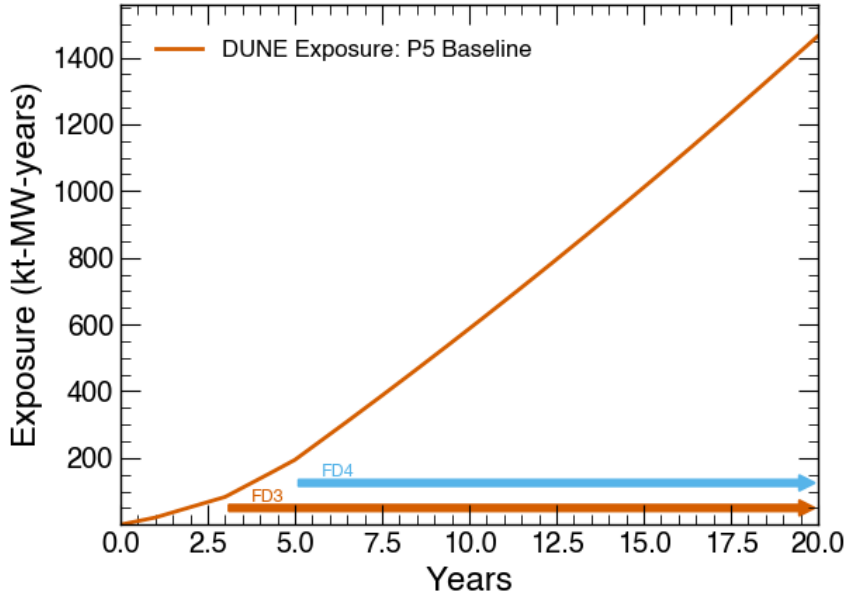
Figure 1: DUNE integrated exposure, in kt·MW·yr units, as a function of time assumed for the long-baseline (LBL) sensitivity results presented in this section. The integrated exposure is built from the beam power and FD mass staging assumptions discussed in the text.

1000 kt·MW·yr integrated exposure milestones of DUNE Phase II appear within reach after approximately 10 and 15 years of beam plus detector operations, respectively. Finally, it is assumed that the Phase I ND systematic constraints will be in effect up to year 6, with the improvements from Phase II ND starting in year 7. The new constraints, as they gradually improve over the course of two years to their final values, will be applied to all past FD data.

The precision of the high-statistics measurements is ultimately limited by the systematic uncertainties. To achieve DUNE's science goals will therefore require unprecedented control of systematic uncertainties. The significance for DUNE to establish CPV is shown as a function of time in Figure 2. Phase II, with its full 1000 kt·MW·yr exposure, will enable DUNE to establish CPV at $> 3\sigma$ over 75% of possible δ_{CP} values, and measure it at a precision of $6° - 16°$, depending on the true value.

DUNE can also measure the angle θ_{23} with world-leading precision and determine the octant if it is sufficiently non-maximal. The measurements of θ_{13} and Δm_{32}^2 will approach the precision of the current measurement from Daya Bay [9] and the planned measurement from JUNO [10], respectively, which are all performed with a different neutrino flavor, over a different baseline, and at a different energy. Comparing the results obtained over this wide range of conditions will provide a more complete and robust test of the three-flavor model. The resolutions to δ_{CP}, $\sin^2 2\theta_{13}$, and $\sin^2 \theta_{23}$ are shown as a function of exposure in Figure 3.

DUNE is also sensitive to BSM physics that impacts neutrino oscillations, including non-unitary mixing, non-standard interactions, violation of charge, parity, and time reversal sym-
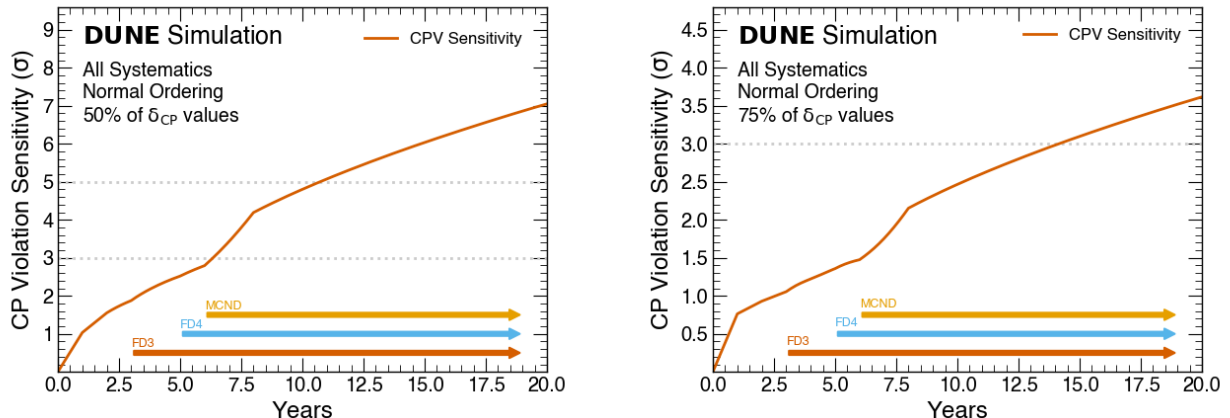
Figure 2: The significance for DUNE to establish CPV for 50% (left panel) and 75% (right) of δ_{CP} values as a function of running time. See text for details about the assumed staging scenario.

metry (CPT), and the possible existence of additional neutrino species (see Section 2.3).

2.1.2   The role of Phase II detectors

The two additional modules, FD3 and FD4, will provide the additional exposure and improved statistical precision that is critical to achieve the full δ_{CP} sensitivity (Figure 2). They also offer the opportunity to improve the neutrino energy reconstruction and the neutrino interaction classification with enhanced detector technology, for example through optimized charge and photon readout systems (Sec. 3.3). It is crucial that the data from these modules be combined with data from FD1 and FD2, with the systematic constraints from the ND applied to all FD modules. For this reason, the most straightforward approach is for FD3 and FD4 to be LArTPCs, so that DUNE would immediately benefit from the ν-Ar measurement program of the ND. The oscillation sensitivities presented in Figures 2 and 3 assume the performance of the Horizontal Drift module using an end-to-end simulation and reconstruction. The alternative LArTPC concepts being considered for FD3 and FD4 are expected to have similar, and perhaps slightly improved performance for GeV-scale beam neutrinos, so the existing simulations serve as a conservative estimate of the eventual sensitivity.

If FD4 is not a LArTPC, the impact on the long-baseline oscillation program is less straightforward. For the THEIA concept discussed in Section 3.5, the performance is estimated using a reconstruction based on the fiTQun package [11], and a boosted decision tree (BDT) [12]. The analysis is less sophisticated than the DUNE TDR sensitivities [8], using the GLOBeS package to implement systematics as normalization shifts, but suggests that the sensitivity is comparable to what can be achieved in a single LArTPC module. It does not yet make use of the additional information potentially offered by the scintillation component, which can provide tagging of neutrons and other sub-Cherenkov threshold particles, for improved event identification and enhanced calorimetry. Combining a non-LArTPC module with LAr measurements
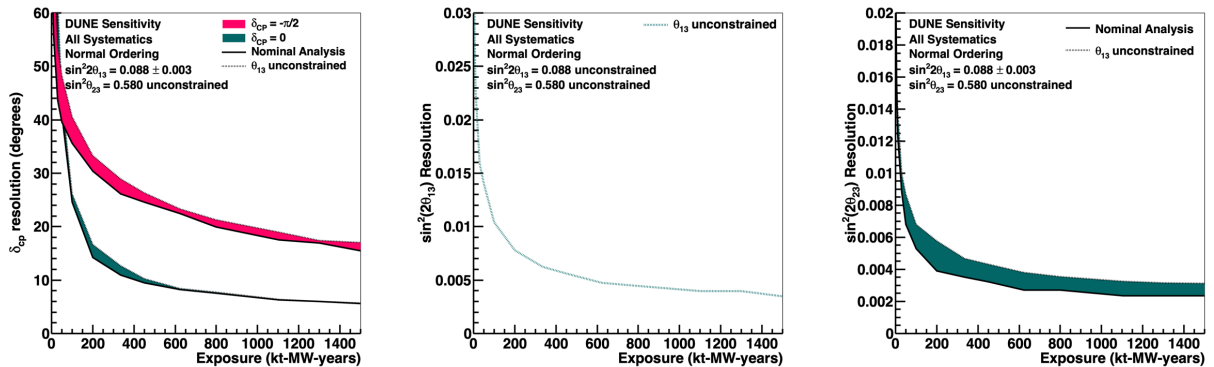
Figure 3: The resolutions to δ_{CP} (left), $\sin^2 2\theta_{13}$ (center), and $\sin^2 \theta_{23}$ (right), shown as a function of exposure in kt-MW-yrs, assuming the full constraint from the ND, including MCND. The ultimate precision of DUNE requires an exposure greater than 600 kt-MW-yrs, which requires FD3 and FD4 to be built in a reasonable timescale.

could potentially provide a cross-check of extracted oscillation parameter values with different detector systematics. A non-LAr FD4 would require a dedicated ND to constrain neutrino cross section uncertainties and detector response on the FD4 nuclear target to a similar precision as the LArTPC constraints. Near detector options for non-LAr FD modules are discussed in Sec. 4.4.

The role of MCND (Section 4.2) is to ensure that DUNE can achieve the required level of systematic uncertainties for Phase II and to ensure that the results are not systematically limited. It would replace the TMS with a detector that has its own standalone physics capabilities, including constraining neutrino-argon cross section uncertainties and expanding the BSM reach of the ND, while also measuring muons exiting the ND-LAr detector. Further study of the ultimate performance of the Phase I ND is important for scoping the Phase II ND.

2.2 Neutrino astrophysics and other low-energy physics opportunities

DUNE's broad physics program includes the detection of neutrinos from astrophysical sources in the MeV energy range [13], primarily neutrinos from the sun and a SNB. With argon as active material, DUNE will be primarily sensitive to the astroparticle ν_e flux for energies below 100 MeV and above 5 MeV due to the relatively large ν_e charged current (CC) cross section for the process: $\nu_e + {}^{40}\mathrm{Ar} \rightarrow e^- + {}^{40}\mathrm{K}^*$. DUNE will be unique in this regard, making the experiment highly complementary to existing and proposed experiments for the next decades aiming for similar astrophysical neutrino measurements in the 10s of MeV regime: JUNO [14], Hyper-Kamiokande [15], and dark matter detectors [16, 17]. This section highlights the improvements a LArTPC FD module from Phase II would bring. It also includes a summary of the advantages of a water-based liquid scintillator, that would be sensitive primarily to the $\bar{\nu}_e$ flux, within the Phase II program.

21

DUNE Phase I will be sensitive to solar and SNB neutrinos, achieving an energy resolution of $(10-20)\%$. The visible energy threshold will be > 5 MeV for SNB neutrinos and higher for solar neutrinos, which do not arrive in a short pulse. Large LArTPC detectors have demonstrated much lower charge thresholds, ~ 100 keV [18], but Phase I sensitivity will be limited to > 5 MeV due to light collection performance and radiological backgrounds. Thus, innovation on these fronts can lower visible energy thresholds for astrophysical neutrinos by as much as two orders of magnitude while also improving energy resolution. Lower thresholds would also fundamentally expand the low-energy physics opportunities with DUNE Phase II. Figure 4 shows a selection of potential signatures of astrophysical or other beam-unrelated origin with DUNE Phase II, together with relevant backgrounds.
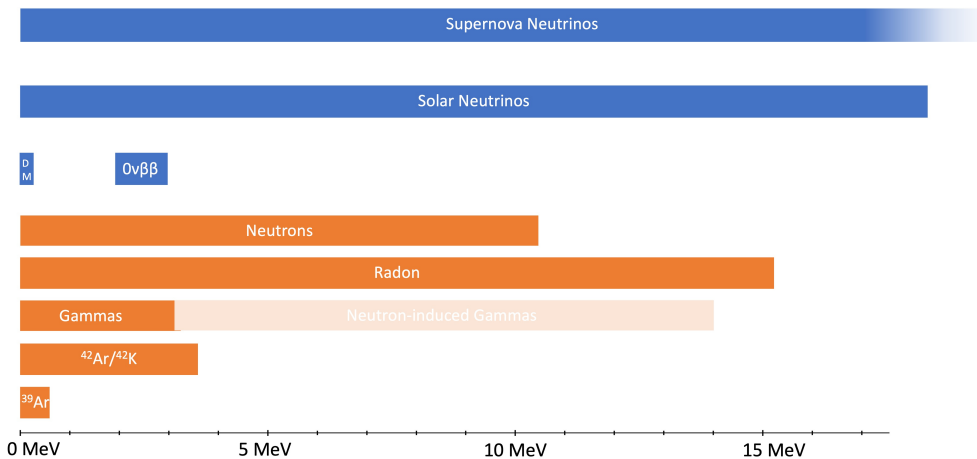
Figure 4: Detectable energy ranges in DUNE LArTPC FD modules for potential < 20 MeV signatures of astrophysical or other non-beam-related origin (blue), and for relevant, overlapping backgrounds (orange). The DM signature refers to weakly-interacting massive particle (WIMP) direct dark matter searches. Adapted from [19].

2.2.1 SNB neutrinos

DUNE will be part of a collaborative, multi-messenger network of neutrino and optical telescopes studying the next galactic core-collapse supernova (CCSN). With different flavor sensitivity from other large experiments, DUNE will provide complementary information about the collapse. DUNE's ν_e sensitivity is most striking at the earliest times of the SNB, which is dominated by ν_e emission from neutronization in the stellar core, as shown in the top panel of Figure 5. During Phase I, DUNE will already be able to detect neutrinos from a CCSN with energies > 5 MeV [20], albeit with lower statistics. The larger mass of Phase II represents a significant step in extending the detector's sensitivity to a SNB signal, since the burst trigger efficiency, reconstruction of the supernova direction (bottom right panel of Figure 5), and precise measurement of the supernova spectral parameters (bottom left panel of Figure 5))are dominated by the number of neutrino interactions in the detectors. While the expected event rate varies significantly among supernova models, the 40 kt (fiducial) DUNE detector would be

22

expected to observe ≈ 3000 neutrinos from an SNB at a distance of $10\,\mathrm{kpc}$, just beyond the center of the Milky Way [20].
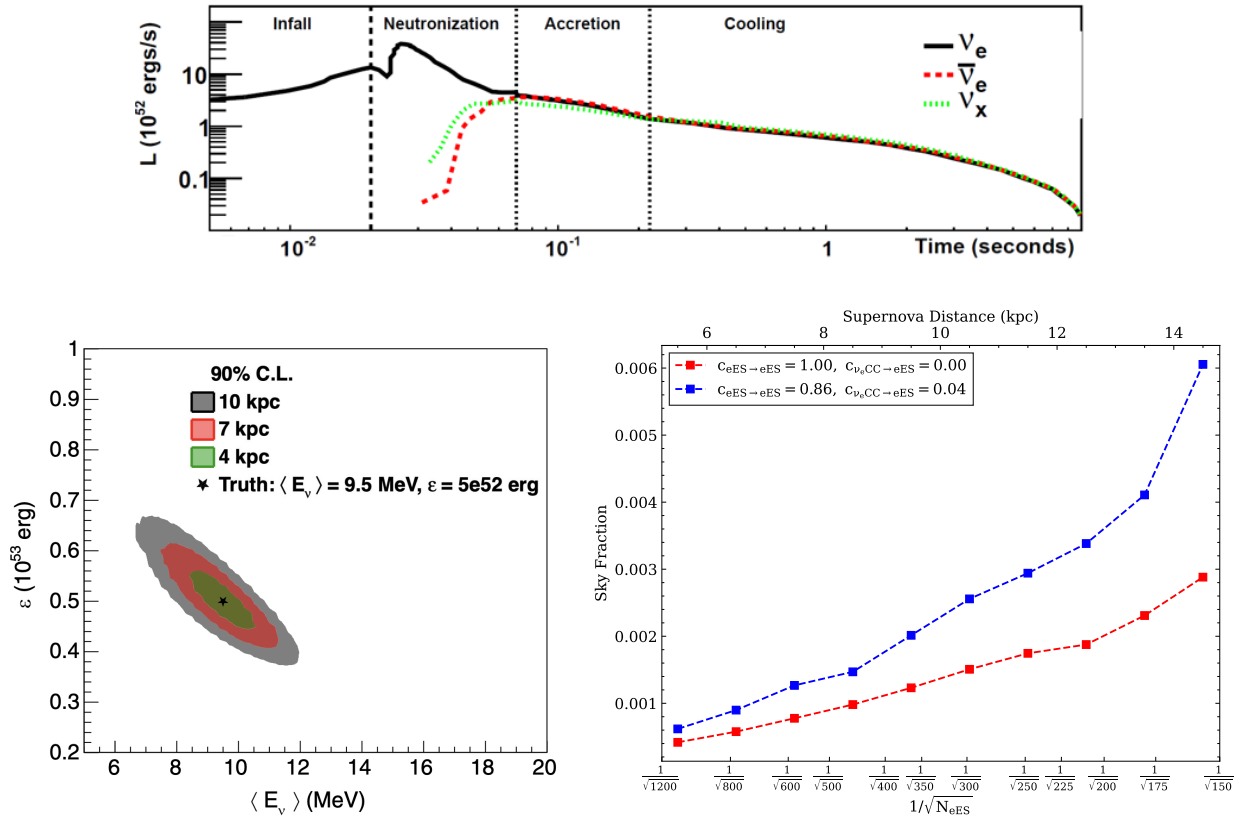
Figure 5: The total luminosity of neutrinos released during CCSN from [21] (top). Sensitivity regions in mean neutrino energy (related to the temperature of supernovae) and neutrino luminosity space for three different supernova distances from [22] (bottom left). DUNE's reconstruction of the direction of a SNB in terms of the fraction of sky allowed at 68% confidence, as a function of recorded number of neutrino-electron scattering events as well as the corresponding supernova distance from [23] (bottom right).

The modular nature of DUNE's FD makes the experiment ideal for SNB triggering and contributing to SuperNova Early Warning System (SNEWS) [24]. Each FD module will independently forward a CCSN alert to SNEWS which will be made available to optical astronomers. Deployment of additional detectors in Phase II will effectively ensure that at least one FD module is operational whenever a SNB arrives at the detector. With all modules taken together, the increased mass from Phase II will allow DUNE to trigger on further supernovae, increasing coverage in the neighborhood beyond the Milky Way (e.g., in the Large and Small Magellanic Clouds).

As the neutrino signal escapes a core-collapse supernova hours before the first optical signal, pin-pointing the source of the SNB is fundamentally important to facilitate optical observation of the initial stages of the supernova. The electron tracks from neutrino-electron elastic scatter-

ing, a sub-dominant interaction channel for SNB detection, are nearly parallel to the incoming neutrino flux and can thus be used to reconstruct the neutrino direction. Supernova pointing leverages the excellent tracking capabilities of a LArTPC to identify neutrino-electron scattering events yielding a pure sample of this low-rate channel. The increased mass from Phase II is critical for realizing DUNE's full potential. Using a typical flux model, the full 40 kt detector would expect 326 neutrino-electron scattering events compared to 163 in Phase I [23]. This reduces the field-of-view for optical follow-up searches following a SNB signal from 0.26% to 0.14% of the total sky at $1\,\sigma$ as shown in the bottom right panel of Figure 5. A Phase II module with pixelated charge readout would also improve SNB pointing resolution by improving the 3D reconstruction of low-energy electron tracks.

The neutrino mass ordering has a strong impact on the expected signal at early times (neutronization burst) when electron-type neutrinos dominate the neutrino flux at production (see Figure 6 for expected event rates in DUNE). Neutrino flavor transformations can be induced by neutrino-neutrino scattering and collective modes of oscillation [25]. These effects will leave imprints on the neutrino signal and can be used to study these phenomena experimentally. These effects will test fundamental neutrino properties by measuring the neutrino self-interaction strength [26]. DUNE will also provide competitive constraints on the absolute neutrino mass via measurements of the time of flight from the supernova to Earth [27].

With argon's ν_e flavor sensitivity, DUNE will uniquely probe the neutrino component of the diffuse supernova neutrino background (DSNB) [28] – Phase II will be critical for such a low-rate search by increasing argon mass.
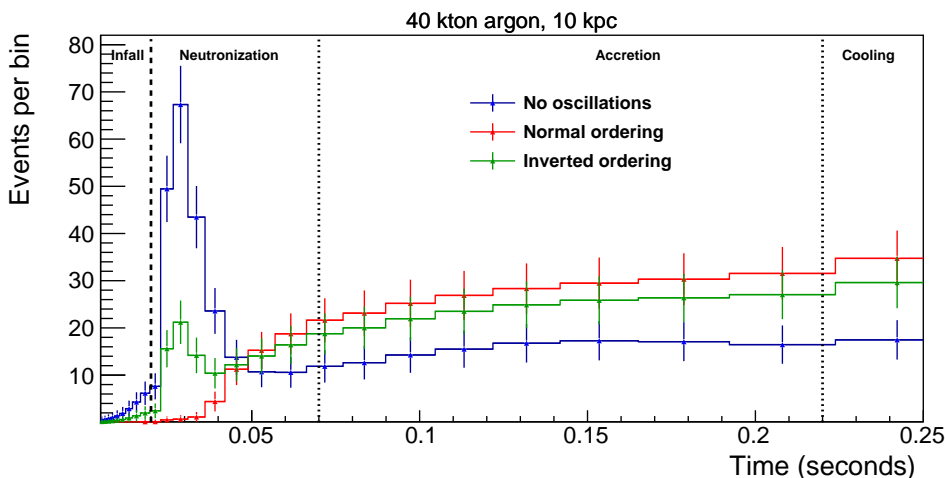
Figure 6: Expected event rates from [20] as a function of time for the electron-capture supernova model in [29] and for 40 kt of argon during early stages of the burst. Shown are the event rate for the unrealistic case of no flavor transitions (blue) and the event rates including the effect of matter transitions for the normal (red) and inverted (green) mass orderings. Error bars are the expected statistical uncertainty in each (varying) time bin.

With significant increase of the photodetector area, e.g., 10% coverage with silicon photomultipliers (SiPMs) [19], and use of ^{39}Ar-depleted argon, a DUNE Phase II LArTPC module

would be sensitive to faint light flashes from Coherent Elastic Neutrino-Nucleus Scattering (CEνNS) interactions on argon during a SNB. The "CEvNS glow" from a supernova would be observed as an increase of low-PE flashes observed through the duration of the burst. As a neutral current (NC) process, this channel is sensitive to all neutrino flavors, thus giving orthogonal information to the MeV-scale ν_e CC interactions. Importantly, CEvNS glow allows DUNE to determine the supernova neutrino fluence independent of neutrino oscillation uncertainties.

A water-based liquid scintillator module (e.g., THEIA) would sacrifice part of the SNB ν_e statistics for a significant increase in $\bar{\nu}_e$ events through inverse β decay, with a threshold of $\sim$2 MeV. Such a module would detect approximately 5000 $\bar{\nu}_e$ interactions from a SNB at 10 kpc distance. The scintillation light would provide a tag for neutrons to allow separation between inverse β decay events and directionally-sensitive elastic scattering reactions. Using the high light output from the scintillation, such a module would also be sensitive to pre-supernova neutrinos [30], alerting neutrino experiments to an upcoming SNB.

2.2.2 Solar neutrinos

After more than a half century of study, there remain important open questions in particle and astrophysics that solar neutrino measurements can potentially resolve. This is due in large part to the precision tracking capabilities of the DUNE LArTPC detectors. In addition, because of argon's dominant ν_e CC interaction channel, the detected energy will correlate strongly with the incoming neutrino energy. With these advantages, DUNE promises excellent potential for improved measurements [31]. Initial studies suggest DUNE Phase I can select a sample of ^{8}B solar neutrinos that would improve upon current solar measurements of Δm_{21}^2 [32] via the precise measurement of the day-night flux asymmetry induced by Earth matter effects. DUNE Phase I can also make the first observation at $>5\sigma$ of the "hep" flux produced via the ^{3}He + p $\rightarrow$ ^{4}He + e$^+$ + ν_e nuclear fusion.

The energy resolution of DUNE Phase I, $(10 - 20)\%$, could be improved down to $\approx 2\%$ through improvements to the Phase II photon detection system (PDS). This radically improves determination of solar neutrino parameters. The measurement of the solar mass splitting Δm_{21}^2 requires precisely measuring the energy dependence of the neutrino oscillation pattern. A single module with 2% resolution would make this measurement better than four modules with Phase I energy reconstruction performance.

For beam-unrelated FD events, reconstructed photon flashes are used to select events within the detector fiducial volume and to correct ionization charge loss along drift, greatly suppressing backgrounds and improving energy reconstruction, respectively. In Phase I, DUNE's solar neutrino reach will be limited by non-perfect light flash reconstruction and by radiological backgrounds, primarily neutron capture on argon, which can also confuse light-charge matching. As described in Section 3, upgrades to the photon detection can increase DUNE light yield in Phase II by a factor of five or more. This will make light flashes from solar neutrino signals more apparent and improve vertex reconstruction from the flash to simplify the light-charge matching algorithm. Neutron capture on ^{40}Ar could be vetoed by rejecting optical flashes that reconstruct near the 6.1 MeV Q-value and further mitigated by installation of passive shielding. Together, these would reduce the solar neutrino detection threshold for a Phase II FD module.

DUNE's ν_e CC signal makes it ideal for measuring the energy dependence of the solar electron-neutrino survival probability, P_{ee}. With a visible energy threshold at or below $5\,\text{MeV}$ for solar neutrinos, possible with some technology choices outlined in Section 3, DUNE will probe the upturn in P_{ee}. This is the transition region between the low-energy regime where vacuum solar oscillations dominate and the high-energy regime where the oscillation probability is determined by Mikheyev-Smirnov-Wolfenstein effect (MSW) matter effects [33] inside the sun. The same MSW matter effects, but in the earth, are central to DUNE's measurements of neutrino mixing parameters with long-baseline oscillation measurements. A significant increase in photodetector coverage would allow measurements of carbon nitrogen oxygen (CNO) solar neutrinos that could distinguish between solar metallicity models [19].

A FD module based on THEIA would also be sensitive to solar neutrinos, through the neutrino-electron scattering channel. The THEIA technology is sensitive to both scintillation and Cherenkov light from low-energy neutrinos – thus simultaneously providing low thresholds and event directionality. Such a module could possibly probe the solar neutrino transition region to even lower energies, near $2\,\text{MeV}$.

2.2.3 Other low-energy physics opportunities

Through heavy fiducialization and improved energy resolution from increased photodetector coverage, DUNE's low-energy physics can reach beyond astrophysical neutrinos in Phase II.

Planning is underway for future WIMP dark matter experiments. These liquid noble detectors will scale up the current technologies active target masses with the goal to reach the so-called "neutrino fog", that is the cross-section below which the potential discovery of a dark matter signal is slowed due to the uncertainty in the irreducible background from the coherent elastic scattering of astrophysical neutrinos with nuclei [34]. Leading upcoming projects include the xenon-based XLZD experiment [35], and the argon-based DarkSide-20k [36] and ARGO experiments. A DUNE FD module could perform a competitive WIMP dark matter search complementary to future argon dark matter experiments [37]. Particularly interesting would be the sensitivity to the annual modulation of the WIMP signal, which due to DUNE's large target mass would allow a rapid confirmation of any observed signal in the current so-called generation-2 experiments [19]. A 10% photodetector coverage with SiPMs could give the necessary threshold of $\sim100\,\text{keV}$. Such low thresholds would also require operating the detector module with underground argon depleted in the ^{39}Ar isotope, for background mitigation.

By introducing a large mass fraction of ^{136}Xe or ^{130}Te to a Phase II FD module based on LArTPC or THEIA technology, respectively, DUNE could also perform neutrinoless double-β decay ($0\nu\beta\beta$) searches. The neutrinoless double β decay community has laid out a strategic plan [38] that calls for a diverse R&D program with sensitivity beyond next-generation ton-scale experiments. DUNE Phase II can contribute toward this long-term $0\nu\beta\beta$ effort, in connection with, and as a possible evolution of, the existing $0\nu\beta\beta$ program. A DUNE THEIA module loaded with ^{130}Te could be a natural evolution of the loaded liquid scintillator technique currently pursued by SNO+ [39] and KamLAND-Zen [40]. Similarly, a ^{136}Xe-doped DUNE LArTPC module with sufficiently good energy resolution (σ) of order 2% [41] could expand on liquid xenon TPC strategies currently employed by nEXO [42]. Such a LArTPC $0\nu\beta\beta$ module would

also require sourcing very large amounts of underground argon, in order to mitigate ^{42}Ar-induced backgrounds.

Finally, thanks to its $\bar{\nu}_e$ sensitivity, a THEIA module would also observe geo-neutrinos and reactor neutrinos [12].

2.3 Physics beyond the Standard Model

DUNE has discovery sensitivity to a diverse range of physics Beyond the Standard Model (BSM), which is complementary to those at collider experiments and other precision experiments. BSM physics accessible at DUNE may be divided into three major areas of research: rare processes in the beam observed at the ND (for example heavy neutrinos, light dark matter, or new physics that could enhance neutrino trident production), rare event BSM particle searches at the FD (for example inelastic boosted dark matter, nucleon decays), and non-standard neutrino oscillation phenomena (for example sterile neutrino mixing, non-standard interactions). In the following, we give examples where DUNE Phase II will bring additional unique sensitivity with respect to Phase I and to the performance of current experiments [43].

2.3.1 Rare event searches at the near detector

The high intensity and high energy of the LBNF proton beam enables DUNE to search for a wide variety of long-lived, exotic particles that are produced in the target and decay in the ND. Heavy neutral leptons (HNLs) and Axion-like particles (ALPs) are examples of well-motivated searches that can be carried out in DUNE. Low density detectors are best suited for such a search, because the signal scales with the detector volume while the background (predominantly due to Standard Model neutrino interactions) scales with detector mass. In Phase I, SAND can perform such searches with a density of ~ 0.2 g/cm^2. In Phase II, the ND-GAr substantially improves the reach for these searches with even lower density and a larger volume. Signal efficiencies and background rates after selection cuts are found to improve significantly in Phase II, thanks to ND-GAr [46]. Background rates generally depend on the decay final state. In some cases background-free searches appear possible, for example for channels involving pairs of muons in the final state.

For HNLs, the decay rates are proportional to $|U_{\alpha N}|^2$ in the case of single dominant mixing, where $\alpha = e, \mu, \tau$ and the matrix $U_{\alpha N}$ specifies the mixing between the active SM neutrinos α and the new heavy states N. Figure 7 shows the combined sensitivity for HNL decay channels probing each individual mixing matrix element $|U_{\alpha N}|^2$, as a function of the HNL mass and under the assumption of no background (result adapted from [44]). As can be seen from the figure, DUNE is world-leading at masses below m_τ, complementary to the LHC heavier mass searches. In addition, DUNE may have the potential to explore further the portion of parameter space predicted by Type I seesaw models. Other phenomenological studies [47, 48, 49, 50] confirm the potential of the DUNE Phase II ND for HNL searches.

ND-GAr is also sensitive to ALPs with masses between 20 MeV and 2 GeV [51, 46]. DUNE is expected to improve over present constraints on ALP particles particularly for ALP masses below the kaon mass. For a wide range of ALP lifetimes, the sensitivity improvement would
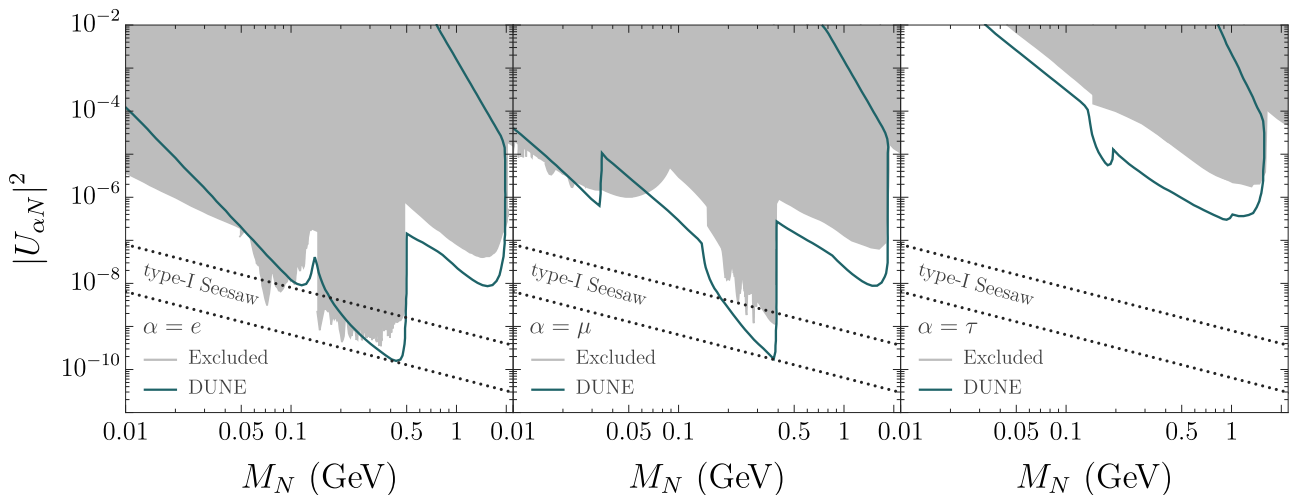
Figure 7: Expected DUNE ND sensitivity at 90% CL to the mixing $|U_{\alpha N}|^2$ as a function of the mass M_N, for a total of $7.7 \cdot 10^{21}$ POT, and combining all the possible HNL decay channels leading to visible states in the detector. Backgrounds are assumed to be negligible. Results are shown for a HNL coupled exclusively to: e (left panel), μ (middle panel), and τ (right panel). The dotted gray lines enclose the region of parameter space where a Type I seesaw model could generate light neutrino masses in agreement with oscillation experiments and upper bounds coming from the latest KATRIN results on β-decay searches. A negligible background level after cuts and a signal selection efficiency of 20% was assumed for this analysis. Figure adapted from [44] to include the latest excluded areas from existing results; obtained with the `HNLimits` [45] package. All sensitivity curves and currently excluded areas assume Dirac neutrinos, and that the HNL only couples to one of the charged leptons as indicated by the flavor index of the panel, while the other two mixings are set to zero.

span many orders of magnitude.

Another rare event search at the ND is neutrino trident production, that is, the production of a pair of oppositely-charged leptons through the scattering of a neutrino on a heavy nucleus. Neutrino trident production is a powerful probe of BSM physics in the leptonic sector [52, 53]. The Standard Model (SM) expectation is that the ND will collect approximately a dozen of these rare events per ton of argon per year [54, 55]. To date, only the dimuon final-state has been observed, although with considerable uncertainties. The main challenge in obtaining a precise measurement of the dimuon trident cross-sections ($\nu_\mu \to \nu_\mu \mu^+ \mu^-$ and $\bar{\nu}_\mu \to \bar{\nu}_\mu \mu^+ \mu^-$) at DUNE will be the copious backgrounds, mainly consisting of CC single-pion production events ($\nu_\mu N \to \mu \pi N'$), as muon and pion tracks can be easily confused. ND-GAr will tackle this search by improving muon-pion separation through dE/dx measurements in the HPgTPC and the calorimeter system, and ND-GAr's magnetic field will significantly improve signal-background separation by tagging the opposite charges of the two muons in the final state.

2.3.2   Rare event searches at the far detector

Phase II will also enhance BSM searches at the FD, and in particular searches that are expected to be nearly background-free at the scale of the experiment's full exposure. In such cases, the decay or scattering rate sensitivity will be inversely proportional to the FD exposure (in kt·yr), and added exposure in Phase II FD modules will be significant. Background-free (or quasi-background-free) searches at the FD may include baryon-number-violating processes. For example, current estimates [43] for the $p \to K^+ \bar{\nu}$ search yield a mean background rate expectation of 0.4 events for a 400 kt·yr exposure at the FD.

2.3.3   Non-standard neutrino oscillation phenomena

DUNE is sensitive to neutrino oscillation scenarios beyond the standard three-flavor picture, including sterile neutrinos, non-standard interactions, and PMNS non-unitarity. These searches rely on both the ND and FD, and require high precision and very large exposures, such that both the Phase II ND and FD are important.

In addition to searching for BSM modifications to the muon and electron neutrino signals, DUNE also has a unique capability to search for tau neutrino appearance because the broadband LBNF beam has significant flux above the ~ 3.5 GeV tau charged-current threshold. Searches for tau appearance would enable DUNE to directly constrain the tau elements of the PMNS matrix, and also to search for anomalous ν_τ appearance, which may point to mixing with HNLs or non-standard interactions [56, 57]. This would become particularly interesting if hints of non-unitarity are observed in the muon and electron channels. The τ lepton from beam ν_τ CC interactions is not directly observable in the DUNE detectors due to its short 2.9×10^{-13} s lifetime. However, the final states of τ decays ($\sim 65\%$ into hadrons, $\sim 18\%$ into $\nu_\tau + e^- + \bar{\nu}_e$, and $\sim 17\%$ into $\nu_\tau + \mu^- + \bar{\nu}_\mu$) can be detected.

The LBNF beamline is designed such that the target and the horn focusing system can be replaced. The LBNF/DUNE Construction Project will provide targets and horns designed for 1.2 MW operation, in the standard low-energy beam tune configuration optimized for CPV measurements. New ACE-MIRT upgrades designed for >1.2 MW operation will be needed, and could provide the capability to run with a higher-energy beam tune optimized for detection above the τ production threshold. Studies indicate that the ν_τ charged-current interaction rate will more than double at the FD in this case, compared to the standard LBNF beam optimized for CPV [58]. Running with the high-energy tune is not currently planned, but could provide further physics reach for DUNE in Phase II.

At the ND, the baseline is far too short for $\nu_\mu \to \nu_\tau$ oscillations to occur within a three-flavor scenario. However, ν_τ originating in rapid oscillations driven by sterile neutrinos could be detected. A challenge is that for the tau decay to muon channel, a large fraction of the signal is at very high energy. In Phase I, the TMS cannot reconstruct momentum by curvature, and is limited to measuring $T_\mu < \sim 6$ GeV by range. It may be possible to search for anomalous tau appearance in SAND, which is sensitive to higher energy muons by curvature but has much smaller target mass. In Phase II, ND-GAr provides a magnetized spectrometer for ND-LAr which can reconstruct very high-energy muons by curvature. With one year of data with the Phase II ND, preliminary studies show that DUNE's reach in this channel extends beyond the

present strongest limits from NOMAD [59].

3 The DUNE phase II far detector

3.1 Introduction

The primary objective of the DUNE Phase II FD is to increase the fiducial mass of DUNE to at least the originally planned 40 kt LAr-equivalent mass. For long-baseline neutrino oscillations, it is critical that all four FD modules be compatible with the systematic constraints of the ND. Non-LAr options for the Phase II FD would require corresponding additions or changes to the ND complex in order to achieve a comparable level of systematic uncertainty. These options are described in Section 4.4. For MeV-scale physics, the additional mass would double the number of expected neutrino interactions in a SNB and extend the reach to supernovae beyond the Milky Way. An exposure of hundreds of kt-yrs is required to improve upon oscillation parameter measurements with solar neutrinos. Most BSM searches also require very long exposures to be competitive.

Enhancements to the detector design have the potential to improve the DUNE program by lowering the threshold for MeV-scale neutrinos or by reducing the background rates in this energy regime. Phase II also presents opportunities to expand the DUNE science program to new areas while preserving the essential core measurement capabilities. The design of the Phase II FD modules will also incorporate lessons learned from the construction of Phase I, in particular the vertical drift FD2, optimizing performance and cost.

3.2 The vertical drift detector design

The single-phase vertical drift technology as implemented in ProtoDUNE-VD and planned for FD2 [60] (Figures 8 and 9) draws from the strengths of the DUNE prototypes [61] and ProtoDUNE-SP [62] as well as the previous detectors ICARUS and MicroBooNE. Relative to the well-established single-phase (SP) horizontal drift design that is based on large wire plane assemblies, the vertical drift design simplifies detector construction and installation, reducing overall detector costs. The vertical drift module uses most of the same structural elements as the ProtoDUNE-DP design (e.g., charge-readout planes (CRPs) to form the anode planes, and the field cage that hangs from the cryostat roof), and is constructed of modular elements that are much easier to produce, transport, and install.

The cathode at the vertical mid-plane of the detector is suspended from the top CRP support structure and subdivides the detector into two vertically stacked, 6.5 m high drift volumes, with CRP readout for both the top and bottom drift volumes. The top CRPs are suspended from ports on the cryostat roof whereas the bottom CRPs are supported by feet on the cryostat floor.

The important features of the vertical drift design, particularly in comparison with the FD1 horizontal drift design, are:
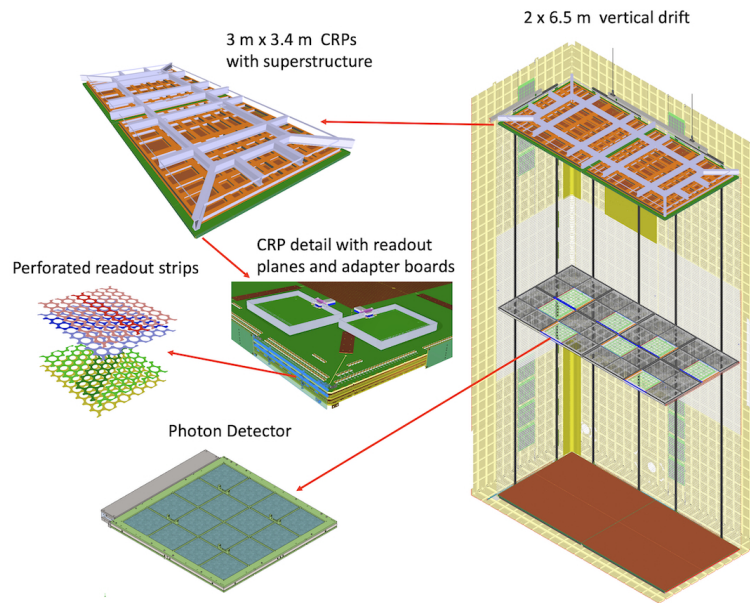
Figure 8: Schematic of the vertical drift FD2 concept with PCB-based charge readout. Corrugations on cryostat wall shown in yellow; PCB-based CRPs (brown, at top and bottom with superstructure in gray for top CRPs); cathode (violet, at mid-height with openings for photon detectors); field cage modules (white) hung vertically around the perimeter (the portions near the anode planes are 70% optically transparent); photon detectors (light green at right), placed in the openings on the cathode and on the cryostat walls, around the perimeter in the vertical regions near the anode planes. Updated from [60].
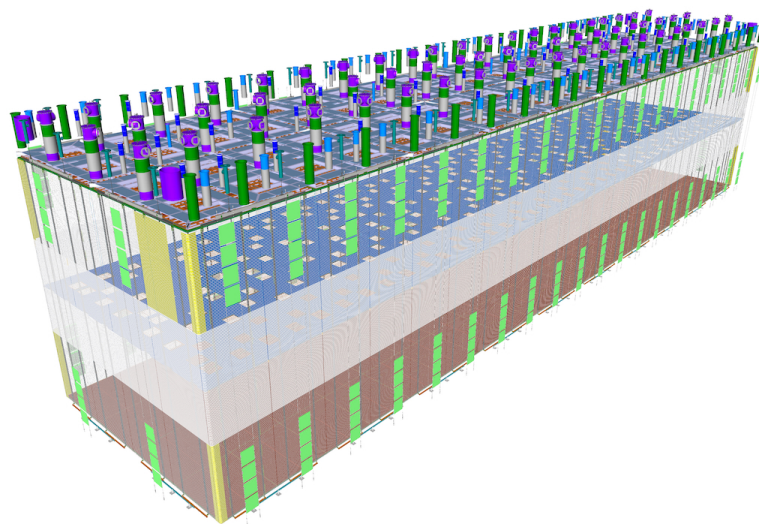
Figure 9: Perspective view of the vertical drift FD2 detector. From [60].

- maximizing the active volume[1];

- high modularity of detector components;

- simplified anode structure based on standard industrial techniques;

- simplified cold testing of instrumented anode modules in modest size cryogenic vessels;

- field cage structure independent of the other detector components;

- extended drift distance;

- reduction of dead material in the active volume;

- allowance for improved light detection coverage;

- simplified and faster installation and quality assurance (QA)/quality control (QC) procedures; and

- cost-effectiveness.

3.2.1 Charge readout planes (anodes)

The baseline design FD2 anodes, illustrated in Figure 10, provide three-view charge readout via two induction planes and one collection plane. The anodes are fabricated from two double-sided, perforated, 3.2 mm thick printed circuit boards (PCBs), that are connected mechanically, with their perforations aligned, to form charge-readout units (CRUs). A pair of CRUs is attached to a composite frame to form a CRP; the frame provides mechanical support and planarity. The holes allow the electrons to pass through to reach the collection strips. Each anode plane consists of 80 CRPs in the same layout. The CRPs in the top drift volume, operating completely immersed in the LAr, are suspended from the cryostat roof using a set of superstructures, and the bottom CRPs are supported by posts positioned on the cryostat floor. The superstructures hold either two or six CRPs, and allow adjustment, via an externally accessible suspension system, to compensate for possible deformations in the cryostat roof geometry.

The FD2 top and bottom drift volumes implement different charge readout (CRO) electronics. The top anode is read out via the top drift electronics (), based on the design used in ProtoDUNE-DP, that comprises both cold and warm components housed in signal feedthrough chimneys (SFT chimneys). These chimneys penetrate the cryostat roof, allowing the components to be fully accessible for repair or upgrade. The bottom detector electronics (), on the other hand, implements the same cold electronics (CE) used in the horizontal drift FD1, which features local amplification and digitization on the CRP in the LAr, thereby maximizing the signal-to-noise.

---

[1]For reference, the FD2 detector model yields an active volume of 10,586 m^3, a 5.6% increase over the estimated FD1 active volume of 10,021 m^3.
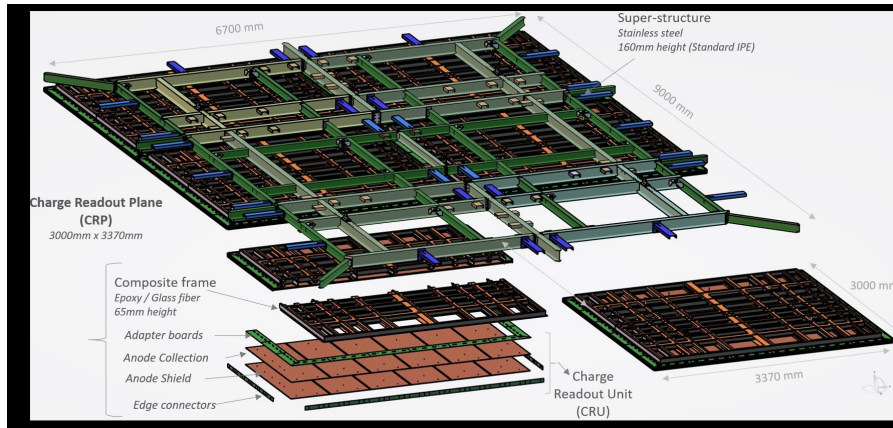
Figure 10: A top superstructure (green structure on top) that holds a set of six CRPs, and below it an exploded view of a CRP showing its components: the PCBs (brown), adapter boards (green) and edge connectors that together form a CRU, and composite frame (black and orange). From [60].

3.2.2 High-voltage system

The FD2 has a horizontal cathode plane placed at detector mid-height, held at a negative voltage, and horizontal s (biased at near-ground potentials) at the top and bottom of the detector, which together provide a nominal uniform E field of 450 V/cm. The main high voltage system (HVS) components are illustrated in Figure 11.

The HVS is divided into two systems: (1) supply and delivery, and (2) distribution. The supply and delivery system consists of a negative high voltage power supply (), high voltage (HV) cables with integrated resistors to form a low-pass filter network, a HV feedthrough (), and a 6 m long extender inside the cryostat to deliver −294 kV to the cathode. The distribution system consists of the cathode plane, the field cage, and the field cage termination supplies. The cathode plane is an array of 80 cathode modules, each with the same footprint as a CRP, formed by highly resistive top and bottom panels mounted on fiber-reinforced plastic () frames. The modular field cage consists of horizontal extruded aluminum electrode profiles stacked vertically at a 6 cm pitch. A resistive chain for voltage division between the profiles provides the voltage gradient between the cathode and the top-most and bottom-most field-shaping profiles.

In addition to the primary function of providing uniform E fields in the two drift volumes, both the cathode and the field cage designs are tailored to accommodate PDS modules (Section 3.2.3) since it is not possible to place them behind the anode plane, as in the FD1-HD design. Each cathode module is designed to hold four double-sided X-ARAPUCA PDS modules that are exposed to the top and bottom drift volumes through highly transparent wire mesh windows. Along the walls, the field cage is designed with narrow (15 mm width) profiles in the region within 4 m of the anode plane to provide 70% optical transparency to single-sided PDS modules mounted on the cryostat membrane walls behind them, and conventional (46 mm width) profiles within 2.5 m of the cathode plane.
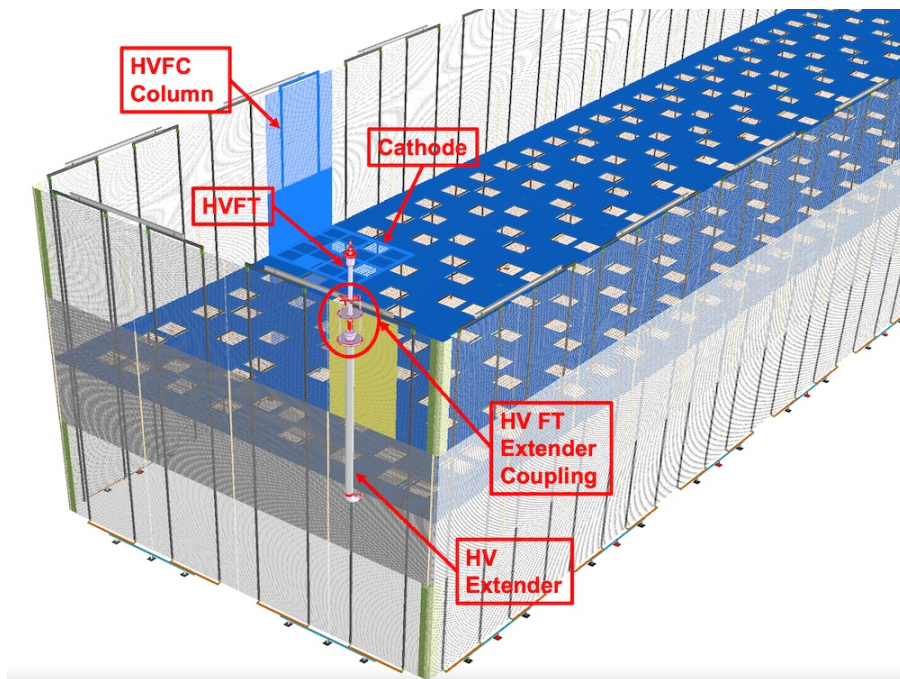
Figure 11: A bird's-eye view of the field cage, with one full-height field cage column (highlighted in cyan) that extends the entire height, the HV feedthrough and extender (in the foreground), and the cathode (with one cathode module highlighted in cyan and modules installed on cathode). From [60].

3.2.3 Photon detection system

The FD2 module will implement X-ARAPUCA [63, 64] PDS modules. Functionally, an X-ARAPUCA module is a light trap that captures wavelength-shifted photons inside boxes with highly reflective internal surfaces until they are eventually detected by SiPMs. An X-ARAPUCA module has a light collecting area of approximately $600 \times 600\,\mathrm{mm}^2$ and a light collection window on either one face (for wall-mount modules) or on two faces (for cathode-mount modules). The wavelength-shifted photons are converted to electrical signals by 160 SiPMs distributed evenly around the perimeter of the photon detector (PD) module. Groups of SiPMs are electrically connected to form just two output signals, each corresponding to the sum of the response of 80 SiPMs.

Since their primary components are almost identical to those of FD1-HD, only modest R&D was required for the FD2 PDS modules. The primary differences were to optimize the module geometry and the proximity of the SiPMs to the wavelength-shifting (WLS) plates. Both of these are more favorable in FD2, leading to more efficient light collection onto the SiPMs. As discussed in Section 3.2.2, the design has the PDs mounted on the four cryostat membrane walls and on the cathode structure, facing both top and bottom drift volumes. This configuration produces approximately uniform light measurement across the entire TPC active volume.

Cathode-mount PDs are electrically referenced to the cathode voltage, avoiding any direct path to ground. While membrane-mount PDs adopt the same copper-based sensor biasing and readout techniques as in FD1-HD, cathode-mount PDs required new solutions to meet the challenging constraint imposed by HVS operation. The cathode-mount PDS are powered using non-conductive power-over-fiber (PoF) technology [65], and the output signals are transmitted through non-conductive optical fibers, signal-over-fiber (SoF), thus providing voltage isolation in both signal reception and transmission.

3.3 Optimized charge and photon readouts for Phase II vertical drift FD modules

Several variations on the vertical drift design are under consideration to improve the performance and/or reduce the cost. Potential improvements can be broadly grouped into two classes, the charge readout and the photon readout systems.

Optimizations of the charge readout system include options to improve the production processes and reduce the cost of the CRPs, possible optimizations of strip pitch and length, and channel count (Section 3.3.2). Other options are to replace the strip-based CRP with a pixel based CRP (Section 3.3.3) or with an optical readout based on electroluminescence (Section 3.3.4).

The leading criteria for selecting an optimized technology for a Phase II photon readout system are performance enhancement at low incremental costs, and the ability to leverage minimum-risk development of solutions already demonstrated and adopted for Phase I. One of the most attractive options is the proposed concept (Section 3.3.1), in which PDs are integrated into the field cage. The APEX concept makes use of the PoF and SoF technologies developed for FD2 and opens up the opportunity to greatly extend the optical coverage. Another optimization

under consideration is the addition of photon detection to a pixel-based CRP (Section 3.3.5).

3.3.1 Optimized photon readout with APEX

The APEX concept (Aluminum profiles with embedded X-ARAPUCA) integrates a large-area photon detection system into the detector module's field cage. APEX is a simplified, lightweight, and low(er)-cost photodetector solution for optimizing photon readout that increases the active optical coverage of the LAr target volume. This solution is derived from the well-established X-ARAPUCA technology with SiPM photosensors developed for FD2. Concrete examples of physics topics enabled by an improved light detection system are given in Sec. 2.2, in the context of the neutrino astrophysics program of DUNE.
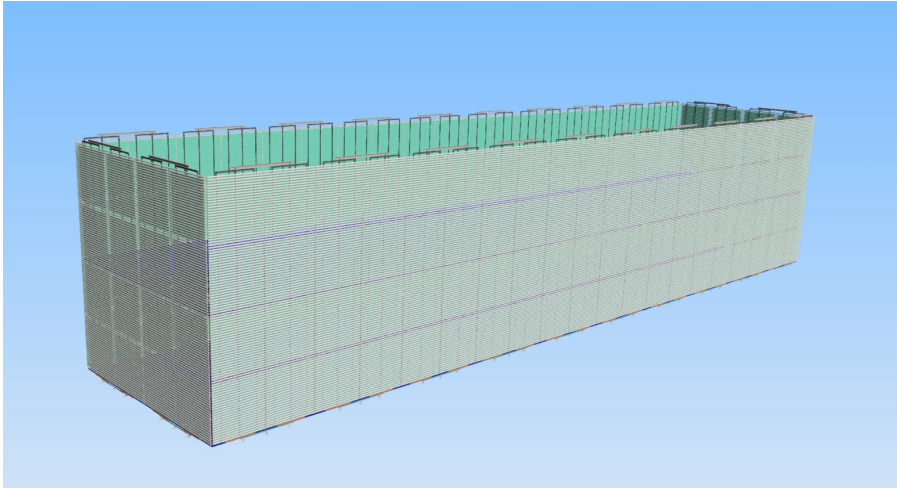
Figure 12: A bird's-eye view of the field cage with integrated large-area photon detection system, APEX. The field cage structure is constructed of modules vertically stacked in groups of four hanging around the LAr drift volume perimeter from the top.

The field cage covers the four vertical sides of the VD LArTPC active volume between the top anode and bottom anode planes, and thus offers the largest available surface for extended optical coverage, i.e., APEX can provide up to $\sim 60\%$ coverage of the surface enclosing the LArTPC active volume if the field cage walls are fully instrumented, as shown in Fig. 12. In the APEX concept, no PD modules are installed on the cathode. The PD readout electronics would need to be referenced to the (high) voltage level of the field cage electrode profile on which the PD module is installed, and therefore would require electrical isolation. Power and signal transmission can be established via non-conductive optical fibers by using the PoF and SoF technologies developed for the FD2 photon detectors that are integrated into that FD module's HV cathode plane. These technologies are described in Section 3.2.3. They have been demonstrated to work reliably for electrical isolation with noise immunity and long-term stability in LAr.

APEX keeps the same field cage structure as designed for FD2 (see Figure 11), which includes 24 field cage supermodules, each made up of eight $3.0 \times 3.2\,\mathrm{m^2}$ field cage modules, for

Figure 13: An APEX panel. Top left: one PD module installed on field cage profiles. Bottom left: a PD module equipped with a SiPM strip at the center. Center: front view of an APEX panel showing the 6×6 array of PD modules mounted on an field cage module. Right: a back view of the field cage module showing its aluminum profile structure.

a total of 192 modules. A field cage module consists of horizontal extruded aluminum C-shaped electrode profiles (3 m long and 6 cm wide) stacked vertically at a 6 cm pitch and mounted on vertical FR4 I-beams. An APEX panel, illustrated in Figure 13, is a standard vertical drift field cage module instrumented with a 6×6 array of thin, large-area ($\sim 50 \times 50 \, \text{cm}^2$) X-ARAPUCA-type PD modules installed onto the field cage structure and fully covering it, as shown in Figure 13. Hydrodynamic simulations are under development to understand the potential impact of APEX panels on the LAr recirculation.

Six PD modules constitute a horizontal row of the APEX panel. Each PD module vertically spans about nine field cage profiles and is mechanically fastened and electrically referenced to the profile at its mid-height (the fifth of nine). The cavity of this profile houses and provides Faraday shielding for the cold electronics readout boards for all six of the PD modules in that row of the array, providing signal conditioning and digitization in cold. Several PoF receivers and an SoF transmitter (driver and laser diode) at the center of the $\sim$3 m long profile receive power and transmit signal, respectively, for the PD modules in the row via optical fibers. The signals from the six PD modules are multiplexed and transmitted over a single optical fiber to the (warm) receivers and data acquisition (DAQ), as schematically represented in the block diagram of Figure 14. The fibers are routed through the penetration at the top of the cryostat using the central vertical I-beam of the field cage structure as conduit. Each row of six PD modules in an APEX panel thus forms an electrically isolated system.

Figure 14: APEX cold readout concept: a row of six PD modules (three of the six are not shown in order to display the readout elements) in an APEX panel forming an electrically isolated single readout system.

The PD module, the basic unit of the APEX array, is a simplified version of the light trap X-ARAPUCA concept used in the FD1 and FD2 PDS, designed to be a lightweight ($\sim$1.8 kg), compact object suitable for efficient mass production. Two WLS stages, #1 and #2 – with a dichroic filter (DF) between them – convert, transmit, and trap incident LAr scintillation light under the dichroic filter layer. These components are contained in solid PMMA (transparent acrylic) slabs that are 6 mm thick, with a surface area of $\sim 50 \times 50 \, \text{cm}^2$, illustrated in Figure 13, bottom left. The DF layer is deposited directly on the front plane of the acrylic substrate, and

the WLS #1 coating on top of the DF. Chromophore molecules embedded in the substrate PMMA (WLS #2) matrix shift transmitted light to a wavelength above the DF cutoff. Light trapping is optimized by ultra-high reflectivity non-metallic thin film lamination (e.g., Vikuiti ESR) of the acrylic slab edges and backplane. An array of SiPMs mounted on a flex PCB are optically bonded to the acrylic surface, as shown in Figure 13, bottom left. Photons trapped by reflection in the slab are eventually absorbed by the photosensors, producing electronic signals. We estimate that 80 large-area SiPMs per module, with high photon detection efficiency (), ganged together into one readout channel, will be sufficient to reach an overall detector efficiency of $\epsilon_D \simeq 2\%$.

Assembly of APEX panels is expected to be simple. To assemble one, aluminum field cage profiles are first assembled to form a field cage module, electronics boards are positioned in the profiles, and PD modules are connected to the boards then fastened to the profiles to complete the APEX panel. An APEX assembly can be built out of bulk materials (aluminum profiles and acrylic plates) with low-radioactive content. For this reason, even an extended PDS coverage compared to Phase I modules is not expected to be a dominant contributor to the internal background budget discussed in Sec. 3.6.
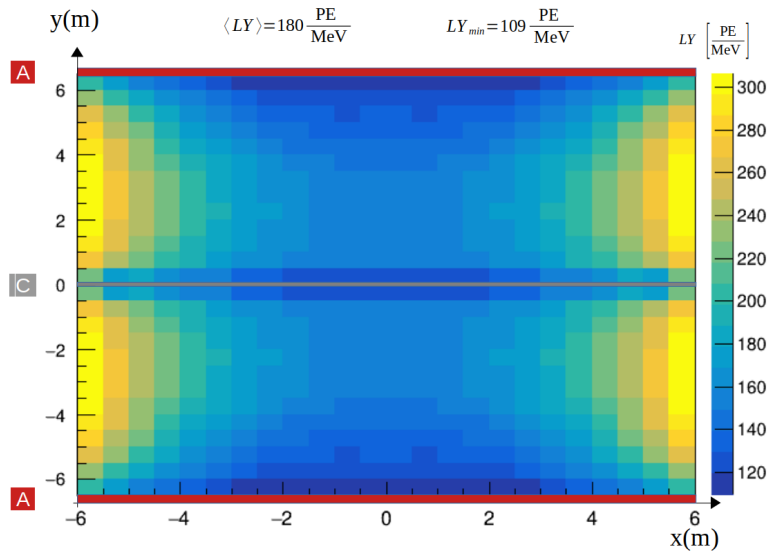
Figure 15: Map showing the expected in the central (x, y) transverse plane at $z = 0$ for the field cage-extended coverage APEX photon detection system. Dimmer regions are present near the anode planes (with no PDs on them) and at mid-height (near the non-instrumented cathode plane).

A simulation was performed for a Phase II FD module with APEX, assuming 55% optical coverage of the LAr volume. The light yield $LY(x, y, z)$ of the system was evaluated, i.e., the number of photoelectrons (PEs) collected per unit of deposited energy anywhere in the LAr volume, assuming 2% detection efficiency of the X-ARAPUCA module and standard LAr scintillation light emission and propagation parameters. The simulation resulted in an average value

$\langle LY \rangle = 180$ PE/MeV across the detector volume, with a minimum of $LY_{\min} = 109$ PE/MeV near the anode planes, thanks to the extended optical coverage of the APEX system. Such a light yield would be about a factor of 5 higher than the FD2 one, where simulations indicate an average light yield of 39 PE/MeV and a minimum light yield of 16 PE/MeV [60]. Figure 15 shows the light yield map in the transverse plane at the center of the FD module long axis. APEX-specific studies on light-only and charge+light calorimetric performance, impact of non-uniform light collection, and achievable PDS thresholds in the presence of background flashes, are in progress.

A series of prototypes are planned to fully develop the APEX concept. A first round of prototyping, carried out at CERN, has studied the impact on the drift field uniformity of placing insulating material between field cage electrodes. The (expected) observation of a slow buildup of static charge on the surface of the insulating material may, counter-intuitively, allow reduction of the number of field cage electrodes, with a larger pitch. The current (2024) focus is on a second (ton-scale) TPC prototype at CERN that will be instrumented with up to eight full-size PD modules, primarily for mechanical and cryogenic tests. Additionally, a PD module prototype with a full electronic chain, including PoF and SoF systems, will be constructed and tested in parallel before being integrated into this prototype. A larger-sized APEX demonstrator in a several cubic meter LAr cryostat, with $\mathcal{O}(100)$ SoF and PoF in/out fibers, will be a third-stage prototyping goal in 2024-2025, likely at Fermilab. Finally, a full-sized APEX PD-instrumented field cage will be deployed in the VD cryostat at CERN, along with the proposed optical readout (Section 3.3.4).

3.3.2 Strip-based charge readout

The PCB-based vertical drift anodes, called CRPs, are made up of two stacked PCBs, providing three projective views. The PCB face directly opposite the cathode has a copper guard plane to absorb any unexpected discharges. The reverse side of this PCB is etched with strips that form the first induction plane. The other PCB has strips on the side facing the inner PCB forming the second induction plane, and has the collection plane strips on its reverse side [60]. The PCBs are supported by composite frames and mechanically connected using spacers. CRPs have been successfully demonstrated in the 50 L test stand and at full scale in the vertical drift cold box. They have been installed in ProtoDUNE-VD in the NP02 cryostat at CERN and will be deployed in the FD2 cryostat at SURF (see Figure 10).

This system has already been optimized for deployment in FD2, and as such forms a reference solution also for FD3. Additional optimizations should be explored for FD3 to reduce cost or to improve performance further. There are various ways in which the strip-based charge readout might be re-optimized that would impact the strip pitch, length, and orientation. A more concrete optimization plan will be developed after assessing ProtoDUNE-VD performance in 2025.

Additional considerations to be explored include the CRP fabrication techniques, including faster production of the PCB itself and simpler quality control. Some of these ideas have been tested in the 50 L test stand at CERN, particularly techniques to reduce PCB hole misalignments.

In addition to the CRP, the readout electronics need some re-optimization. Depending on the timescale for construction of FD3, some of the existing electronics production lines may no longer be available. This may require re-design of components associated with readout of the top and/or bottom CRPs. For example, a potential optimization of the FD2 BDE includes porting the , a custom pre-amplifier and shaping , from the 180 nm to the 65 nm production process[2] to mitigate the risk of losing access to the 180 nm process. The two other BDE custom ASICs, and , are already using the 65 nm process. Other potential optimizations for the FD2 BDE design include reducing the cable length for signal and power (it is 27 m for the current FD2 design), simplifying detector installation.

3.3.3 Pixel-based charge readout

A pixel-based readout would replace the multi-layer strip-based readout with a single-layer grid of charge-sensitive pixels at mm-scale granularity. Instrumenting each pixel with a dedicated electronics channel would achieve a LArTPC with true and unambiguous 3D readout, where information on the third spatial dimension is provided by the LArTPC drift time. This is advantageous compared to conventional wire-based two-dimensional readout, especially for higher-multiplicity interactions of $O(\text{GeV})$ neutrinos. In interactions with several charged particles in the final state, it is possible for tracks to overlap in one 2D projection, making it more difficult to reconstruct. Similarly, straight-line tracks in strip-based readout have pathological angles where the track is recorded entirely along a single strip. Given channel densities of $\mathcal{O}(10^5)$ pixels per m^2 of anode, pixel readout would require operation at $\mathcal{O}(100)$ μW power consumption per channel, including amplification, digitization and multiplexing. This is necessary in order to avoid excessive heating of the LArTPC detector, operating near LAr boiling point. Significant progress has been made in recent years in the development of pixel readout for LArTPCs, overcoming issues with excessive waste heat, as well as demonstrating cryo-compatibility, $\mathcal{O}(10^4)$ digital multiplexing, and cost-effective, scalable production. Two options for readout are discussed below, and .

LArPix Readout

LArPix [66] is a complete pixel readout system for LArTPCs, consisting of 6400-channel pixel anode tiles, cryogenic-compatible data and power cabling, and a multi-tile digital controller with an integrated operating system. It has been developed as the baseline technology of Phase I ND-LAr. The system relies on the LArPix ASIC, a 64-channel detector system-on-a-chip that includes analog amplification, self-triggering, digitization, digital multiplexing, and a configuration controller.

The LArPix-v1 ASIC demonstrated that waste heat could be controlled through a custom low-power amplifier and channel self-triggering, where the digitization and digital readout are dormant until a signal is detected on the pixel. The LArPix-v2 ASIC incorporated a variety of improvements to facilitate large-scale production of pixel anodes, including Hydra-IO, a

---

[2]The 180 nm and 65 nm processes are advanced lithographic techniques used in semiconductor fabrication; the dimension refers to feature size.

novel programmable chip-to-chip data routing technique to improve system reliability in the inaccessible cryogenic detector environment.

The current 32×32 cm^2 LArPix pixel tile (Figure 16) has 6400 charge-sensitive pixels at 3.8 mm pitch and can be configured and read out via a single set of differential digital input and output wires. The design leverages standard commercial techniques for PCB production to realize a LArTPC anode, achieving 800 e$^-$ equivalent noise charge per channel on the sensitive TPC-facing side of the tile, while powering and communicating with 100 LArPix ASICs on the back side. The power consumption achieved by the current LArPix tile is 14 W/m^2, ensuring that the heat flux from the anode is lower than the one from the cryostat walls.

Data acquisition is controlled by the Pixel Array Controller and Network (PACMAN) card, responsible for delivering power and communication to the tiles. A single compact controller is currently capable of driving $\mathcal{O}(10)$ pixel tiles (e.g., $\mathcal{O}(10^5)$ pixels). It includes a CPU with integrated operating system and programmable logic similar to a field programmable gate array (FPGA). The controller is designed to mount on the room-temperature side of a LArTPC cryostat feedthrough, and incorporates power filtering and ground isolation to ensure the integrity of the low-noise environment within the detector.
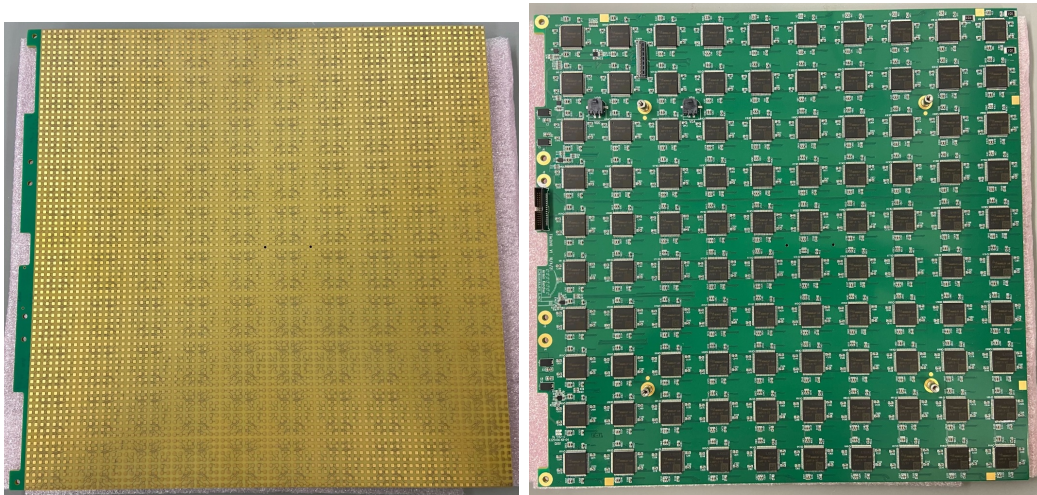
Figure 16: Left: Prototype LArPix-v2 anode tile 32 cm in length by 32 cm in height, with 6400 gold-plated charge sensitive pixel pads at 3.8 mm pitch driven by (right) 100 LArPix-v2 ASICs.

Approximately 80 LArPix-v2 pixel tiles have been produced as part of the current prototyping program for the DUNE ND. Sets of 16 pixel tiles have been used to instrument each of the four ton-scale LArTPC modules of the 2×2 Demonstrator (Figure 17), a prototype of the modular LArTPC design planned for the ND. Each module has been operated at the University of Bern, and has been used to image over 100 million cosmic ray events.

The LArPix-v2 development program has achieved its goal of a scalable design. All components are produced via commercial vendors using traditional electronics production techniques, and are ready for integrated testing; no additional assembly is required. LArPix-v2 system production costs, including all cabling, controllers, and power supplies, are approximately $10k

per square meter.

Operation of prototype LArPix anodes, in either vertical or horizontal orientations, show that natural convection provides sufficient heat dissipation to mitigate argon phase transition (bubble formation or boiling). In particular, the 2x2 Demonstrator [67], a prototype of the DUNE ND, is constructed of multiple fiberglass boxes with a very low perforation, approximately 1% of the surface, and rather limited spaces for convective heat dissipation, yet it shows no issues with thermal management and has achieved purity in excess of 2 ms. Future work includes a demonstration of LArPix anode heat dissipation in a configuration similar to the FD2 design.

Assuming completion of the development program of LArPix for the DUNE ND, LArPix would already meet most of the requirements for deployment in a future FD module. The development and integration of a high-speed, $\mathcal{O}(1)$ GHz, 16-to-1 digital multiplexer would significantly reduce the number of cables and feedthroughs, making deployment in a FD much more feasible. Tests of a large-scale LArPix prototype in the ProtoDUNE-VD system at the CERN Neutrino Platform are important to validate the integration and interfaces with the other aspects of the vertical drift design.

Q-Pix Readout

Q-Pix is a novel pixel-based technology for low-threshold, high-granularity readout that is expected to improve reconstruction relative to projective-based readout, at a much reduced data throughput. It is ideally suited to the low data rate readout environment of the DUNE FD modules. The basic concepts of the Q-Pix circuit [68] are shown in Figure 18 (A). The input pixel is envisioned to be a simple circular trace connected to the Q-Pix circuit via a PCB. The circuit begins with the "Charge-Integrate/Reset" (CIR) circuit. This charge-sensitive amplifier continuously integrates incoming signals on a feedback capacitor until a threshold on a Schmitt trigger (regenerative comparator) is met. When this threshold is met, the Schmitt trigger starts a rapid "reset" enabled by a Metal–oxide–semiconductor field-effect transistor (MOSFET) switch, which drains the feedback capacitor and returns the circuit to a stable baseline, at which point the cycle is free to begin again. To mitigate any potential charge loss, an alternative design known as the "replenishment" scheme has also been evaluated. In contrast to the reset architecture, the MOSFET now functions as a controlled current source such that when the Schmitt trigger undergoes a transition, the MOSFET replenishes a charge of $\Delta Q = I \cdot \Delta t$, where Δt is the reset pulse width or discharge time.

Both the "reset" and "replenishment" schemes capture and store the present time of a local clock within one ASIC. This changes the basic quantum of information for each pixel from the traditional "charge per unit of time" to the difference between one clock capture and the next sequential capture, the Reset Time Difference (RTD). This new unit of information measures the time to integrate a pre-defined charge. Physics signals will produce a sequence of short, $\mathcal{O}(\mu s)$, RTDs. On the other hand, in the absence of a signal, the quiescent input current from ^{39}Ar and other radiogenic or cosmogenic backgrounds would be small, producing long, $\mathcal{O}(s)$, RTDs. Signal waveforms can be reconstructed from RTDs by exploiting the fact that the average input current and the RTD are inversely correlated.
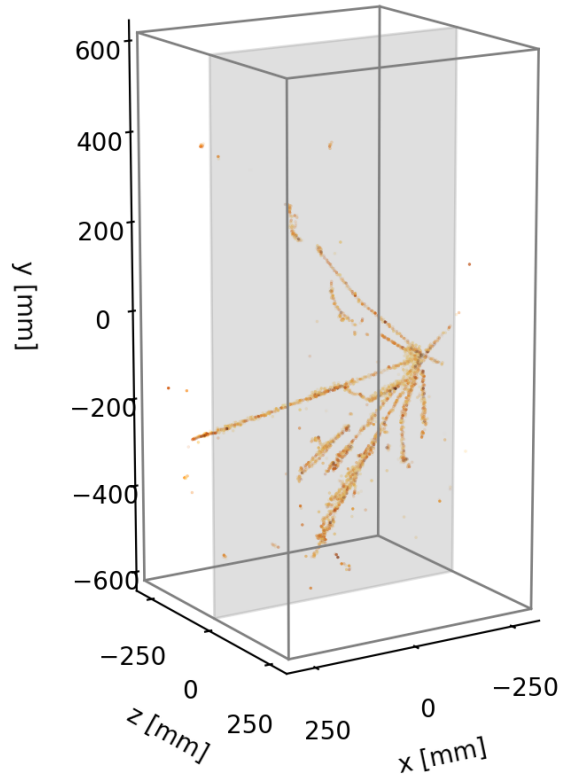
Figure 17: Left: A photograph of one of the four ton-scale LArTPC modules for the 2x2 Demonstrator, a prototype of the DUNE ND. Right: an example cosmic ray imaged in true 3D using a 102,400-channel LArPix-v2 system in this module (right).

Q-Pix has shown that this architecture can enhance the physics capabilities of a large-scale LArTPC through its ability to provide full 3D information of the events, as opposed to the three 2D projections provided by FD1/FD2 readout. The first of these demonstrations shows the improved reconstruction enabled by a pixel based detector when compared to a projective-based readout for DUNE multi-GeV neutrino interactions [70]. This analysis showed enhanced efficiency and purity across all neutrino interaction types analyzed and the ability to reconstruct the topology and content of the hadronic system (including number of final state protons, charged, and neutral pions). Moreover, through an analysis of supernova neutrino interactions and a simulation of the Q-Pix architecture, it was shown that Q-Pix can significantly enhance the low-energy neutrino capabilities for kiloton-scale LArTPCs. Specifically, Q-Pix: i) enhances the efficiency of reconstructing low-energy supernova neutrino events over the nominal wire based readout, ii) allows for a high-purity and high-efficiency identification of supernova neutrino candidates, and iii) affords these enhancements at data rates 10^6 times less for the same energy threshold [71].
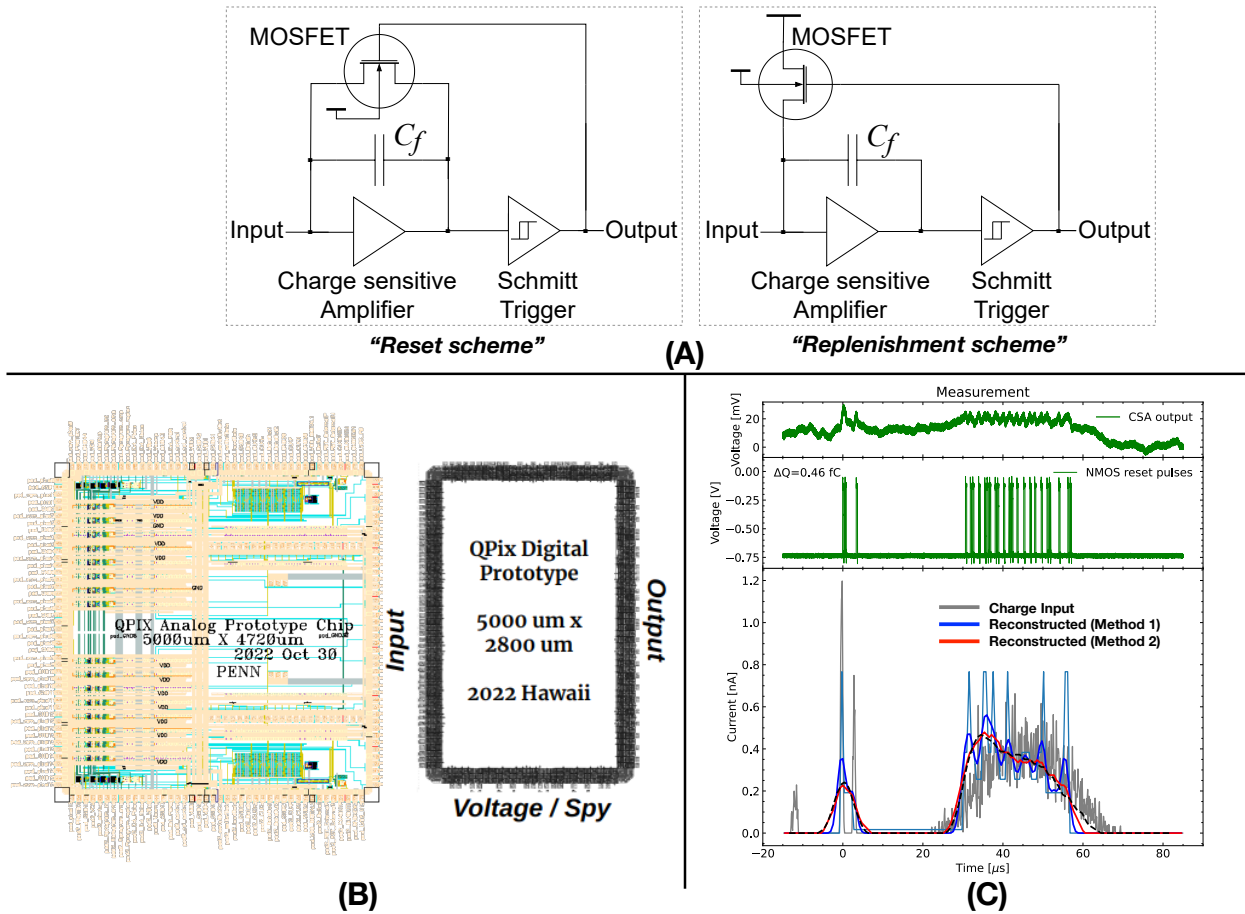
Figure 18: A) Schematic of the basic concepts of the Q-Pix circuits for the reset and replenishment schemes. B) Left: Schematic of the 16-channel analog front-end and Right: schematic of the 16-channel digital design. C) Current waveform reconstructed using a discrete-component implementation of the Q-Pix replenishment scheme at a charge threshold of 0.46 fC ($\sim 2875e^-$) and reconstructed using different digital filtering based on analysis. Images A and C are adapted from [69].

A number of prototypes are currently under construction and evaluation to demonstrate the Q-Pix readout architecture. These include designs in both 180 nm and 130 nm, evaluation of the architecture using discrete commercial off-the-shelf (COTS) components, as well as extensive digital prototyping using FPGAs. The 180 nm design is shown schematically in Figure 18 (B). It consists of a 16 channel analog chip implemented with the replenishment architecture, and a 16 channel digital chip. On the other hand, Figure 18 (C) shows the implementation of the replenishment architecture for the Q-Pix readout using COTS discrete components. This prototype was able to demonstrate the fidelity of reconstructing input from an arbitrary waveform generator with a replenishment threshold of 0.46 fC with replenishment pulse widths $\sim 300 - 600$ ns and linear responses to replenishment up to 2 MHz rates. This demonstration provides confidence that the architecture proposed will be capable of meeting the performance needs of future large scale LArTPCs. The consortium of universities and labs working on this project expect both small and large scale demonstrator ($\mathcal{O}(1000 - 100,000)$ pixel) LArTPCs in the coming next few years.

3.3.4 Optical-based charge readout

The optical-based readout shares the same physics benefit as the pixel-based charge readout solutions (Sec. 3.3.3) in providing a native 3D readout. This technology has also demonstrated the best spatial resolution of any LArTPC readout option so far, with $\simeq 1.1$ mm per pixel [72]. The data-driven readout with native zero suppression yields a very efficient raw data storage, of relevance for SNB physics. The overall optical gain and the low-noise readout environment enable low-threshold ($\simeq 500$ e$^-$ per pixel) operation, supporting DUNE's MeV-scale neutrino astrophysics program. From the technical point of view, the (off-cryostat) optical readout also benefits from simplicity of access, greatly simplifying maintenance and upgrade operations. Finally, depending on the granularity versus cost trade-off chosen, significant cost savings compared to other readout technologies may also be present.

The optical charge readout with fast cameras was developed within the ARIADNE program and represents a cost-effective and powerful alternative approach to the existing charge readout methodology. As first demonstrated in the one-ton dual-phase ARIADNE detector, the secondary scintillation (S2) light produced in Thick GEM (THGEM) holes can be captured by fast Timepix3 (TPX3) cameras to reconstruct the primary ionization track in 3D.

The operation principle of a dual-phase optical TPC readout with a TPX3 system is shown in Figure 19a. When a charged particle enters the LAr volume, it causes prompt scintillation light (S1) and ionization. The free ionization electrons are drifted in a uniform electric field to the surface of the liquid. A higher field induced between an extraction grid and the bottom electrode of the THGEM extracts the electrons to the gas phase. Once in gas, the electrons are accelerated within the 500 μm holes of the THGEM at a field set between 22 and 31 kV/cm. As well as charge amplification, secondary scintillation (S2) light is produced. The light is shifted with a tetra-phenyl butadiene (TPB) coated sheet to 430 nm and then detected by cameras mounted on optical viewports above the THGEM plane.

Originally, the optical readout was tested with EMCCD cameras within the one-ton ARIADNE detector at the T9 charged-particle beamline at CERN [72], and later was upgraded
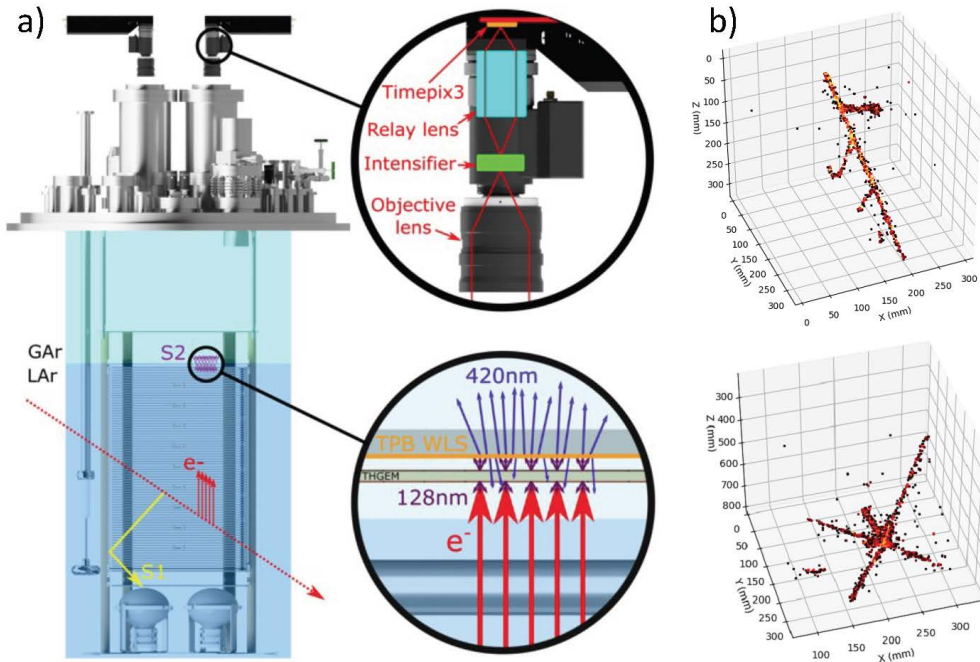
Figure 19: (a) Detection principle of dual-phase optical TPC readout with TPX3 camera, first demonstrated in the one-ton ARIADNE detector. (b) LAr interactions from cosmic-ray muons. Figures taken from [73].

with fast TPX3. The TPX3 camera assembly boosts the S2 light signal and simultaneously measures Time over Threshold (ToT) and Time of Arrival (ToA) information with 10-bit resolution. ToT allows accurate calorimetry and ToA gives accurate timing (1.6 ns resolution). The TPX3 chip then sends a packet containing information that allows for full 3D reconstruction using a single device. The high readout rate (up to 80 Mhits/s), natively 3D raw data, and low storage due to zero suppression make TPX3 ideal for optical TPC readout.

The TPX3 camera system was first tested in low-pressure CF4 gas within the ARIADNE 40 l TPC prototype [74]; following this demonstration, a TPX3 camera was mounted on ARIADNE and particle tracks from cosmic-ray showers were successfully imaged in 3D for the first time (Figure 19b) [73]. The cameras are shown to be sensitive even to pure electroluminescence light generated at the lower end of the THGEM field; this mitigates difficulties often faced when trying to operate THGEMs at a higher field, where there can be issues with stability. Use of cameras has additional benefits, such as ease of upgrade as they are externally mounted. Thus, they are decoupled from TPC and acoustic noise, and large areas can be covered with one camera, bringing both cost and operational benefits.

To demonstrate this technology further and at a scale relevant to the 10 kt (fiducial) FD modules, a larger-scale test (ARIADNE$^+$) was recently performed [75] at CERN. Four cameras, each imaging a $1 \times 1 \, \text{m}^2$ field of view, were employed. One camera utilized a novel VUV image intensifier, eliminating the need for a wavelength shifter. The test also showcased a light readout plane (LRP) comprising sixteen, $50 \times 50 \, \text{cm}^2$ surface area, glass THGEMs. The novel
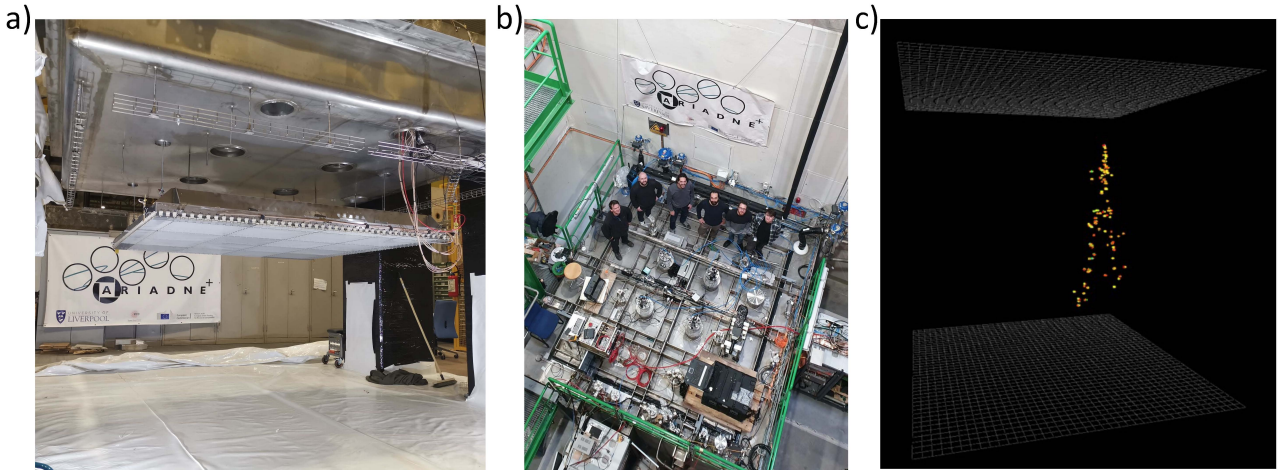
Figure 20: (a) The light readout plane under the cryostat lid; (b) the ARIADNE$^+$ team on top of the cryostat; (c) a recorded image of an interaction in LAr.

manufacturing process for the glass THGEMs allows for mass production at large scale [76]. Stable operation was achieved, and cosmic-ray muon data from both the visible and VUV intensifiers were collected. An image of the detector setup is shown in Figure 20 and results are published in [77].

The TPX3Cam camera and image intensifiers are commercially available, and a proposal to instrument the ProtoDUNE cryostat with optical readout is underway, with testing anticipated to take place in 2025/2026. Further R&D into custom optics and characterization of the next generation Timepix4 (TPX4) cameras, which are anticipated to become commercially available by the end of 2025, can offer further benefits. Another promising ongoing R&D effort is a TPX4 camera with an integrated image intensifier [78]. One of these devices will be tested in the near future within the ARIADNE one-ton detector. Given the current progress of the TPX4 camera system, partial TPX4 instrumentation in NP02 is anticipated.

3.3.5 Integrated charge and light readout on anode

DUNE is also pursuing the integration of both light and charge detection modes on the anode into a single detector element. If such a device could be made sensitive both to VUV photons at reasonable quantum efficiency and to ionization electrons, this would transform the way noble element detectors collect and process both the charge and light signals. A detection element of this kind would offer: i) intrinsic fine-grained information for both charge and light, providing accurate matching between charge and light information; ii) a significant enhancement in the amount of light collected near the anode and much improved uniformity of response, through increased surface area coverage; and iii) simplification in the design and operation of noble element detectors. The technologies under investigation are described in this section, Solar neutrinos in Liquid Argon (SoLAr), , and Q-Pix Light Imaging in Liquid Argon (Q-Pix-LILAr).

SoLAr The SoLAr technology [79] is based on the concept of a monolithic, light-charge, pixel-based readout to achieve a low energy threshold with excellent energy resolution ($\approx 7\%$ at few-MeV neutrino energies [31]) and background rejection through pulse-shape discrimination.

The SoLAr readout unit (SRU) under development is a pixel tile based on PCB technology that embeds charge readout pads located at the focal point of the LArTPC field-shaping system to collect drifting charges, and highly efficient VUV SiPMs to collect photons in thousands of microcells operated in Geiger mode. In order to maintain a uniform electric field, novel monolithic VUV SiPM sensors need to be developed with these features that have charge readout pads and highly efficient UV-light sensitive microcells.

In 2020, a joint research program between LAr detector scientists and an industrial partner (Hamamatsu Photonics) delivered a SiPM that reached a record efficiency (15% PDE) for 128 nm light at the argon boiling point (87 K). Nearly at the same time, the first integrated system for multiplexing the SiPM signal was commissioned and operated inside strong electric fields. In 2021 a further development with Hamamatsu Photonics produced a new SiPM with through-silicon vias that will enable the combination of light detection with the charge readout required for SoLAr.
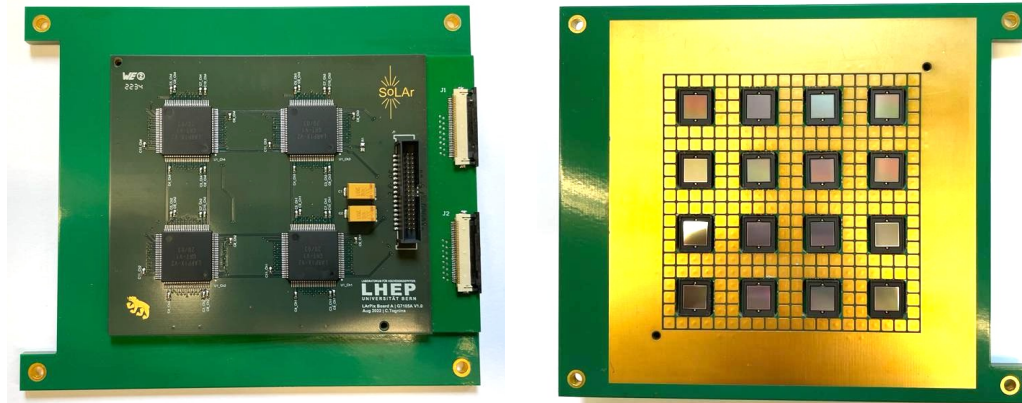
Figure 21: The small-scale SoLAr prototype PCB tested at the University of Bern, front and back sides. The anode consists of a 7×7 cm^2 readout area with 16 VUV SiPMs (the LAr-facing side, at right) and four LArPix-v2a chips on the backplane, at left. The charge pixel pads are 3 mm in size and are placed at a 3.5 mm pitch. The SiPMs have a 6×6 mm^2 sensitive area and are placed at a 17.5 mm pitch.

In the SoLAr preparatory phase (2021-2022), combined light-charge collection was demonstrated using small-size prototypes [80]. The prototypes were operated successfully and have demonstrated that the principle of combining charge and light readout is possible (Figure 21). Simulations accounting for light propagation effects have shown that a 7% energy resolution can be achieved at typical solar neutrino energies (5–20 MeV) and using the scintillation signal only by replacing anode planes with a pixelated readout integrating a light-sensitive area covering $\sim 10\%$ of the surface. This system would enhance the amount of collected light by a factor of five compared with FD1, reducing the frequency at which low-energy background gets incorrectly reconstructed to the (higher) energy region of interest of the signal. The authors

of [31] have studied this remarkable impact of energy resolution in the background budget of a LArTPC using conventional readout in a membrane cryostat.

The combination of shielding and a 7% energy resolution gives access to the 5–10 MeV region, where most of the ^{8}B neutrinos (^{8}B $\rightarrow$ ^{8}Be* + e$^+$ + ν_e) reside, by greatly reducing the dominant background from neutrons and ^{42}K above 5 MeV visible energies. The energy resolution is instrumental for sharpening the 17 MeV cutoff of the ^{8}B neutrino spectrum, which lies just below the "hep" cutoff of 18.8 MeV, and opens a 1.8 MeV window that allows observation of a pure sample of hep neutrinos (^{3}He + p $\rightarrow$ ^{4}He + e$^+$ + ν_e) [81]. Light collection outside the anode is ensured by X-ARAPUCA tiles, for a total coverage of $(8 - 10)$%.

The latter provide the appropriate light yield without resorting to xenon doping, thus preserving the pulse-shape discrimination power of liquid argon. Pulse-shape discrimination is further enhanced with respect to any existing LArTPC by the unique performance of the SRU and the increase of collected light.

Finally, SoLAr will implement neutron shielding embedded directly in the cryostat walls, delivering a novel membrane-based cryogenic system that also suppresses environmental background to the limit where the only residual background is generated inside the LArTPC. This will provide a radiopure environment and reduce external neutron background in the 1-4 MeV region by three orders of magnitude.

LightPix   A variant of the LArPix ASIC has been designed for scalable readout of very large arrays of SiPMs. Called LightPix, this ASIC reuses much of the LArPix system design to provide a system that can read out $>10^5$ individual SiPMs in a cryogenic environment at costs far below \$1 per channel. LightPix may be useful for instrumenting a future far detector PDS with higher quantities of SiPMs than the FD1/FD2 PDS design. This could be used as a readout unit in conjunction with an anode-based light pixel solution, e.g., SoLAr.

LightPix prototyping in combination with VUV-sensitive SiPMs is underway. The first-generation 64-channel LightPix-v1 ASIC includes a custom low-power time-to-digital converter (TDC) with sub-ns resolution to enable precise measurement of photon arrival times. It also implements programmable digital coincidence logic for the suppression of dark counts, particularly useful for room-temperature detector applications. The LightPix-v1 ASIC was used to demonstrate particle detection in two small-scale prototype VUV-scintillation detectors: a 16-channel system integrated into a LArPix pixel tile LArTPC detector at LBNL, and a 300-channel system for readout of a high-pressure gaseous helium detector at UC-Berkeley/LBNL. A second-generation ASIC, LightPix-v2, is in fabrication. Changes include a new front-end amplifier optimized for use with larger (higher-capacitance) SiPMs, as well as a charge-integrator for use in higher-occupancy environments.

Q-Pix-LILAr   The Q-Pix consortium is pursuing a different integrated charge and light readout system on the anode, by coating a charge readout pixel with a type of photo-conductive material that, when struck by a VUV photon, would generate a signal (charge) that could be detected by the same charge readout scheme considered for the ionization charge. The Q-Pix-LILAr concept is shown schematically in Figure 22 (A). Moreover, with the proper choice of

photoconductor, such a device could have a broad photon wavelength response, thus offering detection of the full spectrum of light produced in noble element TPCs.
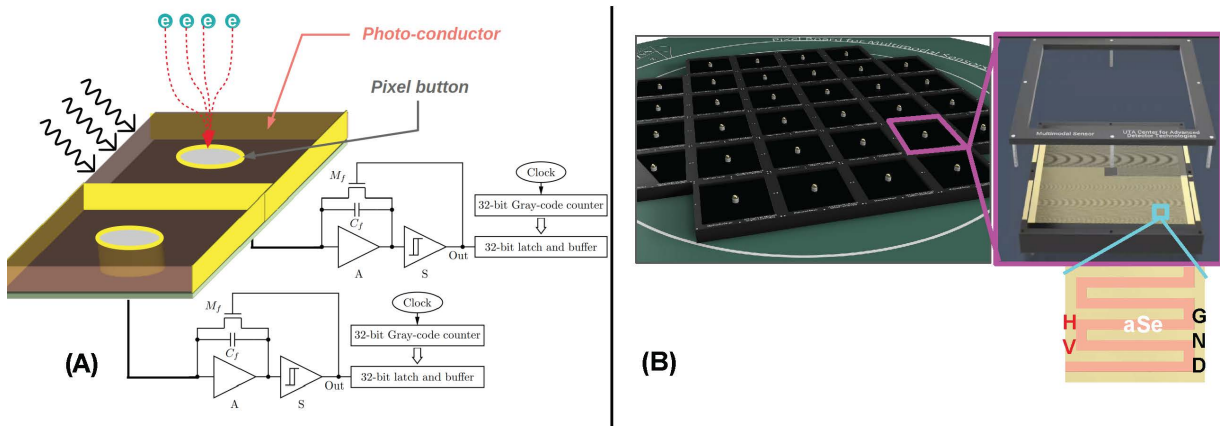
Figure 22: A) Schematic design for the Q-Pix-LILAr integrated charge and light readout, from [82]. B) Example design for a multimodal (charge and light) pixel where interdigitated electrodes (IDE, not shown) are deposited around the central ionization collection pixel. Once the photoconductor creates single electrons from photon conversion, IDEs define a region of high electric field where avalanche multiplication of those single electrons occurs, producing detectable signals.

Three such photo-conductive materials have been explored in recent R&D: Amorphous selenium (aSe), zinc oxide (ZnO), and organic photodiodes (OPDs). Their application in a liquid argon environment is currently under investigation. Initial studies of constructing a multimodal pixel detector have recently focused on utilizing aSe, as the ability to prototype and test it was the simplest. The first study on aSe in cold used commercially manufactured PCBs to demonstrate that these aSe-based interdigitated electrodes (IDE) are sensitive to VUV light at cryogenic temperatures, are cryo-resistant, and are able to maintain argon purity [82]. Designs for a multimodal pixel are shown in Figure 22 (B) where an IDE is deposited around the central ionization collection pixel. This design provides a straightforward way to apply a local electric field to the aSe, to enable charge gain, and to instrument the area between the charge collection pixels.

More recent studies have pushed this capability further to characterize the performance of such a design to a low photon flux ($\mathcal{O}(100)$ photons), at high electric fields ($> 70\,\text{V}/\mu\text{m}$) and at cryogenic temperatures. These results continue to show promise. Further R&D into aSe-based devices, as well as other photoconductors, is anticipated to be an area of active research in the near future.

3.4 Liquid-argon doping

A promising direction for expanding DUNE capabilities in a Phase II FD module is to introduce dopants to the LAr, creating a detector medium other than pure argon. Generically,

these LAr "doping" techniques may be used to modify the detector response in a desirable way or to introduce new target materials of interest into the bulk detector volume. These approaches are analogous to widely-used strategies in e.g., scintillator or solid state detectors, where secondary fluors are sometimes added to scintillators to shift photon wavelengths, or elements like gadolinium or lithium are added to increase neutron or neutrino cross sections, respectively. A key constraint for LAr dopants is that they must not interfere with the operation of the LArTPC by introducing electronegative impurities that non-negligibly degrade the LAr transparency to electrons. Furthermore, as for any large-scale detector with complex physics of signal generation, the relevant microphysics (including radiative and non-radiative molecular energy transfer, electron-ion recombination, and scintillation-light production) must be well understood through a robust R&D program to adequately assess the scalability to the DUNE FD scale. Several such avenues are being explored that would enhance the charge or light detection capabilities, or introduce new signals of interest. This section discusses two promising potential additives that have been previously demonstrated in large-scale LArTPCs. The first category is liquid xenon, which is of interest at low concentrations for impact on the scintillation light signal, and at higher concentrations as a signal source. The second includes photosensitive dopants that convert scintillation light to ionization charge.

These LAr dopants can be particularly impactful for DUNE Phase II prospects to broaden the low-energy physics program, targeting signals in the MeV to keV energy range. Detection of signals in this regime can enhance the GeV-scale neutrino oscillation physics program through enhanced neutrino energy reconstruction [83]. In combination with techniques that lower radioactive and external backgrounds, the detection of keV–MeV signals also provide sensitivity to a broad array of previously inaccessible signals spanning BSM physics and low-energy neutrino astrophysics. Examples include low-energy solar and SNB neutrinos, searches for rare decays such as $0\nu\beta\beta$, exotic physics such as fractionally-charged particles, and dark matter scattering. A more complete list can be found in [84]. An expanded program in these areas would complement DUNE's program while leveraging the large mass and deep-underground location.

3.4.1 Liquid xenon

Liquid xenon is a potential additive to the LAr in DUNE Phase II, either at a low (parts per million (ppm)) or high (up to the percent level) concentration. The loading techniques [85] and stability conditions [86] of LAr+LXe mixtures have been explored across this broad range of concentrations.

At low concentrations, the presence of xenon impacts the production of scintillation light in LAr, acting as a highly efficient wavelength shifter that converts the 128 nm primary scintillation wavelength in argon to a longer 178 nm wavelength. This has several advantages, including reduced Rayleigh scattering, improved light detection uniformity, a narrowing of the scintillation timing distribution, and a reduction in energy losses to impurities such as nitrogen. Such losses would result from non-radiative energy transfers involving the long-lived triplet state of Ar, transfers that are suppressed with the introduction of xenon. This leads to a much improved robustness of the scintillation light yield against LAr impurities, without appreciable impact on

the charge signal. In ProtoDUNE-SP xenon doping up to ~ 20 ppm verified the enhancements to optical response and the recovery of light yield in the presence of impurities [85]. Xenon doping at a 10 ppm level is already assumed in the FD2 Phase I module [60].

At higher concentrations, up to the percent level, xenon may also be of interest as a signal source. ^{136}Xe is a candidate isotope for $0\nu\beta\beta$ which, if observed, would establish the Majorana nature of the neutrino and demonstrate a violation of lepton number conservation [87]. The introduction of xenon, either in its natural form (8.9% ^{136}Xe) or enriched to ^{136}Xe, into a large-scale, deep-underground LArTPC detector could provide an opportunity to search for this important decay mode [41]. Mitigation of important backgrounds (^{39}Ar, ^{42}Ar, neutrons) near the 2.458 MeV Q-value for this decay are consistent with the requirements of other potential low-energy physics goals considered for DUNE Phase II, as described in Section 3.6. A key challenge for a competitive search is the massive procurement of xenon, at a level exceeding the world's current production by more than one order of magnitude, and possibly xenon enrichment at the same scale [88]. Another crucial challenge is achieving an energy resolution at the percent level for MeV-scale electrons; photosensitive dopants, discussed in the following, provide one avenue toward achieving this.

3.4.2 Photosensitive dopants

In a typical pure-LAr TPC, the energy deposited by charged particles is ultimately divided between ionization electrons, drifted in the electric field and detected at the anode plane, and scintillation light, detected by a photon detection system. The photon signal, which is produced promptly with ns-scale timing, is used for 3D event position reconstruction as well as triggering and absolute timing of neutrino interactions. In a LArTPC doped with a photosensitive dopant, the scintillation signal would be converted to ionization charge, effectively transferring the full deposited energy into that channel. Potential photosensitive dopants under consideration are a class of hydrocarbons with work functions on the order of the LAr (or Xe-doped LAr) VUV primary scintillation photon energy (7–9 eV). A dopant of this kind would convert scintillation light into ionization electrons very efficiently with minimal loss of spatial resolution.

The use of such dopants in LArTPCs can offer benefits to both the GeV- and MeV-scale physics programs of DUNE Phase II. In general, the transfer of deposited energy into the ionization channel leads to an enhancement of the ionization charge, which is measured with excellent efficiency in a LArTPC. This enhancement is particularly pronounced in regions of high energy deposition, improving prospects for particle identification using charge calorimetry. Furthermore, LAr with photosensitive dopants exhibits a significantly more linear relationship between deposited and visible charge, reducing the scale and uncertainties of corrections related to electron-ion recombination effects.

The general impact of such dopants in large-scale LArTPCs in practice was studied by the ICARUS Collaboration. ICARUS performed a long-term test of the Tetra-methyl-germanium (TMG) dopant in a three-ton LArTPC exposed to cosmic rays and γ sources, observing a clear enhancement in the ionization charge signal, and a significantly more linear response in reconstructed to deposited charge [89]. Importantly, this test also demonstrated long-term stability in realistic LArTPC operating conditions. A complete and detailed model of the

microphysics of energy transfer between LAr and candidate photosensitive dopants will require a comprehensive assessment of potential dopants and their ionization response across a broad range of signal energies for the Phase II program.

The enhancements provided by photosensitive dopants are particularly notable for improving energy resolution at low energies, e.g., to capture point-like signals at or below the MeV scale. A significant challenge with measuring such signals is the efficient collection of small amounts of scintillation light. In the Phase I design, a limited photon detection efficiency of order $\mathcal{O}(0.1\%)$ may limit the capabilities of DUNE to extract spectral information regarding MeV-scale signals, and thus to perform energy-based background mitigations. Ideally, a detector would measure both the ionization and scintillation anti-correlated signals to measure a precise total energy, as in the case of the EXO-200 experiment [90] and as also investigated in [91].

In principle, a large LArTPC can achieve percent-level energy resolution for MeV-scale signals of interest, but this would require detection of tens of percent of the scintillation photons, a level of efficiency impractical with current and near-future designs. Meanwhile, by converting the isotropic scintillation light into directional ionization charge, photosensitive dopants at the ppm level could allow the full energy to be measured with high efficiency by the TPC charge detection system. In this sense, charge alone would provide a precise energy measurement, analogous to a correlated charge/light measurement. Previous work in the context of LAr calorimeters has also considered the impact of several candidate dopants on MeV-scale α particles, demonstrating substantial charge enhancements for low-energy events with relatively large scintillation signals [92]. Straightforward future R&D using β or γ sources to study the low-energy electromagnetic response can further clarify the impact and achievable energy resolution for MeV-scale signals of interest for beam neutrino energy measurements, low-energy neutrino astrophysics, and keV- to MeV-scale BSM signatures. To fully realize the potential of photosensitive dopants in LArTPCs, studies to explore the microphysics involved, and R&D to determine the optimal dopant types and concentrations, will also be needed.

3.5 Hybrid Cherenkov plus scintillation detection

The THEIA hybrid Cherenkov+scintillation detection concept is motivated by a science program of low-energy astroparticle, rare event, and precision physics (Section 3.5.2). It also contributes to the overall CPV sensitivity (Sec. 2.1). The envisioned 25 kt THEIA detector offers good particle and event identification at both low and high energies, coupled with a target of high radio-purity, no inherent radio isotopes, and excellent neutron shielding. This allows the detector to probe physics that requires low threshold and low background.

3.5.1 Hybrid detection concept

A detector of the envisioned hybrid design would separate Cherenkov and scintillation light by the use of a novel liquid scintillator [93], fast timing, and spectral sorting. Cherenkov light offers electron/muon discrimination at high energy via ring imaging and sensitivity to particle direction at low energy. The scintillation signature offers improved energy and vertex resolution,

PID capability via species-dependent quenching effects on the time profile, and low-threshold (sub-Cherenkov-threshold) particle detection. The combination boasts an additional handle on PID from the relative intensity of the two signals.

This detector design, being developed as THEIA, would offer excellent energy resolution for high-energy neutrino interactions (better than 10% neutrino energy resolution has been achieved with preliminary algorithms), along with access to a rich program of low-energy, rare-event, and precision physics.

This is likely a cost-effective option, particularly among those designed to broaden the physics program, thanks to the relatively simple and well-understood detector design that omits both cryostat and field cage. The THEIA detector concept is shown in Figure 23.
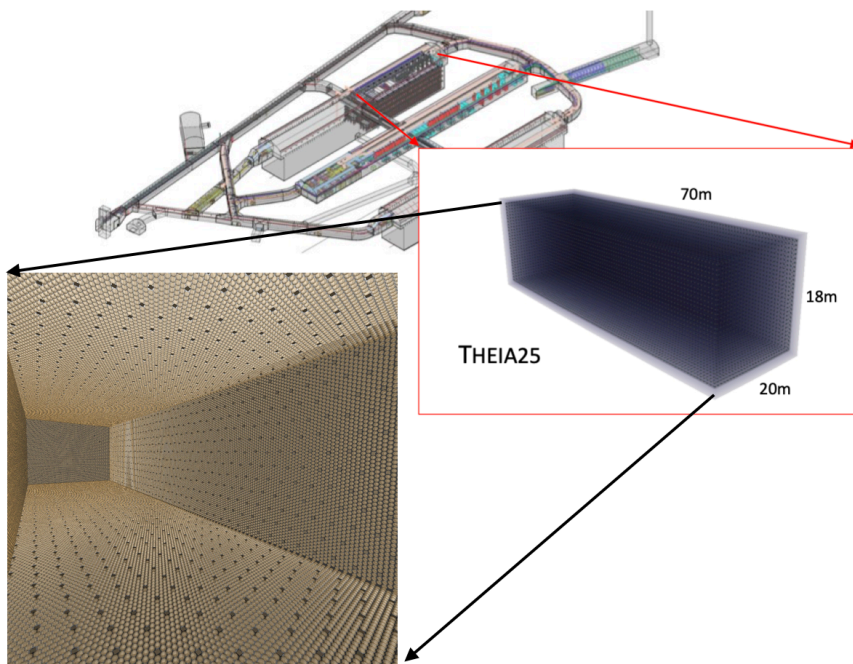
Figure 23: Illustration of sited in a DUNE FD cavern, with an interior view of the THEIA-25 concept modeled using the Chroma optical simulation package [94]. Taken from [12].

3.5.2 Theia physics program

THEIA will seek to make leading measurements over as broad a range of neutrino physics and astrophysics as possible. The scientific program includes:

- observations of solar neutrinos – both a precision measurement of the CNO flux, and a probe of the MSW transition region;

- determination of neutrino mass ordering and measurement of the neutrino charge conjugation and parity (CP)-violating phase δ_{CP};

- observations of diffuse supernova neutrinos, and sensitivity to neutrinos from an SNB with directional sensitivity;

- sensitive searches for nucleon decay in modes complementary to LAr; and, ultimately,

- a search for $0\nu\beta\beta$, with sensitivity reaching the normal ordering regime of neutrino mass phase space ($m_{\beta\beta} \simeq 6$ meV).

Table 2 summarizes the physics reach of THEIA-25. The full description of the analysis in each case can be found in [12].

Table 2: Projected THEIA physics reach, from Ref. [12]. Exposure is listed in terms of the fiducial volume assumed for each analysis. The total detector volume assumed is $70 \times 20 \times 18$ m^3. For $0\nu\beta\beta$, the target mass assumed is the mass of the candidate isotope within the fiducial volume (assumed to be housed within an inner containment vessel). Limits are given at the 90% CL.

Physics Goal	Reach	Exposure (Assumptions)
Long-baseline oscillations	Equivalent to 10-kt LAr module	127 kt-MW-yr
Supernova burst	$< 2°$ pointing accuracy 5,000 events	25-kt detector, 10 kpc distance
DSNB	5σ discovery	125 kt-yr (5 yr)
CNO neutrino flux	$< 10\%$	62.5 kt-yr (5 yr, 50% fid. vol.)
Reactor neutrino detection	2000 events	100 kt-yr (5 yr, 80% fid. vol.)
Geo neutrino detection	2650 events	100 kt-yr (5 yrs, 80% fid. vol.)
$0\nu\beta\beta$	$T_{1/2} > 1.1 \times 10^{28}$ yr	211 ton-yr ^{130}Te
Nucleon decay $p \to \overline{\nu}K^+$	$\tau/B > 1.11 \times 10^{34}$ yr	170 kt-yr (10 yr, 17-kt fid. vol.)
Nucleon decay $p \to 3\nu$	$\tau/B > 1.21 \times 10^{32}$ yr	170 kt-yr (10 yr, 17-kt fid. vol.)

3.5.3 Technology readiness levels

The THEIA reference design makes use of a number of novel technologies to achieve successful hybrid event detection. This design would be used to enhance the Cherenkov signal by reducing and potentially delaying the scintillation component. The use of angular, timing, and spectral information offers discrimination between Cherenkov and scintillation light for both low- and high-energy events. Fast photon detectors – such as the 8" PMTs now manufactured by Hamamatsu, which have better than 500 ps transit time spread – will be coupled with spectral sorting achieved via use of dichroic filters [95].

Successful separation of Cherenkov and scintillation light has been demonstrated even in a standard scintillator like LAB-PPO [96] with the use of sufficiently fast photon detectors, and will be even more powerful when coupled with the spectral sorting capabilities envisioned for THEIA.

Radiopurity levels exceeding the requirements for the THEIA low-energy program have been successfully demonstrated by water Cherenkov experiments (SNO) and scintillator experiments (Borexino).

Further optimization of the design could be achieved by considering deployment of Large Area Picosecond Photo-Detectors (LAPPDs) [97, 98], for improved vertex resolution, or slow scintillators [99, 100] to provide further separation of the prompt Cherenkov component from the slower scintillation. A more complete discussion of the relevant technology is provided in [101].

The R&D for THEIA will be completed with the successful operation of a number of technology demonstrators currently under construction: (i) a one-ton test tank and a 30-ton Water-based Liquid Scintillator (WbLS) deployment demonstrator at Brookhaven National Laboratory (BNL) will demonstrate the required properties and handling of the scintillator; (ii) a low-energy performance demonstrator, , at Lawrence Berkeley National Laboratory (LBNL) [102] will demonstrate the performance capabilities of the scintillator, fast photon detectors, and spectral sorting; and (iii) a high-energy demonstration at ANNIE, at Fermilab, will validate GeV-scale neutrino detection using hybrid technology [103]. These detectors are all currently operational or under commissioning.

3.6 Background control

The potential to enhance the physics scope of DUNE Phase II with lower energy thresholds has been attracting significant attention within the wider community [84]. The proposed ideas tend to rely on two enhancements over the Phase I program: greater control of radioactive backgrounds and improved energy resolution at lower energies. DUNE is well placed to improve the lower-energy physics scope, first because of the depth of the FD, which is well shielded from cosmic-induced backgrounds. Secondly, the sheer size of the detector volumes allows for significant fiducialization to reduce external backgrounds originating within the SURF cavern rock and shotcrete. Phase II designs that minimize material in the active regions, such as the FD2 or dual-phase (DP) designs, are most favorable for low-background physics due to reduced risk of radioactive backgrounds.

We can define two natural physics target energy regions. While these targets are motivated by the intrinsic backgrounds in argon-based detector modules (Sections 3.2 through 3.4), most of this background control discussion also applies to water-based detectors (Section 3.5), as detailed in the following.

The first background target extends the energy threshold down to about 5 MeV. With careful control of neutron, γ, and radon related backgrounds, combined with improvements in the low-energy readout, an extended SNB neutrino program can be envisaged, with improved reach in terms of supernova distance sensitivity (to the Magellanic Clouds), for elastic scatters with improved directionality, and to the (softer energy) early or late parts of the supernova neutrino flux. A low-energy threshold could also allow a precision solar neutrino program to explore solar-reactor oscillation tensions and non-standard interactions. In an argon-based detector, this 5 MeV threshold is set by the intrinsic ^{42}Ar-^{42}K decay chain, as shown in Figure 4.

The second background target would extend the energy threshold to even lower values of

~1 MeV or less. With such a low threshold, ambitious but high-reward physics measurements would include: solar CNO measurements; searches for $0\nu\beta\beta$ with xenon loading; and even high-mass weakly interacting massive particle dark matter detection could be possible [37]. In an argon-based detector, this could be accomplished only by using underground sources of argon, thus largely suppressing the intrinsic ^{42}Ar activity.

This section outlines some of the most significant radioactive backgrounds and identifies paths to reduce them in Phase II detector modules.

3.6.1 External neutrons and photons

In DUNE Phase I, the dominant background to low-energy SNB neutrinos will be from external neutrons, that is neutrons originating from outside the detector (SURF cavern rock and shotcrete). These neutrons are primarily of radiogenic origin. When captured in the LAr, they can produce 6.1 MeV or 8.8 MeV γ cascades which Compton scatter or pair produce electrons that directly mimic the CC neutrino signals. On the other hand, in a water-based detector, neutron captures on free hydrogen would result in lower-energy gammas of 2.2 MeV.

To remove external neutrons in argon-based detectors, passive shielding can be deployed, as first suggested in [31]. A layer of 40 cm of water, or 30 cm of polyethylene or borated polyethylene, is sufficient to attenuate the neutron flux from spontaneous fission or (α, n) reactions in the rock by 3 orders of magnitude, making it subdominant. A shield of this size fits within the warm support structure of the cryostat. Alternative approaches would involve modifications to the cryostat design, for example, layering the insulating foam with neutron-capturing materials such as gadolinium-doped acrylic. These same measures will ameliorate the cavern γ background originating from ^{238}U and ^{232}Th natural decay chains.

In a water-based detector, no passive neutron shield around the detector would be necessary. Excellent neutron shielding via detector fiducialization would be reached in this case thanks to the plentiful free hydrogen available as part of the detector target.

Spallation-induced neutron and cosmogenic background events are also possible, though they are primarily short-lived and expected to be orders of magnitude less than the radiogenic backgrounds. A full study of these backgrounds in [104] show that these can be further reduced by tagged-muon-proximity event selections.

3.6.2 Internal backgrounds from detector materials

After the external cavern neutrons, the most significant source of neutron background comes from contaminants in materials within the detector, from (α, n)-induced reactions within the cryostat and other components. Photons produced in these events can also distort reconstructed quantities due to light flash or charge blip backgrounds, particularly when close to the readout, such as the cryostat-mounted light sensors. Dark matter experiments have successfully managed such backgrounds with careful material selection programs, using radioactive assay techniques to select favorable materials for detector construction, and to ensure quality assurance during production and installation processes. The world-leading argon-based dark matter detectors have lowered backgrounds by five orders of magnitude below the DUNE Phase I target. To maintain the sub-dominance of these internal backgrounds relative to externals removed by

shielding, a DUNE Phase II argon-based detector module will require a less stringent reduction target of three orders of magnitude on detector components such as cryostat stainless steel [19].

For a THEIA-type module, internal backgrounds within the fiducial volume are driven by the cleanliness of the target itself. The chemical purity of the water-based liquid scintillator target is 10^{-17} g/g in both uranium and thorium contaminants, which is considered achievable by improving target material purification techniques [12].

3.6.3 Intrinsic backgrounds from unstable isotopes in the target

Argon extracted from the atmosphere contains two background isotopes that can limit sensitivity at the lowest energy for any argon-based detector: ^{39}Ar, with a decay Q-value of 565 keV; and ^{42}Ar, with a decay Q-value of 599 keV and its daughter isotope ^{42}K, which decays with a Q-value of 3525 keV. The ^{42}Ar-^{42}K chain sets a lower limit of about 5 MeV, dependent on the ultimate low-energy resolution, for low-threshold physics with atmospheric argon. Dark matter experiments have successfully extracted argon from underground sources, which are depleted in both ^{42}Ar and ^{39}Ar [105]. These experiments show reduction factors of order 1400 for ^{39}Ar and have seen no ^{42}Ar. The currently only known source of underground argon is too small to fill a detector the scale of DUNE, but work is ongoing to identify new, larger sources which can be used cost-effectively. Recent estimates of the potential reduction of ^{42}Ar in underground-sourced argon is expected to be eight orders of magnitude [106].

Intrinsic argon background contributions would be absent in a THEIA-type module. The most abundant radioactive isotope in this target material would be ^{14}C. With a decay Q-value of 156 keV, ^{14}C would not be a relevant background for any of the low-energy physics measurements and searches discussed in Section 2.2 in connection with a THEIA module.

3.6.4 Radon background

Radon gas has high mobility, emanates from all detector materials, and can diffuse easily throughout the entire detector volume. This background can mimic directly low-energy neutrinos, through (α, γ) reactions and misidentified α events in the detector. It also produces daughter products which can plateout on internal components such as the photon detector system, distorting the low-energy reconstruction. Several approaches should be adopted to control this background, including: direct removal of radon in the purification system using an inline radon trap; selection of detector materials for low radon emanation; surface treatments to contain or remove radon sources; removal of a significant emanation source from dust by controlling and cleaning to higher cleanliness standards than in Phase I; removal of radon from air during installation to lower the risk of plateout backgrounds when the detector is open; and analysis techniques such as α tagging by pulse shape discrimination.

3.6.5 The SLoMo concept

One proposed design for a low-background, argon-based, Phase II far detector is the Sanford Underground Low background Module (SLoMo). This design, shown in Figure 24 provides a path to lower background levels using the techniques outlined above, reducing most background

sources by three orders of magnitude below the expected Phase I levels. This is combined with a significant increase in light coverage within the detector using high quantum efficiency, DarkSide-style, SiPM tiles [107] to increase the energy resolution and pulse shape discrimination power at lower energies.
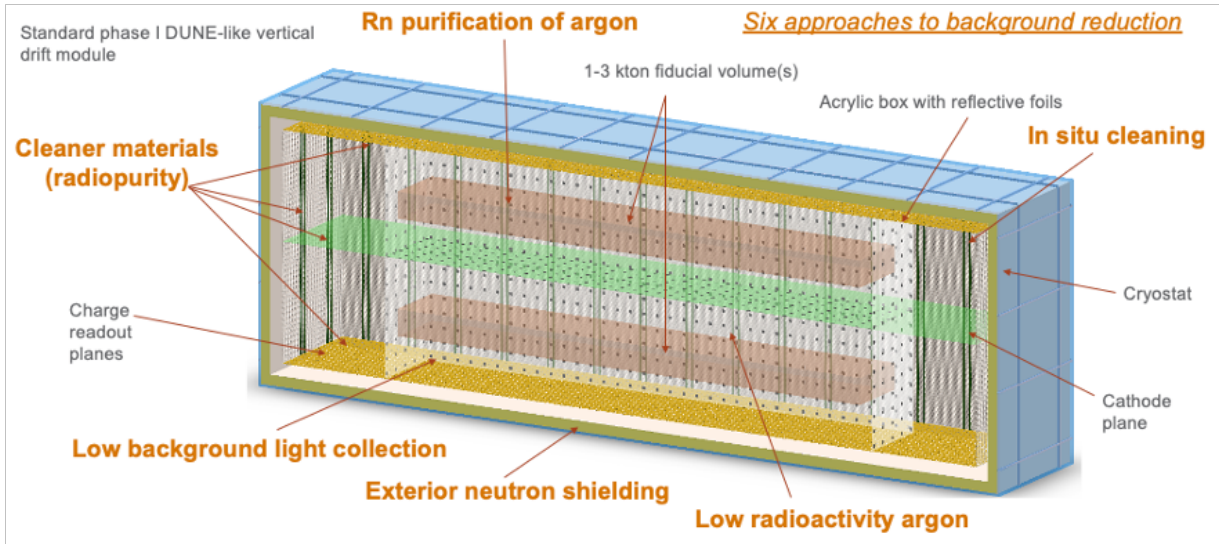
Figure 24: Design for SLoMo, highlighting background control methods required to achieve goals.

To get this light coverage, SLoMo aims to densely instrument an interior 1–2 kt of highly fiducialized underground argon (UAr) in the center of a vertical drift-like detector. The structure on which to mount the DarkSide SiPM modules is not fixed in this design, though we propose light-tight acrylic walls covered in wavelength-shifting foils. Reference [19] shows that a 20% SiPM coverage, combined with charge detection by existing VD CRPs and viewing an inner volume, should easily lead to a sub-2% energy resolution (sigma) at 2 MeV. This feature, along with the negligibly low amount of ^{42}Ar in UAr, makes possible $0\nu\beta\beta$ studies with xenon loading, should this be a program DUNE wishes to pursue. Reducing ^{42}Ar to very low levels also allows detectable energy spectra from a supernova to reach well into the region where $\nu_e - e$ elastic scattering dominates and thus pointing, in principle, is improved. A 20% SiPM module coverage would come at an affordable cost and would detect enough photons to allow pulse shape discrimination. The combination of high SiPM coverage, low neutron background, fiducialization and radon control would allow competitive WIMP dark matter searches in SLoMo. Solar CNO investigations would also become possible, as would observation of further phenomena, such as the "supernova glow" [108]. This design is outlined in [19], where the significant physics gains are further explained.

3.6.6 Research and development requirements

All the Phase II options to lower the energy threshold require a radioactive background budget to be specified and low-background techniques to be deployed to ensure it is achieved. The

R&D required to achieve these goals includes:

- Large-scale materials and assay campaigns, scaling up material selection techniques used by low-background fundamental physics experiments to the kt scale.

- Cleanliness requirements and approaches for the kt scale.

- Radon control in detector liquids, including emanation assay and control at the FD scale.

- Low-background photon detection systems, developing new designs that can increase the light detection efficiency without overwhelming a background budget.

- Background model and simulation campaign for physics sensitivity analyses.

- Novel analysis techniques, such as pulse shape discrimination, to remove background events.

- Compact shield designs for argon-based modules, that can fit in the limited DUNE cavern space or within the cryostat structure.

- New sources of underground argon, capable of filling an argon-based DUNE FD module cost-effectively.

3.7 Toward detector concepts for Phase II FD modules

The DUNE FD2 vertical drift technology forms the basis for the reference design for FD3 and FD4. As such, the R&D for FD3 and FD4 is primarily focused on upgraded photon detector and charge readout systems for the vertical drift layout. Most of these candidate systems are either further developments of the current systems or replacements based on technologies that are already under active R&D or in early prototyping phases. A non-LAr option such as THEIA is also under consideration as an alternative technology for FD4. A summary of technologies under consideration, both LAr and non-LAr options, for these FD modules, along with R&D status and plans, is provided in Table 3.

The detector technologies described in the previous sections (Section 3.2 through 3.6) will form the building blocks to define full detector designs for both FD3 and FD4. These technologies are not standalone, and most of them can be combined or integrated together, as shown in Table 4. It is important to note that the check marks in the table for FD3 are not solely driven by Technology Readiness Level (TRL) since several other technologies listed (e.g., ARIADNE, LArPix) are also technically mature.

The choices for FD3 are primarily motivated by how straightforward the proposed upgrades are to implement without requiring major modifications to the baseline FD2 design on which FD3 will be based. This is an important consideration since in the case of FD3, the DUNE collaboration is aiming to meet the technically limited schedule, which calls for FD3 installation to start no later than 2029. However, as the other technologies listed in Table 3 evolve, they may demonstrate that they meet our FD3 requirements. If so, and if timelines can be met,

Technology	Prototyping Plans	Key R&D Goals
CRP (Sec. 3.3.2)	**2024:** Cold Box tests at CERN. **2025-2026:** ProtoDUNE-VD at CERN.	Port LArASIC to 65 nm process
APEX (Sec. 3.3.1)	**2024:** 50 L & 1-ton prototypes at CERN. **2024-2025:** $\mathcal{O}(100)$-channel demonstrator at Fermilab. **2025-2028:** ProtoDUNE-VD at CERN.	Mechanical integration of APEX PD in field cage
		Signal conditioning, digitization and multiplexing in cold
LArPix, LightPix (Secs. 3.3.3 and 3.3.5)	**2024:** 2x2 ND demonstrator at Fermilab. **2024-2025:** Cold Box tests at CERN. **2026-2028:** ProtoDUNE at CERN.	Micropower, cryo-compatible, detector-on-a-chip ASIC
		Scalable integrated 3D pixel anode tile
		Digital aggregator ASIC and PCB
Q-Pix, Q-Pix-LILAr (Secs. 3.3.3 and 3.3.5)	**2024:** Prototype chips in small-scale demonstrator. **2025-2026:** 16 channels/chip prototypes in ton-scale demonstrator at ORNL. **2026-2027:** Full 32-64 channel "physics chip".	Charge replenishment and measurement of reset time
		Power consumption
		R&D on aSe-based devices and other photoconductors
ARIADNE (Sec. 3.3.4)	**2024:** Glass THGEM production at Liverpool. **2025-2026:** ProtoDUNE-VD at CERN.	Custom optics for TPX3 camera
		Light Readout Plane design with glass-THGEMs
		Characterization of next-generation TPX4 camera
SoLAr (Sec. 3.3.5)	**2024:** Small-size prototypes at Bern. **2025-2028:** Mid-scale demonstrator at Boulby.	Development of VUV-sensitive SiPMs
		ASIC-based readout electronics
Hybrid Cherenkov+ scintillation (Section 3.5.1)	**2024-2025:** Prototypes at BNL (1- & 30-ton), LBNL (Eos), Fermilab (ANNIE). **2025-26:** BUTTON at Boulby.	Theia organic component manufacturing
		Theia *in situ* purification
		Spectral photon sorting (dichoicons)

Table 3: Prototyping plans and key R&D goals for the main Phase II FD technologies under consideration.

they will remain under consideration for FD3 (with the exception of THEIA). Therefore, their continued R&D in view of FD3 is encouraged.

While full detector solutions will be defined in the forthcoming years through dedicated design reports, the following outlines the high-level detector concepts currently under consideration by the DUNE collaboration.

Technology	Option for FD3	FD4	Can integrate with
CRP (strip-based charge readout)	✓	✓	APEX
APEX (X-ARAPUCA light readout on field cage with SiPMs)	✓	✓	CRP, LArPix, Q-Pix, ARIADNE, SoLAr
LArPix, **LightPix** (pixel charge and light readout)		✓	APEX, SoLAr
Q-Pix, **Q-Pix-LILAr** (pixel charge and light readout)		✓	APEX, SoLAr
ARIADNE (dual-phase with optical readout of ionization signal)		✓	APEX
SoLAr (integrated charge and light pixel readout)		✓	APEX, LArPix, Q-Pix
Hybrid Cherenkov + scintillation		✓	N.A.

Table 4: LArTPC integration of the detector technologies currently being considered for the Phase II FD modules. Here, "FD3" refers to the FD3 reference design requiring only minimal modification to the FD2 vertical drift design. The "FD4" options could also become options for FD3 over time.

For FD3, we envisage a vertical drift LArTPC that is similar in concept to FD2 (Section 3.2). We do not anticipate any changes to the FD2 high voltage system, with two drift volumes of 6.5 m drift length each. The CRPs at both anodes would feature three 2D projective views of the events, obtained from two double-sided perforated PCBs stacked together, similar to FD2. Continued R&D beyond the current CRP design for FD2 will focus on optimizations of strip pitch, length and orientation, as well as on streamlining CRP construction techniques (Section 3.3.2). Upgrades to FD2 charge readout electronics are possible, such as the adoption of the 65 nm process for the fabrication of all FD3 ASICs.

The FD3 PDS would be composed of X-ARAPUCA-based PD modules read by SiPMs using PoF and SoF, similar to FD1 and FD2. The installation location (field cage, cathode and/or membrane wall), optical coverage, and PD module design of the FD3 PDS will be determined through APEX technology R&D (Section 3.3.1). This R&D will also determine the reference solution for PDS readout electronics, particularly whether analog optical signals will be transmitted outside the cryostat as in FD2, or a digital optical transmission solution will be adopted. Background control could include incremental improvements over FD2 protocols, but no dedicated passive shields (beyond the cryostat itself) nor underground argon (Section 3.6)

would be deployed. We envisage LAr doping as for FD2, via the addition of trace (ppm-level) amounts of liquid xenon (Section 3.4).

The concepts for FD4 introduce further improvements. The concept for the reference design is a vertical drift LArTPC with a central cathode and two anodes with pixel-based readouts. The projective readout of CRPs would be replaced by a native 3D charge readout system, either employing charge pixels (see LArPix and Q-Pix technologies in Section 3.3.3) or through an optical-based charge readout (see ARIADNE technology in Section 3.3.4). The anode pixels may also serve as scintillation light detection units (see the SoLAr, LightPix and Q-Pix-LILAr options in Section 3.3.5). The symmetric TPC configuration may in principle allow for implementation of different pixel-based solutions at the top and bottom anodes, depending on the R&D outcome and available resources, as is the case for the different top and bottom electronics adopted in FD2.

A single-drift LArTPC solution for FD4 with a unique ARIADNE-based anode plane on top and the cathode placed at the bottom of the detector is also possible. This solution would require upgrades to the HV system to accommodate a longer (13 m) drift. Commercial 600 kV power supplies with fluctuations in the output voltage that are sufficiently small for this application already exist. On the other hand, R&D would be needed to scale up the high-voltage feedthrough design currently being used in the ProtoDUNE-VD demonstrator, in order to adapt to the larger diameter high-voltage cable and to the higher voltage values. Scintillation light detection away from the anodes would be performed with X-ARAPUCA modules further improved from FD3 (see Section 3.3.1). Compact shield designs and greater control of radioactive backgrounds would be explored for FD4, given that an important goal for this module would be to extend the physics scope to lower energy thresholds.

A hybrid detector module capable of separately measuring scintillation and Cherenkov light (see THEIA technology in Section 3.5) would provide a fully complementary detection technology for FD4 compared to FD1-3, and currently forms the basis of the alternative FD4 concept being explored by the DUNE Collaboration. This module would be designed for both high-precision Cherenkov ring imaging and long-baseline neutrino oscillation sensitivity, and a rich program across a broad spectrum of physics topics in the MeV-scale energy regime, see Table 2. This can be achieved via either a phased approach, with both the light yield of a water-based liquid scintillator target and the coverage of fast-timing photosensors increasing over time in order to broaden the physics program, or with a high light-yield liquid scintillator and sufficient Cherenkov separation to preserve the Cherenkov purity from the start. Near detector options for non-LAr FD modules are discussed in Section 4.4.

The DAQ system for FD3 and FD4 will be based on the same architecture designed for the first two FD modules. The DUNE timing system will be extended to these modules, facilitating inter-module synchronization and triggering. Most likely, the DAQ will pursue the use of Ethernet and standard protocols for the readout interface to the detector electronics. Raw data will be stored using the same file format, easing the integration with offline computing. The configuration, control, and monitoring system will be re-used, with customizations as needed. Use of the existing DAQ software will allow us to focus efforts on the aspects that may be implemented differently, and to take advantage of advances in computing technologies. For example, the trigger and data filter may evolve to rely on more sophisticated data processing

techniques and technologies, such as Artificial Intelligence (AI), particularly at low energies.

Decisions on the technology choices for FD3 and FD4 are expected to come no later than 2027 and 2028, respectively. As noted earlier in this section, the reference designs for FD3 and FD4 are upgraded versions of the vertical drift LArTPC technology, with THEIA serving as an alternative technology choice only in the case of FD4.

The final design milestones for Phase II FD modules are driven by the number and extent of the upgrades planned. For example, in the case of an FD2-like module where the only upgrades are optimization of CRPs and the APEX light system, one can envision being ready for by 2028 in a technically limited schedule. In this scenario, the earliest start for installation of FD3 can be anticipated in 2029 with completion of installation and filling in 2034. Alternatively, if one were to implement pixel-based upgrades such as LArPix, Q-Pix, SoLAr, or ARIADNE (top anode plane only), the FDR milestone would likely be delayed until at least 2030.

An asymmetric DP vertical drift LArTPC for FD4, with a single drift volume instrumented via a single ARIADNE readout plane, would require significant changes to the HV system. It is possible to reach the FDR milestone for this option by 2031-32. In the case of the THEIA option, a FDR milestone no earlier than 2033 is anticipated. The ProtoDUNEs at CERN will continue to serve as important platforms to demonstrate several of these technologies and their potential for integration.

4 The DUNE Phase II near detector

In Phase II, DUNE will have accumulated FD statistics of several thousand oscillated electron neutrinos, resulting in statistical uncertainties at the few-percent level on the number of electron appearance events. To reach the physics goals of DUNE, a similar level of systematic uncertainty must be achieved, which requires precise constraints from the ND. To understand the needs of the Phase II ND, we must first understand the expected performance of the Phase I ND, which consists of two measurement systems, ND-LAr+TMS, and SAND. In Section 4.1, we describe why the Phase I ND is critical for DUNE physics, discuss limitations inherent to its design, and outline the Phase II requirements that are needed to provide improved constraints on the argon-based FD data sample. This is a difficult challenge as the ultimate performance of the Phase I ND is not yet understood, and will depend on analysis techniques developed over the coming decade. Section 4.2 describes a detector concept that meets the design motivations of Section 4.1. Further improvements may come from upgrades to the Phase I ND components, see Section 4.3. Near-detector options to constrain possible non-argon FD data samples are discussed in Section 4.4.

4.1 Design motivations

The Phase I ND-LAr+TMS detector is designed to measure neutrino interactions on the same nuclear target as the FD, and with a detector response similar to the FD. Neutrino energy in the FD is estimated by summing the lepton energy with the hadronic energy. The FD measures the muon energy by range, and the energies of all other particles calorimetrically, in both cases

exploiting energy deposits occurring in LAr. The ND-LAr+TMS detector also measures muons by range, and other particles calorimetrically. It is able to reconstruct the same observables as the FD, and measures them with essentially the same resolutions, in an unoscillated beam. This capability is the core requirement of the DUNE ND, and will be a critically important constraint for all DUNE long-baseline measurements. The ND-LAr+TMS system moves off-axis (via DUNE-PRISM) to collect data at different fluxes, and directly constrains the energy dependence of neutrino cross sections. SAND is permanently on-axis, and measures neutrino cross sections on various nuclear targets while also monitoring the beam. SAND has a LAr target, so that it can also measure cross section ratios, including on argon.

The dimensions of Phase I ND-LAr are driven by containment of electrons and hadrons, rather than by event rate, so that they can be measured calorimetrically in the same way as in the FD. To minimize cost, the dimensions have been chosen to be as small as possible while maintaining full coverage of the neutrino-argon phase space. However, this means that the acceptance is non-uniform and depends on the event kinematics, complicating the calorimetric energy measurement. Beam-induced muons will be reconstructed by the ND-LAr+TMS combined system. TMS is able to provide sign selection of muons, which is especially important to reject wrong-sign backgrounds in antineutrino mode. However, ND-LAr itself is not magnetized, so the sign selection is only possible for the muons that enter TMS ($\gtrsim 800$ MeV kinetic energy), and there is no sign selection for other particles. While TMS will provide muon momentum and sign reconstruction for the energy region relevant for long-baseline oscillation physics, the design is such that muons above 6 GeV kinetic energy will not be ranged out nor sign-selected.

The main purpose of the SAND detector will be to monitor the neutrino beam, but it will also be capable of making independent measurements of the neutrino flux and flavor content. This additional capability adds robustness to the ND complex, enabling better control over systematics and background. Phase I SAND will be able to measure the sign of all charged particles in its low-density CH_2 tracker, but not generally for hadrons produced in the argon target. The SAND tracker will also measure neutrino cross sections on carbon and hydrogen targets.

To constrain neutrino-argon interaction modeling, it is useful to identify specific exclusive processes. Of those, about two thirds of neutrino interactions in DUNE will have pions in the final state. ND-LAr is an excellent detector for identifying pions and protons when they are above threshold, and do not undergo strong interactions inside the detector. However, many events in the DUNE energy range have pions with hundreds of MeV kinetic energy, which travel several interaction lengths and frequently scatter, transferring some energy to the atomic nuclei that is then not seen in a calorimetric energy reconstruction. On the other hand, below threshold pions decay to final state particles, including neutrinos, leading to large fractions of their rest mass not being visible calorimetrically. Also, protons below 300 MeV/c are impossible to detect in ND-LAr because they deposit all of their energy over a range of only a few mm, producing highly saturated ionization charges recorded on a single pixel. Predictions on the multiplicity of such low-momentum protons from neutrino-argon interaction models are particularly uncertain.

These Phase I limitations motivate the design of the Phase II ND. Specifically, the Phase II

ND should have, when compared to the Phase I ND:

- argon as the primary target nucleus,

- improved PID across a broad range of energies and angles,

- lower tracking thresholds for protons and pions,

- minimal secondary interactions in the tracker volume,

- 4π acceptance over a wide range of momenta, and

- magnetization to achieve sign selection over a broader muon momentum range.

Employing an argon target will ensure that constraints from the Phase II ND can be applied directly to the argon-based FD without any extrapolation in atomic number.

A broad acceptance and high PID efficiency will enable exclusive final states to be identified, which will improve the constraints on neutrino interaction modeling. Low thresholds will make the Phase II ND highly sensitive to nuclear effects. Magnetization will ensure sign selection at all energies and angles, for both charged leptons and charged pions.

In the event that one of the Phase II FD modules consists of a neutrino target material that is not argon-based and of a detector technology other than LArTPC, such as the THEIA detector concept described in Section 3.5, the requirements for the Phase II ND complex will need to be expanded to account for the additional target material(s) and the different neutrino detection method.

4.2   Phase II improved tracker concept

For Phase II, an improved tracker concept based on a GArTPC would replace TMS downstream of ND-LAr. Drawings for the envisaged layouts of the Phase I and Phase II detector suites are shown in Figure 25. A GArTPC can reconstruct pions, protons and nuclear fragments with lower detection thresholds than a LArTPC can. Figure 26, which compares the same simulated event in each, shows this. The protons travel a much longer distance and can be more clearly separated in gaseous argon. The GArTPC is also less susceptible to confusion of primary and secondary interactions, since secondary interactions occur infrequently in the lower-density gas detector. If the TPC is inside a magnetic field, it can better distinguish neutrinos and antineutrinos and can determine the momenta of particles whose trajectories are not contained in the detector. It can also measure neutrino interactions over all directions, unlike the ND-LAr, which loses acceptance at high angles with respect to the beam direction. Therefore, a GArTPC detector system at the near site, called ND-GAr in the following, provides a valuable and complementary data sample to better understand neutrino-argon interactions.

However, a drawback of a GArTPC is the lower neutrino event rate in a given volume due to the lower density. One way to improve this is to use high-pressure argon gas. A cylindrical volume with a diameter and length both of roughly 5 m, and gas at 10 bar, would have a fiducial mass of nearly one ton of argon, yielding approximately one million neutrino
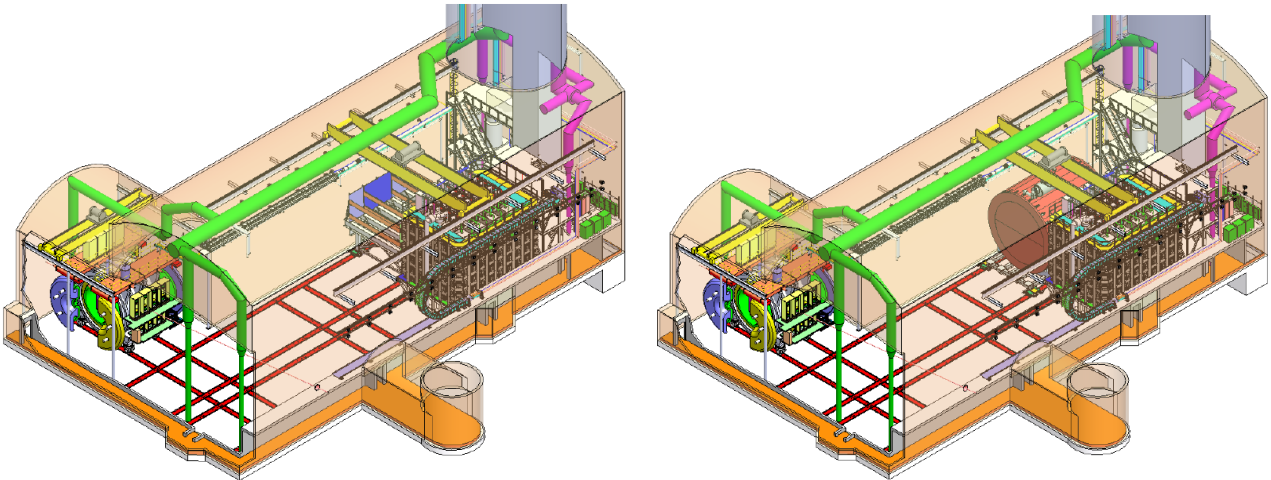
Figure 25: Layout of the envisaged Phase I (left) and Phase II (right) ND suite. The neutrino beam enters from the bottom-right corner, and exits at the top-left corner, of the drawings. The SAND detector is shown at its permanent on-axis location, while all other detectors upstream are shown at their maximum off-axis location.

interactions per year. The trade-off between sufficient target mass and low detector density has not been optimized, but would nonetheless be adjustable during operations by setting the detector pressure.

As illustrated in Figure 27, the reference design concept for the ND-GAr detector comprises:

1. a pressurized GArTPC,

2. a surrounding calorimeter,

3. a magnet, and

4. a muon-tagging system.

A PDS may also prove necessary to reduce pileup and to provide the event t_0 for the drift time determination in events that do not reach the calorimeter. It would also help improve the track matching between the TPC and the external calorimeter and muon systems [110]. All these subsystems are described in the following. The entire ND-GAr system will move perpendicularly to the beam direction together with ND-LAr, as part of the DUNE-PRISM concept.

This detector concept is motivated by the considerations in Section 4.1. It also affords significant opportunities to study BSM physics, as discussed in Section 2.3.

4.2.1 Charge readout of TPC

A variety of techniques can be used to amplify and collect the ionization electrons after their drift to the TPC anode, and the options currently under consideration for ND-GAr are briefly
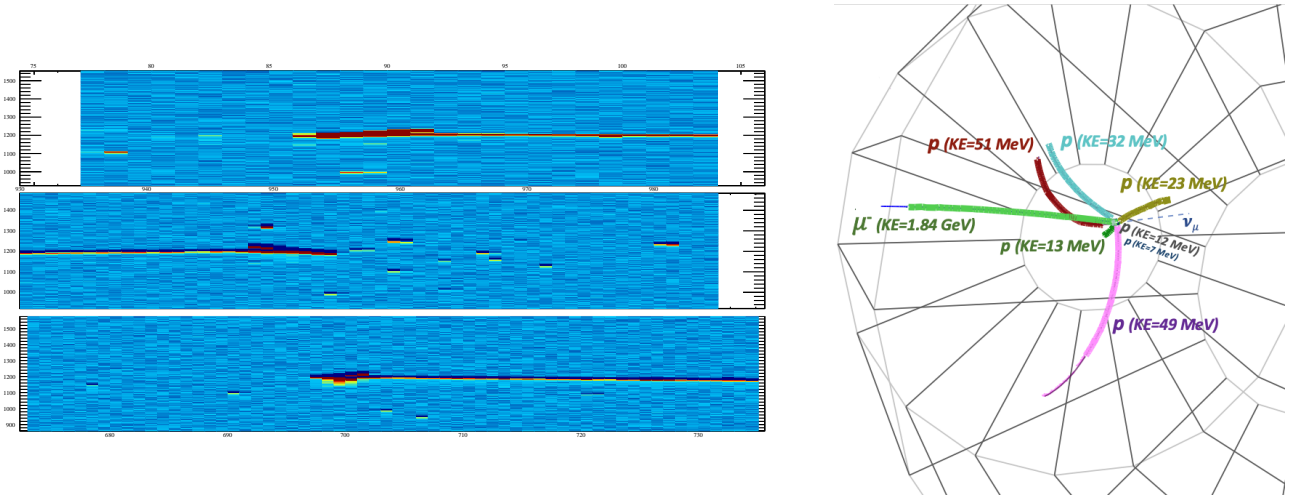
Figure 26: The same CC ν_μ event with seven low energy protons (kinetic energies ranging from 7 to 51 MeV) simulated in a LArTPC (left) and a GArTPC (right). The LArTPC event display shows time ticks versus channel number for the three projective views of the event. The GArTPC reconstruction algorithm finds all eight tracks in the event (seven proton tracks and one muon track), although only six are visible by eye in this view. All proton tracks travel 2.4 cm or less in LArTPC. From [109].

presented here. In all cases, a high-pressure gas mixture with high argon content (>90% molar fraction) is envisaged. A 96:4 Ar:CH$_4$ mixture was tested successfully during ND-GAr R&D [111, 112]. Therefore, non-Ar components in the ND-GAr target will contribute at the few percent level at most to the overall event rate in the TPC. In order to extract pure ν-Ar interactions, such percent-level corrections can be made with high accuracy using Transverse Kinematic Imbalance techniques [113], joint ND-GAr-SAND fits, and Monte Carlo-based estimates. High-pressure argon gas mixtures have been used in the past, such as in the PEP-4 detector at SLAC [114], which used a (flammable) gas mixture of 80:20 Ar:CH$_4$, operated at 8.5 atm. A known challenge for high-pressure gas detectors is that the gas amplification gain decreases as the gas pressure increases. For the DUNE ND-GAr, R&D to ensure adequate stability and gain in a non-flammable gas is underway.

Multi-Wire Proportional Chambers   To collect sufficient event statistics, the HPgTPC, at the core of ND-GAr, must be both large and capable of functioning under high pressures. A TPC of the size used in the ALICE experiment at CERN [115] may be adequate in terms of size, but only if the gas inside is pressurized to approximately 10 atm. As a result of the recent upgrade of ALICE's readout system to gaseous electron multipliers (s), the previously operated ALICE multi-wire proportional chambers have become available. They were previously operated in ALICE at 1 atm, hence their operation needed to be assessed within a high-pressure argon gas environment.

Two test stands, one each in the UK and the US, called the Gas-argon Operation of ALICE TPC (GOAT) and the Test stand of an Overpressure Argon Detector (TOAD), respectively, are
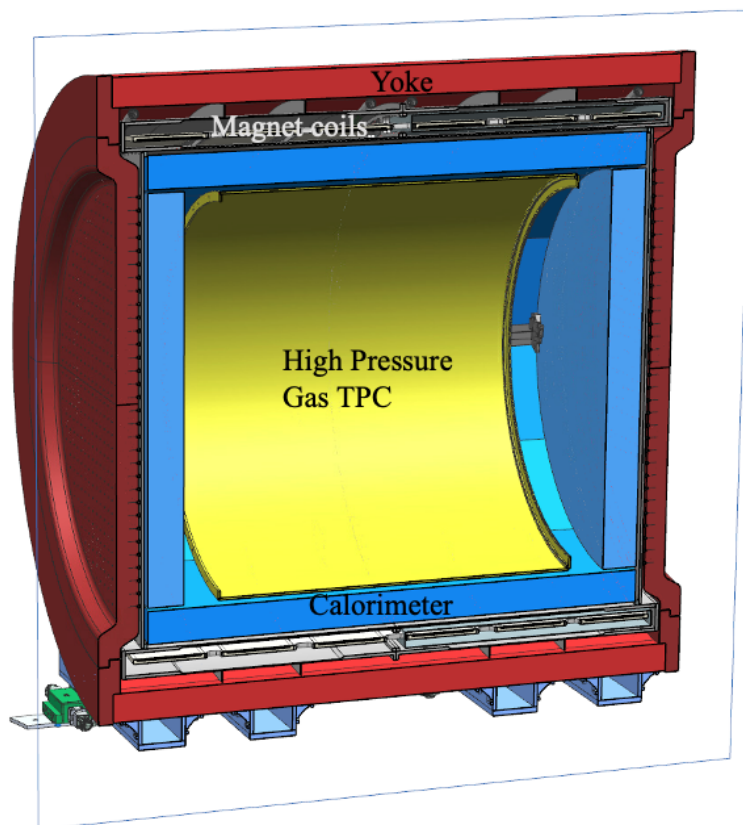
Figure 27: Cutaway view of the full ND-GAr detector system, showing the HPgTPC, the calorimeter, the magnet, and the iron yoke. The detectors for the muon-tagging system are not shown.

being used to test the ALICE chambers under high pressure. GOAT used a pressure vessel rated to 10 atm. It tested an ALICE inner chamber for its achievable gas gain at various pressure set points, amplification voltages, and gas mixtures [111]. TOAD had previously tested an ALICE outer chamber for its achievable gas gain up to 5 atm. Currently, it is being commissioned in the Fermilab for data-taking in a test beam and for performing a full detector slice test of the electronics and DAQ. In both test stands, wire-based readout chambers have been tested in high-pressure environments, demonstrating that they can provide reasonable gas gains when they operate at or above the high voltage values they were subject to in ALICE. Despite this, the long-term operation and stability of these chambers at such high voltages remain to be investigated. There are also plans to test charge readout systems based on micro-pattern gas detectors, such as GEMs, as described below.

TPC Readout with GEMs In a TPC using GEMs or "thick GEMs" (THGEMs), the ionization drift electrons enter the THGEM holes and are accelerated in a high electric field. At sufficiently high fields, this acceleration causes the electrons to further ionize the gas medium,

resulting in a Townsend avalanche. This exponentially increases the number of electrons and therefore the signal size.

Typically, GEMs and THGEMs are produced starting from double copper-clad substrates, either by photolithography of kapton in the case of the former, or Computer Numerical Control (CNC) drilling of epoxy laminates/FR-4 in the latter. We propose to use a new type of THGEM made out of glass, as also proposed in the context of the optical-based charge readout option for the Phase II FD (Section 3.3.4). These glass THGEMs developed at Liverpool (UK) are fabricated using a new masked abrasive machining process. The innovation allows for customization of glass THGEMs, where both substrate and electrode materials can be tailored to our requirements, which include high stiffness, low outgassing, and resilience to damage from discharges.

The amplified electrons from the THGEMs would be read out on a segmented anode to allow for tracking reconstruction. Borosilicate glass and fused silica are isotropic and homogeneous substrate materials that can be machined to typical THGEM thicknesses while remaining sturdy and potentially providing better surface finishes than FR-4-based THGEMs. Their transparency, made possible by indium tin oxide (ITO) electrodes, makes them suitable for optical imaging of primary ionization, as demonstrated up to 1.5 bar with cosmic ray imaging at estimated optical gains up to 10^6 [116].

Future optimization of glass GEMs may include enhancements in light collection with wavelength-shifting substrates [117], wavelength-shifting coatings [118], or diamond-like carbon (DLC) coatings for stability [119, 120]. R&D toward a THGEM-based readout is ongoing in Spain, where a 10-bar full 3D Optical TPC (Gaseous Argon T0 (GAT0)) is under commissioning. In addition, R&D toward a GEM-based readout for ND-GAr is currently underway in the US with the GEM Over-pressurized with Reference Gases (GORG) test stand, currently testing a triple-GEM stack.

TPC Readout electronics Due to the high-pressure nature of this detector, readout electronics must be developed that can operate inside the pressure vessel to minimize the analog signal path. The electronics must also be zero-suppressed and compatible with the existing DUNE DAQ infrastructure for the Phase I ND. Readout electronics has traditionally been one of the cost drivers of TPCs. While the pixel size to be used in the final detector module has not been determined, detectors like ALICE had 700k channels. With this number of channels, work is needed to ensure that the electronics system is cost-effective.

R&D work is underway in the UK and US to deliver such electronics. A prototype system using the SAMPA ASIC, developed for the ALICE TPC upgrade and the sPHENIX detector, plus FPGA-based control and aggregation, is already in hand. This solution, scaled up to the full ND-GAr detector, is expected to be much cheaper than the ones adopted for ALICE and sPHENIX, thanks to the much lower data rates. If full 3D optical tracking is ultimately adopted, the readout electronics would align with the technical proposal described in Section 3.3.4 for FD3 and FD4.
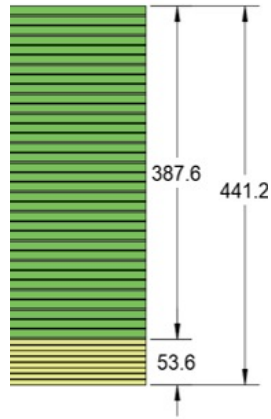
Figure 28: Possible structure of a combined tile and strip layer sampling calorimeter. The (yellow) tile/absorber layers are oriented towards the TPC; they are followed by (green) strip/absorber layers. Dimensions are in mm.

4.2.2 Calorimeter concept

The GArTPC will excel in measuring charged particle tracks, but to first order is blind to neutral particles. As such, it is important to have a system that can detect them. At neutrino energies of a few GeV, these are mostly photons (for example from π^0-decays) and neutrons (from nuclear break-up) in the kinetic energy range from $\lesssim 100\,\mathrm{MeV}$ to $\sim\mathrm{GeV}$. The photon energy will be determined calorimetrically, while the neutron energy can be determined by measuring the time of flight between the production vertex and a nuclear re-scatter in the calorimeter [121]. Both photons and neutrons will be key to measuring nuclear effects that will influence the relationship between true and reconstructed neutrino energy, and the dynamics of the neutrino interactions.

It is also the case that the HPgTPC should occupy the largest possible volume, and the calorimeter has to surround the TPC. As such, it has a rather large surface area even for modern particle physics detectors. Optimizing this detector to achieve the physics goals while still being affordable is a key task of the gaseous argon detector group.

A possible affordable technology with the required performance is based on a plastic scintillator sampling calorimeter that is constructed from active tile layers using a combination of the technology developed by the CALICE R&D Collaboration [122] and the more traditional scintillator strip, WLS fiber, and SiPM readout combination, used in neutrino experiments such as the near detector. A preliminary structure of the calorimeter is illustrated in Figure 27. Further details of the potential layout of the barrel detector are shown in Figure 28.

A potential barrel geometry consists of 60 layers with the following layout:

- eight inner layers of $2\,\mathrm{mm}$ copper + $5\,\mathrm{mm}$ of $2.5 \times 2.5\ \mathrm{cm}^2$ tiles + $1\,\mathrm{mm}$ FR-4, and

- 52 layers of $2\,\mathrm{mm}$ copper + $5\,\mathrm{mm}$ of cross-strips $4\,\mathrm{cm}$ wide

A possible barrel calorimeter depth is about $44\,\mathrm{cm}$. The initial performance evaluation for photons, based on a preliminary design that was investigated, is summarized in Figure 29.

72
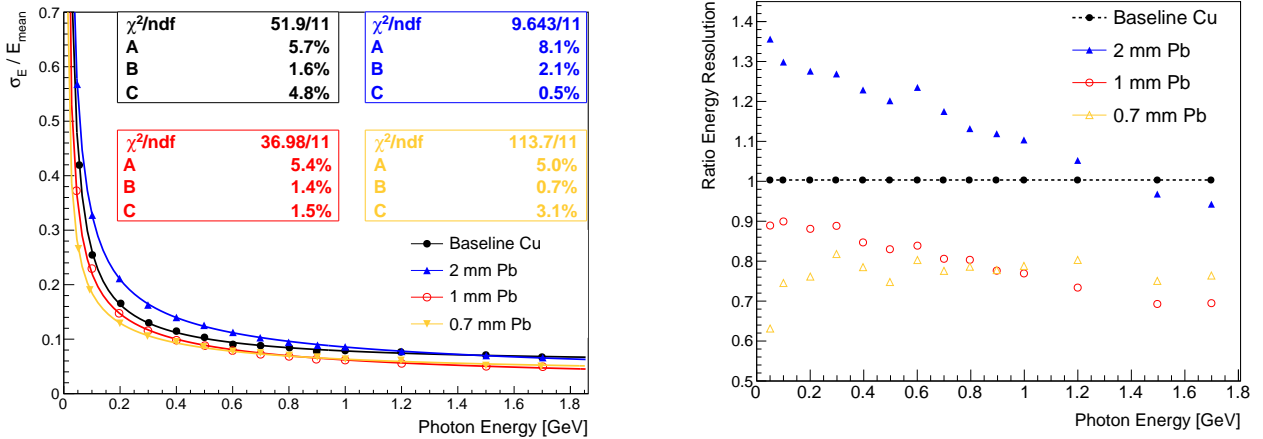
Figure 29: Left: energy resolution as a function of photon energy for different absorber configurations. The function $\frac{\sigma_E}{E} = \frac{A}{\sqrt{E}} \oplus \frac{B}{E} \oplus C$ has been fitted to the simulated data, where the $\oplus$ symbols refer to a quadrature sum of the three terms. Right: Ratio of the energy resolution for the different absorber configurations. The best resolution is achieved using thin lead absorber. The overall depth of the electromagnetic calorimeter (ECAL) has been kept constant. More details can be found in [5].

For the present study, copper has been chosen as the absorber material, as initial studies have shown that this material provides a good compromise between calorimeter compactness, energy, and angular resolution. It also allows for the removal of heat generated by the electronics in the tile layer. There are several possible readout ASICs on the market to determine the time and charge of the SiPM signals, one possibility being the KLauS ASIC [123].

4.2.3 Magnet concept

To achieve the physics goals, the TPC volume of the ND must be magnetized in order to measure the momenta of muons and other particles, and to determine the sign of their charge. The magnetized system will analyze both the tracks originating from ND-LAr and penetrating from upstream, and the tracks produced within the magnetic volume by neutrino interactions.

The need to make the magnet as compact as possible, thus minimizing the material at the downstream end of the TPC and in front of the calorimeter, suggests an integrated design in which the magnet structure serves also as a pressure vessel for the TPC gas volume. The magnetic design described in [124], and summarized here, fulfills these requirements and is cost-effective.

The magnet system consists of a superconducting solenoid surrounded by an iron return yoke. The superconducting solenoid cryostat serves not only as a pressure vessel body for the HPgTPC, but also as support for it and the calorimeter elements located in its bore. Additionally, the design of the iron magnet yoke uses the mechanical strength of the yoke's pole faces to eliminate the large domed heads that would normally be required for a large-diameter pressure vessel.

Another important design requirement for ND-GAr is the ability to accurately measure the momentum of muons that originate in ND-LAr. This requirement limits the amount of material allowed on the upstream side of ND-GAr and motivates an unconventional and asymmetrical iron yoke design. An iron yoke that eliminates a portion of the iron along the upstream face has been developed and designed, and is called Solenoid with Partial return Yoke (SPY). Figure 30 illustrates the SPY magnet system.
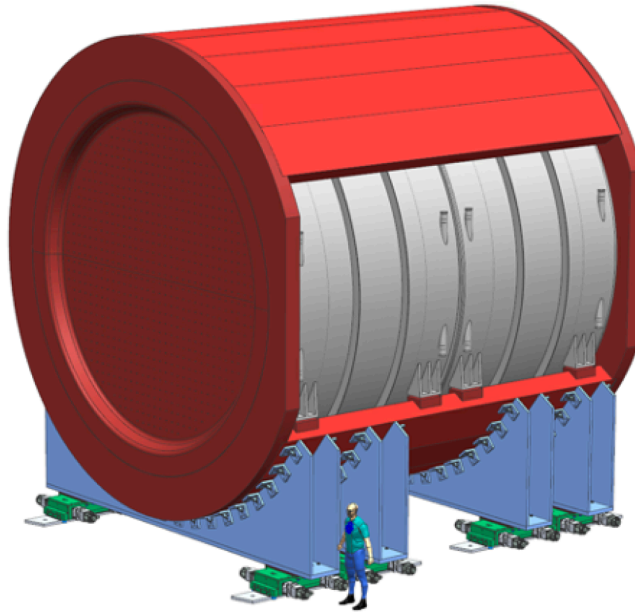
Figure 30: The SPY magnet system. The hole in the yokes is on the upstream side, to minimize material traversed by tracks originating from neutrino interactions in ND-LAr.

The following lists the main requirements and technological features of this design in more detail:

- The momentum analyzing power of the ND-GAr assembly (magnet + TPC) must provide at least 3% momentum resolution for the muons originating within ND-LAr. Additionally, for particles produced as a result of neutrino interactions in the HPgTPC, the resolution in neutrino energy reconstruction must be at least as good as that of the DUNE FD.

- The magnetic field uniformity, thanks to recent and relevant improvements in the capability of event reconstruction, is not required to be very high. A $\pm 10\%$ tolerance within the magnetic volume is expected to be sufficient, provided that a very accurate map for the magnet "as built" is measured. However, it is worth emphasizing that the magnet design fully described in [124] greatly exceeds the $\pm 10\%$ requirement, and should offer a $\pm 2\%$ variation over the whole volume. Careful studies were also done to evaluate and minimize the magnetic forces between ND-GAr and SAND.

- The superconductor will be co-extruded in high-purity aluminum to provide quench protection. The current reference solution for cable material is one based on niobium titanium. Higher temperature superconductors such as MgB_2 will also be considered as part of an R&D program currently in progress.

- The ND-GAr assembly must provide good acceptance for muons exiting ND-LAr and must fit within the space constraints imposed by the ND hall design and by DUNE-PRISM.

- The ND-GAr's magnet system must present as little material as possible in the path of the muons exiting from ND-LAr. A similar requirement holds in the downstream face of the yoke, to assist in the discrimination of muons from pions.

- The vacuum cryostat must be capable of providing mechanical support and a cryogenic environment for the superconducting coils. The inner wall of the vacuum cryostat must be sufficiently strong to serve as the outer wall of the pressure vessel for the HPgTPC, and to support the weight of the calorimeter.

- The carbon steel of the return yoke must provide a uniform $0.5\,\mathrm{T}$ magnetic field over the full length of the solenoid, and limit fringe fields to the $\leq 0.01\,\mathrm{T}$ levels required by the experiment and by the co-existence with SAND. It must also provide flat carbon steel pole tips for the magnet return yoke that match the magnetic field boundary conditions at the ends of the solenoid, and provide the mechanical support for the pressure vessel end flanges.

The main parameters achieved in the current design [124] are summarized in Table 5.

Parameter	Requirement	Notes
Central field	$0.5\,\mathrm{T}$	
Field uniformity	$\pm 10\%$	Current design achieves $\pm 2\%$
Ramp time to full field	$30\,\mathrm{min}$	
Stray field	$\leq 0.01\,\mathrm{T}$	Stray field in SAND negligible, in LAr fiducial volume (FV) $\simeq 10\,\mathrm{G}$
Bore diameter	$6.73\,\mathrm{m}$	Reduction possible with TPC and ECAL optimizations
Coils diameter	$7.85\,\mathrm{m}$	Cryostat diameter at stiffening rings
Solenoid length	$\simeq 7.8\,\mathrm{m}$	
Solenoid weight	$\simeq 150\,\mathrm{t}$	
Yoke total weight	$\simeq 757\,\mathrm{t}$	

Table 5: List of SPY parameters according to the current reference design.

4.2.4 Muon system

A GArTPC ND system will need to be outside the calorimeter to improve pion/muon separation. The muon tagger would likely implement a well established technology, such as a coarsely instrumented scintillator detector. It is not likely to require substantial R&D, but will need engineering effort.

4.2.5 Light detection options

Enabling time-tagging by the TPC would provide an absolute determination of the vertex position and interaction time, thus simplifying the matching with external detectors and enabling reconstruction of interactions whose by-products range out before reaching them. The only demonstrated technique to accomplish this in TPCs relates to primary scintillation, which due to the complexity of the system would require significant R&D, primarily to study the level of localization needed in order to associate time information with a given interaction. The choice of gas mixture for the detector will also be key, as different mixtures have very different scintillation properties [125, 126].

Although pure argon gas emits scintillation light copiously at a level of 20000 photons/MeV, gases employed historically in TPCs for accurate tracking in magnetic fields do not [127]. The recent demonstration of strong (and fast) wavelength shifting in the Ar/CF_4 system, with yields in the range 700–1400 photons/MeV [128, 129], opens up the possibility of ns-level time tagging for energy deposits down to at least 5 MeV [110]. A mere 1% CF_4 addition (per volume) seems sufficient to achieve this performance while keeping the electron diffusion at 3.6 mm for a 5 m drift (compared to 20 mm for pure argon) for a 200 kV cathode bias. These values are even below those expected for a conventional Ar/CH_4 (90/10) mixture.

In view of the requirements for single-photon detection and magnetic field compatibility, and given the spectral range of the scintillation, two technologies are of particular interest, as described below. A third, light readout of secondary scintillation at the amplification stage, is also an option that could be explored, based on an Ar/CH_4 (99/1) mixture (Section 4.2.1).

SiPMs SiPMs are well suited for detection in the visible range, and several ganging schemes are currently available for large area coverage (e.g., [130]). Silicon suffers from high dark rate at room temperature and, in fact, simulations point to the need for cryogenic operation (-25 C) to reach MeV-thresholds in ND-GAr. Methods to do this are under study. A comprehensive R&D program has been laid out and is led by Spain. A conceptual description of the ganging scheme and active-cryostat concept proposed, along with proof-of-principle demonstrations for both, can be found in [110].

LAPPDs Large-Area Picosecond Photo-Detectors (LAPPDs) are novel photosensors based on microchannel plate technology. With sensitive regions of order 20×20 cm and sub-cm position resolution, this type of detector is a good candidate for covering large areas. LAPPDs are tolerant of magnetic fields and handle sub-ns timing with an excellent signal-to-noise ratio, and without any cooling requirements. They were recently demonstrated to work for neutrino detection by the ANNIE experiment. Ideal coverage could be achieved with about 100

LAPPDs, which could be delivered within a few years at current production rates. Depending on the choice of quencher/wavelength shifter, modifying the photocathode composition or a wavelength shifter coating might be required.

Studies to optimize this system are required, and include determining optimal coverage, the best photocathode design, and enclosures to allow the LAPPDs to operate at high pressure.

4.2.6   R&D and engineering road map

R&D will be necessary for this Phase II improved tracker concept, starting in 2024 and lasting for several years. It will be important to fully define the detector requirements, then aim for a technical design report in the late 2020s, and be ready to begin construction in the early 2030s. The essential R&D and design work needed for ND-GAr includes, but is not limited to, the following items:

ND-GAr magnet   INFN Genova is pursuing R&D on using magnesium diboride (MgB_2) superconducting cables, which have a higher critical temperature and do not face some of the challenges of co-extruding NbTi superconducting cables with high-purity aluminum.

ND-GAr TPC charge readout and electronics test stands   Several R&D efforts are already underway, as described in Section 4.2.1. Examples include the GOAT, TOAD, GORG, and GAT0 test stands. Charge readout TPCs are a mature technology, with gas mixtures identified that give sufficient gain. The current R&D priority is to test the full readout chain, from amplification technology to readout electronics, in a high-pressure test stand, using a non-flammable gas with a high argon fraction, to ensure adequate stability and gain. Electron diffusion measurements will also be performed for the same gas mixtures.

Concerning the amplification stage, current testing has been done with wire chambers. However, modern TPCs such as those for ALICE and sPHENIX use GEMs to achieve better stability of operation and higher gains. For this reason, R&D for a GEM/THGEM-based amplification stage has started in the context of the DUNE Phase II ND, as well. The stability of proposed wavelength-shifting gases such as Ar/CF_4 (99/1) must be studied, as they are low-quenched. Conventional GEM, THGEM, glass-GEMs, glass-Micromegas and wire chamber amplification stages are all currently under evaluation in Spain, the UK, and the US.

Once detailed requirements on tracking performance are established, further R&D on readout electronics and on the segmentation of the charge readout pads/strips will be pursued accordingly. The TPC charge readout R&D work is currently ongoing in the UK (GEM work and readout electronics), Spain (glass-GEM, SiPMs + TPX3 cameras), and the US (readout electronics and test stands) using sources and test beams.

Light detection in ND-GAr TPC   The realization of light readout at the scale of the ND-GAr TPC poses important engineering challenges in relation to photosensor technology, HV integration, and good light collection. Dedicated physics studies are needed to establish the best design path towards the optimization of the detection thresholds, time-tagging performance, and photosensor coverage. Both light readout options discussed above have R&D needs, for

example cooling control for SiPMs and operation at high pressure for LAPPDs. Groups in Spain are performing R&D on the optimization of the SiPM-based optical readout concept: required coverage, use of reflectors and light collectors, SiPM channel ganging and cooling schemes. R&D on LAPPDs is also underway in the US.

Also, the outstanding tracking performance of ND-GAr needs to be guaranteed while ensuring that the photosensor plane not be blinded during the avalanche multiplication process in the anode region. This will require an additional R&D step targeting the minimization of photon-feedback, as it is customary for instance in ring-imaging Cherenkov detector applications [131].

ND-GAr calorimeter R&D was underway in Germany on coupling fibers to SiPMs to maximize light collection and uniformly illuminate the SiPM face. Studies must also be done to optimize the calorimeter design, including the number of strip and tile layers, and their granularity. A cost-effective readout electronics system must also be developed.

ND-GAr calibration systems, field cage, and gas systems Engineering work is also required to design the infrastructure and support services for the ND-GAr detector. The ALICE detector featured a high-performance TPC of similar size [115], therefore that design can potentially be used as a starting point. For example, a laser calibration system that can uniformly illuminate the drift volume could provide the required accurate monitoring of drift velocity variations and inhomogeneities within the volume. Such a system must be designed in close connection with the HV field cage. The movable ND-GAr will require design of a mechanically robust field cage with mechanical end-cap structures. A buffer region in between the field cage and pressure vessel will be needed to degrade the high voltage, and this may require the use of an additional insulating gas.

The detector performance depends crucially on the stability and quality of the gas in the drift region, therefore it will be necessary to develop a system to control and monitor the gas mixture in the drift volume. Control operations include pressurization, recirculation, purification, and evacuation of the gas. The current design of the magnet system does not incorporate a method for evacuation [132]. However, modifying it to function under both pressure and vacuum conditions is well understood. Generally, achieving vacuum is desirable to facilitate the reduction and monitoring of O_2 and H_2O impurities (as well as other unforeseen contaminants). It is also worth considering purifying argon gas in the gas handling system – which might yield similar results – although evacuation could potentially be faster.

4.3 Improvements to Phase I near detector components

As part of the Phase II program, possible enhancements and improvements to the exisiting Phase I components of the ND are being considered. This section discusses such possible improvements to the Phase I detector components ND-LAr and SAND.

4.3.1 Phase II ND-LAr detector

ND-LAr is the LAr component of the DUNE ND complex. With the intense neutrino flux and high event rate at the ND, traditional, monolithic, projective wire readout LArTPCs would be stretched beyond their performance limits. To overcome this hurdle, ND-LAr will be fabricated out of a matrix of smaller, optically isolated TPCs, read out individually via a pixelated readout. The subdivision of the volume into many smaller TPCs allows for shorter drift distances and times. This and the optical isolation lead to fewer problems with overlapping interactions.

The ND-LAr design consists of 35 optically separated LArTPC modules, which allows for independent identification of ν-Ar interactions in an intense beam environment using optical timing. Each TPC consists of a HV cathode, a low-profile field cage that minimizes the amount of inactive material between modules, a light collection system, and a pixel-based charge readout.

One key aspect of ND-LAr operation is the ability to cope with many neutrino interactions in each spill. The LBNF neutrino beam consists of a $10\,\mu$s wide spill, which leads to $\mathcal{O}(50)$ ν interactions per spill in Phase I and $\mathcal{O}(100)$ in Phase II. Given the relatively low expected cosmic ray rate while the beam is on (estimated to be $\sim$0.3/spill at $60\,$m depth), this beam-related pile-up is the primary challenge confronting the reconstruction of the ND-LAr events. The 3D pixel charge signal will be read out continuously. The slow drifting electrons (with charge from the cathode taking $\sim$300 μs to travel the 50 cm drift distance) will be read out with an arrival time accuracy of 200 ns and a corresponding charge amplitude within a $\sim$2 μs-wide bin. This coupled with the beam spill width gives a position accuracy of 16 mm. While this is already good spatial positioning, the ND-LAr light system will provide an even more accurate time tag of the charge as well as the ability to tag subclusters and spatially disassociated charge depositions resulting from neutral particles, such as neutrons, that come from the neutrino interaction. Thus, the ND-LAr light system has a different role from that in the FD, as it must time-tag charge signal subclusters to enable accurate association of all charge to the proper neutrino event, and to reject pile-up of charge from other neutrino signals.

The current ND-LAr design being implemented for Phase I satisfies the general requirements of DUNE for Phase II in terms of increased beam power and lifetime of detector components. Nonetheless, additional potential modifications to ND-LAr that might enhance its capabilities are under consideration. Given that the ND-LAr uptime during DUNE operations is an important factor to take into consideration, those modifications can be divided into two categories: ND-LAr upgrades that imply modifications to the inner detector hardware and thus require emptying the LAr, and those that do not. In the former, more disruptive, category, current ideas under exploration include: improvements to neutron detection methods by upgrading optical detectors with ^{6}Li-glass scintillator, replacement of charge tiles of a module with smaller pixels and lower threshold, use of photosensitive dopants, and use of radiopure underground argon. In the latter (less disruptive) category, possible upgrade options span the following: doping of argon with xenon, upgrade of the off-detector electronics, addition of a rock muon tracker in front of ND-LAr, and use of an additional calibration system based on ^{222}Rn injection. A decision on these possible ND-LAr upgrade paths will come after the Phase I ND-LAr detector is commissioned.

4.3.2 Phase II SAND detector

SAND is a multipurpose detector composed of a superconducting solenoid, a high-performance ECAL, a light tracker, and an active LAr target called . The magnet and the ECAL were part of the detector at INFN Frascati and will be refurbished for Phase I, without the need for upgrades during Phase II. The tracker, based on straw tubes, will be a completely new detector capable of reconstructing charged particle tracks in the magnetic field. Major upgrades for the tracker are not foreseen for Phase II.

GRAIN is an innovative LAr detector that will employ a completely new readout technique, using only scintillation light for track reconstruction. This task is accomplished by cameras with light sensors made of a matrix of SiPMs and optical elements, such as special lenses or Coded Aperture Masks. The GRAIN project is very challenging because, due to the low efficiency of light sensors to VUV scintillation light, the number of photons detected and used by the reconstruction algorithms is low.

For Phase II GRAIN, the goal is to enhance light collection by improving the SiPM PDE in the VUV range. For this purpose, we are developing with "Fondazione Bruno Kessler" (FBK-Trento) Backside Illuminated SiPMs (BSI SiPMs). In this architecture, the light entrance window is on the back of the silicon, while all the metallic contacts are on the front side. This will allow us to improve the fill factor and optimize the anti-reflective coating on the entrance window. It is planned to substitute all the GRAIN matrices of traditional Front Side SiPMs with the BSI ones for Phase II, if they will be available and mature in time.

4.4 Near-detector options for non-argon far detector modules

In the event that one of the Phase II FD modules consists of a neutrino target material that is not argon-based, such as the THEIA detector concept described in Section 3.5, the Phase II ND complex will need to provide measurements of neutrino interactions on those same target nuclei. Several options are under consideration for modifying the Phase I suite of ND sub-detectors to make such measurements, including modifying the Phase I SAND to incorporate oxygen and water targets, embedding liquid scintillator targets within the ECAL of the GArTPC, and constructing a new, dedicated, water-based near detector. While they introduce identical or similar nuclear targets, these particular options do not establish a functionally similar detector at the near site that would also mitigate detector-related uncertainties at the far detector, analogous to ND-LAr for the argon-based FD modules.

4.4.1 Oxygen and water targets in SAND

The SAND detector is equipped with a modular Straw Tube Tracker (STT) with target layers that are designed to be individually replaceable with different materials. A total of 78 thin planes, each about 1.6% of a radiation length X_0, of various passive materials are alternated and dispersed throughout active layers, which are made of four straw planes, to guarantee the same acceptance to final state particles produced in (anti)neutrino interactions. The STT allows minimizing the thickness of individual active layers and to approximate the ideal case of a pure target detector – the targets constitute about 97% of the mass – while keeping the total thickness

of the stack comparable to one radiation length and an average density of about $0.17\,\mathrm{g/cm^3}$. The lightness of the tracking straws and the chemical purity of the targets, together with the physical spacing among the individual target planes, make the vertex resolution ($\ll 1\,\mathrm{mm}$) less critical in associating the interactions to the correct target material. The average momentum resolution expected for muons is $\delta p/p \sim 3.5\%$ and the average angular resolution better than $2\,\mathrm{mrad}$. The momentum scale can be calibrated to about 0.2% using reconstructed $K_0 \to \pi^+\pi^-$ decays.

The STT is optimized for the "solid" hydrogen technique, in which $\nu(\bar{\nu})$ interactions on free protons are obtained by subtracting measurements on dedicated graphite (C) targets from those on polypropylene (CH_2) targets [133, 134, 135]. The default target configuration in Phase I includes 70 CH_2 targets and eight C targets. The use of a distributed target mass within a low-density tracker results in an approximately uniform acceptance over the full 4π angle, as shown in Figure 31. The acceptance disparity between different targets can be kept within 10^{-3} for all particles (Figure 31) due to their thinness and their alternation throughout the detector volume. The subtraction procedure between different materials can then be considered model-independent within these uncertainties. Furthermore, the detector acceptance effectively cancels in comparisons between the selected interactions on different target nuclei.
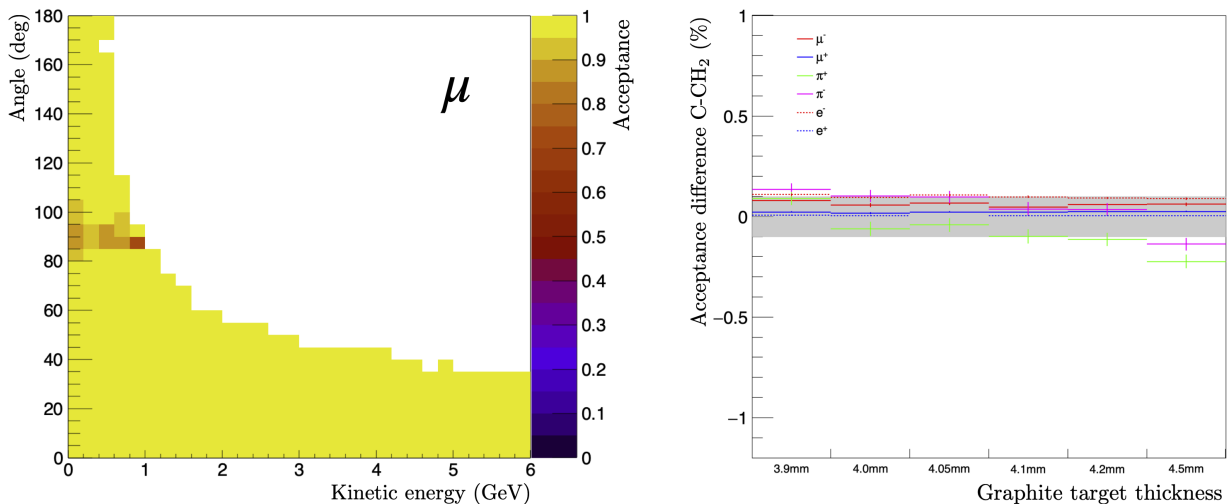
Figure 31: Left: Muon acceptance for ν_μ CC interactions in a forward horn current () beam in SAND. Right: Discrepancy in acceptance between the CH_2 and C targets in SAND.

The ND can operate with both oxygen and water targets concurrently by replacing some of the initial CH_2 targets with polyoxymethylene (CH_2O, acetal) planes with equivalent thickness, i.e., in terms of radiation length and nuclear interaction length λ_I. Interactions on oxygen are obtained from a subtraction between CH_2O and CH_2 targets, while interactions on water are obtained from a subtraction between CH_2O and C targets [136].

To this end, 4.5 mm thick acetal slabs can be used, corresponding to about $0.016\,X_0$ and $0.008\,\lambda_I$. The oxygen content by mass within acetal dominates at 53.3%. By replacing only 20 polypropylene targets (out of 70) with the equivalent CH_2O targets, we obtain an oxygen target mass of about 760 kg and a water target mass of about 850 kg. Assuming an exposure of

3×10^{21} POT, corresponding to about two years with the Phase I beam intensity and to about one year with the Phase II beam, we expect to collect 3×10^6 ν_μ CC events with the FHC beam and 1×10^6 $\bar{\nu}_\mu$ CC events with the beam on oxygen. The subtraction procedure introduces an increase of about 40% in the statistical uncertainties with respect to the use of ideal targets. For 3×10^{21} POT, the resulting statistical bin-to-bin uncertainties in the ν-nucleus cross-sections as a function of neutrino energy are comparable to the expected systematic uncertainties introduced by the STT momentum scale uncertainty of 0.2% [136].

4.4.2 Liquid scintillator targets in the ND-GAr calorimeter

The GArTPC described in Section 4.2 is capable of supporting active THEIA-type targets within the downstream portion of the upstream ECAL, as shown in Figure 32. The THEIA layers consist of X and Y bars (similar to the NOvA configuration discussed in the next section), and interactions in these layers produce particles that enter the high-pressure gas TPC where they are precisely tracked. Neutral particles are measured by the surrounding ECAL, and the active THEIA layers provide an additional measure of low-energy particles near the interaction vertex ("vertex activity"). For neutrino interactions within the GArTPC, the THEIA layers will form an initial low-density section of the ECAL that can provide fast timing for particles exiting the TPC.
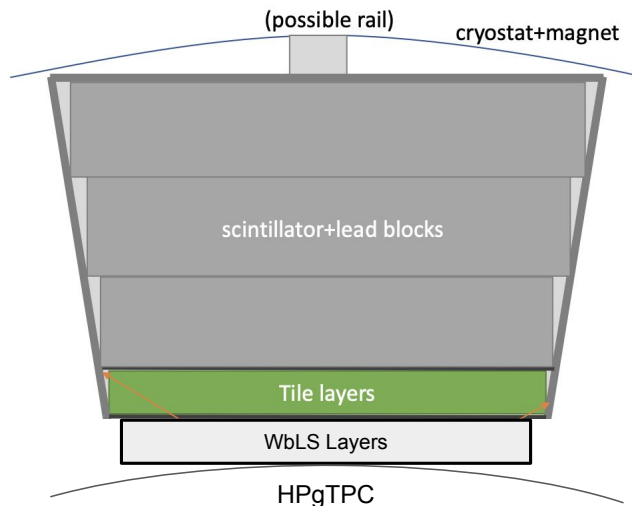
Figure 32: An upstream segment of the GArTPC ECAL, with the beam is pointing downward. The THEIA layers constitute the most downstream portion of the ECAL, and particles produced in these layers via neutrino interactions are tracked in the downstream HPgTPC.

There is sufficient space within the ECAL to include THEIA layers with a thickness of at least 10 cm, which would provide more than a ton of target mass. This would produce $\mathcal{O}(1M)$ charged current ν_μ interactions in a 14 week run on-axis, and $\mathcal{O}(10k)$ charged current ν_μ interactions in a two week run at the furthest off-axis position, both of which would be expected to occur within a nominal DUNE yearly run.

4.4.3   Water-based near detector

It is possible to install a detector specifically designed to make measurements for a water-based FD module in the DUNE ND hall. If a new GArTPC is built, it will serve as the downstream spectrometer for ND-LAr, allowing TMS to be used as a downstream spectrometer for a dedicated Water-based Near Detector (WbND). Any configuration of the ND suite will be subject to the space limitations imposed by the near site infrastructure, as completed before the beginning of beam operations. Two possible options for a WbND are a NOvA-style ND, or a LiquidO ND, both discussed below.

twice as long as the extrusion and looped at the "far end" of the cell (Fig. 1). Generally, the scintillation light is captured by the WLS fiber after several reflections off the cell walls. Simulations show that scintillation light reflects about 8 times on average before entering the fiber. This is the key reason to use highly-reflective PVC surfaces. The Far Detector has a total of 344,064 PVC cells, individually equipped with optical fibers to transport scintillation light to a 32-channel avalanche photodiode (APD) for readout [137]. that sits just over an optical connector attached to each 32 cell module.

NOvA-style near detector   The NOvA ND consists of individual cells, as shown in Figure 33, arranged in horizontal and vertical layers. The cells consist of PVC extrusions filled with liquid scintillator, and a wavelength-shifting fiber collects the light and guides it to the avalanche photodiode (APD) for readout [137].

Figure 33: The fundamental unit cell of the detector of the NOvA near detector; the cells are arranged in horizontal and vertical layers.
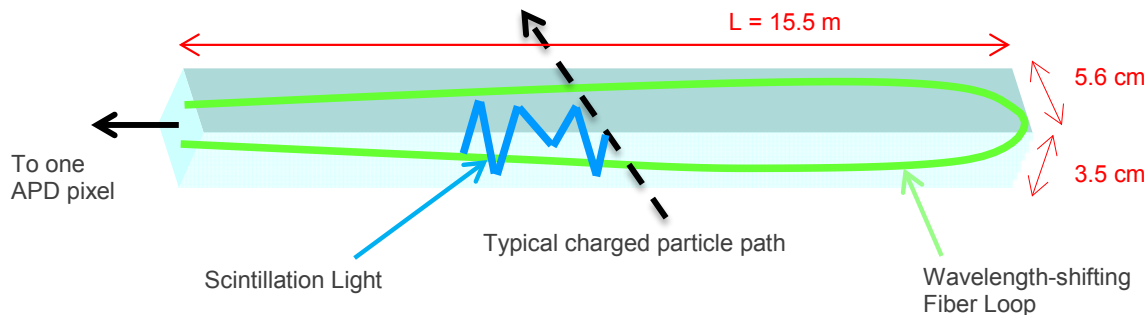
Figure 1: Ionizing particles passing through the scintillating liquid contained within an extrusion cell produce light, which reflects off the PVC walls multiple times until being captured by a wavelength shifting fiber optic loop. Light within the fiber optic travels the length of the extrusion and is detected by an avalanche photodiode (APD). Dimensions refer to *liquid* volume.

The NOvA near detector design could be used to construct a WbND by replacing the NOvA scintillator with TʜᴇɪᴀWbLS. Its cell size and scintillator fraction would have to be tuned to ensure a high muon reconstruction efficiency. This type of detector would also be capable of a calorimetric measurement of the hadronic energy in the neutrino final state, including better sensitivity to neutrons than a LAr detector, due to the presence of free hydrogen in the target material. This detector technology is well established and would require minimal additional R&D.

Detector Structure

The extrusions form the mechanical backbone of the NOvA detectors, providing the strength necessary to maintain a very large structure filled with liquid scintillator. In order to capture the scintillation light for readout, the extrusion cell walls must have a high reflectance, significantly higher than found in commercial PVC products. We have developed a PVC-based formulation to achieve high reflectance while maintaining the necessary mechanical strength. This paper describes the techniques developed to produce more than 11 million pounds of NOvA extrusions that meet strict reflectance, strength and dimensional requirements. An extrusion profile schematic is shown in Fig. 2, and a photograph in Fig. 3a.

LiquidO near detector   A promising new detector concept for the DUNE ND is based on using opaque scintillators with millimeter-scale scattering length to produce high-resolution images of neutrino interactions [138, 139]. The scintillation photons are stochastically confined close to the point of production via scattering, and a lattice of wavelength-shifting fibers at $\simeq 1$ cm pitch is used to extract the light. This technology, called LiquidO, removes the need for manual segmentation: the lattice of fibers is constructed first, and then the opaque scintillator poured in around the fibers. Substantially better spatial resolution per readout channel is achieved by using the profile of the light detected across multiple fibers. Figure 34 shows a CC
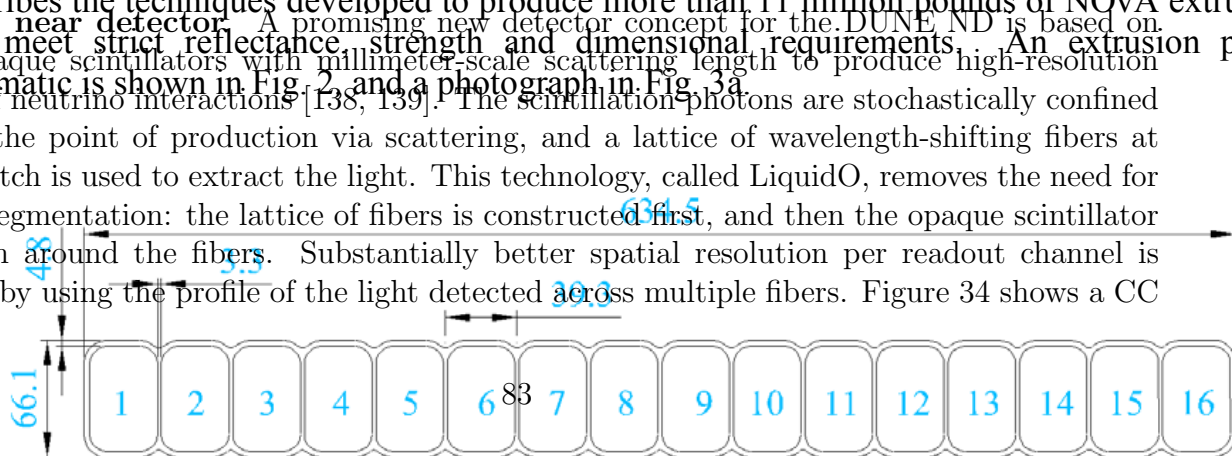
Figure 2: NOvA extrusion cross section with cells numbered 1 through 16 (dimensions are in millimeters).

The Near and Far Detectors consist of free-standing blocks of PVC extrusions, filled with liquid scintillator. The NOvA Far Detector is at this time potentially the largest self-supporting plastic

muon neutrino event as imaged with a LiquidO technology ND. Furthermore, and importantly for a potential THEIA DUNE Phase II FD module, the scintillator isotopic composition can be varied by exchanging the scintillator material, e.g., oil-based scintillators can be swapped with water-based ones. A design analogous to the T2K Super-FGD detector is envisaged for DUNE with the fibers running in all three perpendicular directions, allowing fine-grained precision tracking and excellent calorimetry. The hydrogen-rich nature of organic or water-based scintillators, together with their fast timing, is advantageous for neutron time-of-flight measurements and for particle detection in high-rate environments.
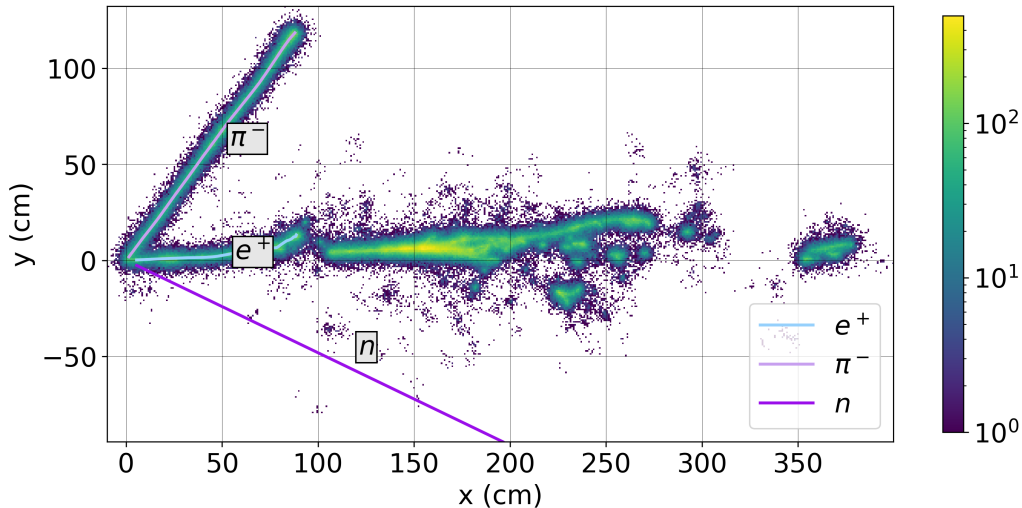
Figure 34: Illustration of a simulated $2\,\mathrm{GeV}$ electron neutrino interaction in a LiquidO-style ND with a 1 cm fiber pitch. The image shows sub-cm spatial resolution and excellent particle ID can be achieved.

Acknowledgements

Glossary

Eos The XRootD-based distributed file system developed by CERN. 56, 61

Theia-25 A 25 kt version of the THEIA detector concept that could serve as DUNE's fourth far detector module.. 54, 55

Theia Proposed hybrid detector with both Cherenkov and scintillation detection capabilities. 16, 19, 24–26, 53–58, 60, 61, 63, 64, 66, 79, 81, 82

neutrinoless double-β decay ($0\nu\beta\beta$) A hypothetical nuclear transition in which a nucleus with with Z protons decays into a nucleus with Z+2 protons and the same mass number, together with the emission of two electrons and no neutrinos.. 25, 51, 52, 55, 56, 59

ACE-MIRT The Accelerator Complex Evolution with Main Injector Ramp and Target upgrade is a proposed set of major upgrades to the Fermilab accelerator complex aimed at an early implementation of an enhanced 2.1 MW beam for DUNE.. 15, 17, 28

Artificial Intelligence (AI) A field of study in computer science which develops and studies intelligent machines.. 63

Axion-like particle (ALP) A hypothetical pseudoscalar particle that appears in the spontaneous breaking of a global symmetry.. 26

anode plane a planar array of charge readout devices covering an entire face of a detector module. 32

APEX Aluminum Profiles with Embedded X-arapuca. 34–39, 61, 62, 64

ARIADNE Charge readout technology for LArTPC dual-phase detectors based on gaseous electron multipliers and fast optical cameras.. 39, 45–47, 60–64

Amorphous selenium (aSe) A type of photoconductive material.. 50, 61

ASIC application-specific integrated circuit. 40–42, 49, 61, 62, 70, 71

BDE bottom detector electronics. 31, 40

boosted decision tree (BDT) A method of multivariate analysis. 19

Brookhaven National Laboratory (BNL) US national laboratory in Upton, NY. 56

BSM beyond the Standard Model. 12, 14, 16, 18, 20, 26–29, 51, 53, 68

charged current (CC) Refers to an interaction between elementary particles where a charged weak force carrier (W^+ or W^-) is exchanged. 20, 24, 27, 28, 57, 67, 80, 82

core-collapse supernova (CCSN) The collapse of stars more than $8\times$ as massive as the sun which produces an intense burst of neutrinos at the end of its fusion cycle in a matter of seconds which ejects the outermost stellar gas leaving behind a neutron star remnant.. 21, 22

cold electronics (CE) Analog and digital readout electronics that operate at cryogenic temperatures. 31

Coherent Elastic Neutrino-Nucleus Scattering (CEνNS) A type of neutrino interaction with matter.. 24

European Laboratory for Particle Physics (CERN) The leading particle physics laboratory in Europe and home to the ProtoDUNEs and other prototypes and demonstrators, including the s. 13–15, 39, 42, 61

CMOS Complementary metal-oxide-semiconductor. 43

Computer Numerical Control (CNC) A precise drilling method that utilizes a rotating cutting tool to produce round holes in a stationary work piece. 69

carbon nitrogen oxygen (CNO) The CNO cycle (for carbon-nitrogen-oxygen) is one of the two known sets of fusion reactions by which stars convert hydrogen to helium, the other being the proton-proton chain reaction (pp-chain reaction). In the CNO cycle, four protons fuse, using carbon, nitrogen, and oxygen isotopes as catalysts, to produce one alpha particle, two positrons and two electron neutrinos. 25, 54, 56, 59

ColdADC A newly developed 16-channels ASIC providing analog to digital conversion. 40

COLDATA A 64-channel control and communications ASIC. 40

commercial off-the-shelf (COTS) Items, typically hardware such as computers, that may be purchased whole, without any custom design or fabrication and thus at normal consumer prices and availability. 45

charge conjugation and parity (CP) Product of charge conjugation and parity transformations. 54

Coordinating Panel for Advanced Detectors (CPAD) US panel that seeks to promote, coordinate and assist in the research and development of instrumentation and detectors for high-energy physics experiments.. 13, 16

charge, parity, and time reversal symmetry (CPT) product of charge, parity and time-reversal transformations. 18

Charge Conjugation-Parity Symmetry Violation (CPV) Lack of symmetry in a system before and after charge conjugation and parity transformations are applied. For CP symmetry to hold, a particle turns into its corresponding antiparticle under a charge

transformation, and a parity transformation inverts its space coordinates, i.e. produces the mirror image. 12–14, 17, 18, 28, 53

charge readout (CRO) The system for detecting ionization charge distributions in a detector module. 31

charge-readout plane (CRP) An anode technology using a stack of perforated PCBs with etched electrode strips to provide CRO in 3D; it has two induction layers and one collection layer; it is used in the SP vertical drift FD and DP designs. 29, 31, 32, 34, 35, 39, 40, 59, 61, 62, 64

charge-readout unit (CRU) In the SP vertical drift design an assembly of the s plus adapter boards; two to a CRP. 31

data acquisition (DAQ) The data acquisition system accepts data from the detector front-end (FE) electronics, buffers the data, performs a , builds events from the selected data and delivers the result to the offline . 37, 63, 69, 70

dichroic filter (DF) Optical filter that reflects some wavelengths of light and transmits others, with almost no absorption for all wavelengths of interest. 37, 38

dual-phase (DP) Distinguishes a LArTPC technology by the fact that it operates using argon in both gas and liquid phases; sometimes called double-phase. 56, 64

DRD ECFA Detector R&D. 16

diffuse supernova neutrino background (DSNB) The term describing the pervasive, constant flux of neutrinos due to all past supernova neutrino bursts. 23

Deep Underground Neutrino Experiment (DUNE) A leading-edge, international experiment for neutrino science and proton decay studies; refers to the entire international experiment and collaboration. 12, 14

DUNE Precision Reaction-Independent Spectrum Measurement (DUNE-PRISM) a mobile near detector that can perform measurements over a range of angles off-axis from the neutrino beam direction in order to sample many different neutrino energy distributions. 14, 15, 64, 68, 73

electromagnetic calorimeter (ECAL) A detector component that measures energy deposition of traversing particles (in the DUNE near detector design). 72, 74, 78, 79, 81

European Committee for Future Accelerators (ECFA) Committee charged with the long-range planning of European high-energy facilities: accelerators, large-scale facilities and equipment.. 13, 16

far detector (FD) The 70 kt total (40 kt fiducial) mass LArTPC DUNE detector, composed of four 17.5 kt total (10 kt fiducial) mass modules, to be installed at the far site at SURF in Lead, SD, USA. 12, 13, 15–22, 24–26, 28, 29, 42, 46, 50, 51, 56, 62–64, 66, 69, 73, 78, 79, 81, 82

far detector module 1 (FD1) The first DUNE far detector module to be built at SURF. 15, 19, 29, 31, 37, 43, 48, 49, 62

far detector module 2 (FD2) The second DUNE far detector module to be built at SURF. 13, 15, 16, 19, 29–32, 34, 35, 37, 39, 42, 43, 49, 52, 56, 60, 62–64

far detector module 3 (FD3) The third DUNE far detector module to be built at SURF. 15–17, 19, 20, 39, 60, 62, 63, 70

far detector module 4 (FD4) The fourth DUNE far detector module to be built at SURF. 15–17, 19, 20, 60, 62, 63, 70

FDR Depending on context, either "final design report," a formal project document that describes the experiment at a final level, or "final design review," a formal review of the final design of the experiment or of a component. 64

Fermi National Accelerator Laboratory (Fermilab) U.S. national laboratory in Batavia, IL. It is the laboratory that hosts LBNF and DUNE, and serves as the experiment's near site. 12, 14, 56, 61, 69

FHC forward horn current (ν_μ mode). 80

field cage The component of a LArTPC that contains and shapes the applied E field. 13, 29–32, 34, 35, 37–39, 54, 61, 62, 77

field programmable gate array (FPGA) An integrated circuit technology that allows the hardware to be reconfigured to execute different algorithms after its manufacture and deployment. 41, 45, 70

FRP fiber-reinforced plastic. 32

FTBF Fermilab Test Beam Facility. 69

fiducial volume (FV) The detector volume within the TPC that is selected for physics analysis through cuts on reconstructed event position. 74

gaseous argon time-projection chamber (GArTPC) A TPC filled with gaseous argon. 13, 66, 67, 70, 74, 79, 81

Gaseous Argon T0 (GAT0) An Optical TPC demonstrator in Spain. A test stand for ND-GAr R&D. 70, 76

Geant4 A software toolkit for the simulation of the passage of particles through matter using Monte Carlo (MC) methods. 38

GEM Gaseous electron multiplier. 69, 70, 76

Gas-argon Operation of ALICE TPC (GOAT) A test stand for ND-GAr R&D.. 69, 76

GEM Over-pressurized with Reference Gases (GORG) A test stand for ND-GAr R&D. 70, 76

GRAIN In the SAND detector, a small cryostat containing LAr installed upstream of the straw-tube tracker inside the ECAL. 78, 79

HNL heavy neutral lepton. 26–28

horizontal drift single-phase, horizontal drift LArTPC technology. 29, 31

high-pressure gaseous argon TPC (HPgTPC) A TPC filled with gaseous argon; a possible component of the DUNE ND. 15, 16, 27, 68, 69, 71–74, 81

high voltage (HV) Generally describes a voltage applied to drive the motion of free electrons through some media, e.g., LAr. 32, 35, 63, 64, 76, 77

HVFT HV feedthrough. 32

HVPS HV power supply. 32

high voltage system (HVS) The detector subsystem that provides the TPC drift field. 32, 34

ICARUS A neutrino experiment that was located at the Laboratori Nazionali del Gran Sasso (LNGS) in Italy, then refurbished at CERN for re-use in the same neutrino beam from Fermilab used by the , MicroBooNE and SBND experiments at Fermilab. 15, 29, 52

KLOE KLOE is a e^+e^- collider detector spectrometer operated at DAFNE, the ϕ-meson factory at Frascati, Rome. In DUNE it will consist of a 26 cm Pb+scintillating fiber ECAL surrounding a cylindrical open detector region that is 4.00 m in diameter and 4.30 m long. The ECAL and detector region are embedded in a 0.6 T magnetic field created by a 4.86 m diameter superconducting coil and a 475 tonne iron yoke. 78

Large Area Picosecond Photo-Detector (LAPPD) A kind of imaging photodetector designed to provide exquisite time resolution.. 56, 75, 76

liquid argon (LAr) Argon in its liquid phase; it is a cryogenic liquid with a boiling point of 87 K and density of 1.4 g/ml. 12–17, 19, 20, 29, 35, 37–40, 45–48, 50–53, 55, 57, 60, 62–65, 74, 77, 78, 82

LArASIC A 16-channel FE ASIC that provides signal amplification and pulse shaping. 40

LArIAT The repurposed ArgoNeuT LArTPC, modified for use in a charged particle beam, dedicated to the calibration and precise characterization of the output response of these detectors. 53

LArPix ASIC pixelated charge readout for a TPC. 40–43, 49, 60–62, 64

liquid-argon time-projection chamber (LArTPC) A TPC filled with liquid argon; the basis for the DUNE FD modules. 13, 15, 19–21, 23–25, 35, 40–43, 45, 48, 49, 51–53, 62–64, 66, 67, 77

long-baseline (LBL) Refers to the distance between the neutrino source and the FD. It can also refer to the distance between the near and far detectors. The "long" designation is an approximate and relative distinction. For DUNE, this distance (between Fermilab and SURF) is approximately 1300 km. 18

Long-Baseline Neutrino Facility (LBNF) Long-Baseline Neutrino Facility; refers to the facilities that support the experiment including in-kind contributions under the line-item project. The portion of LBNF/DUNE-US responsible for developing the neutrino beam, the far site cryostats, and far and near site cryogenics systems, and the conventional facilities, including the excavations. 12, 14, 15, 26, 28, 78

LBNF/DUNE Construction Project The international project to design and build the facilities and detectors for the LBNF and DUNE enterprise (LBNF/DUNE); it includes the LBNF/DUNE-US and projects at multiple international partners to manage the contributions from non-US institutions and funding agencies to design, build, and install the detector components. 14, 28

LBNF/DUNE-US Long-Baseline Neutrino Facility/Deep Underground Neutrino Experiment - United States; project to design and build the conventional and beamline facilities and the contributions to the detectors. It is organized as a DOE/Fermilab project and incorporates contributions to the facilities from international partners. It also acts as host for the installation and integration of the DUNE detectors. 14

Lawrence Berkeley National Laboratory (LBNL) US national laboratory in Berkeley, CA. 56

light yield detected photons per unit deposited energy. 38, 39

LightPix Low-power, cryogenic-compatible and scalable SiPM readout electronics based on the LArPix ASIC. 47, 49, 61–63

MCND More Capable Near Detector. 15, 20

MicroBooNE A LArTPC neutrino oscillation experiment at Fermilab. 15, 29

Metal–oxide–semiconductor field-effect transistor (MOSFET) A type of field-effect transistor. 42

Mikheyev-Smirnov-Wolfenstein effect (MSW) Explains the oscillatory behavior of neutrinos produced inside the sun as they traverse the solar matter. 25, 54

neutral current (NC) Refers to an interaction between elementary particles where a neutrally charged weak force carrier (Z^0) is exchanged. 24

near detector (ND) Refers to the collection of DUNE detector components installed close to the neutrino source at Fermilab; also a subproject of LBNF/DUNE-US that includes installation, infrastructure, and the cryogenics systems for this detector. 12, 13, 15, 17–20, 26, 27, 29, 41–43, 64–66, 70, 72–74, 76, 77, 79, 81–83

ND-GAr component of the near detector with a core gaseous argon TPC surrounded by an ECAL and a magnet. 15, 26–28, 67–70, 72–77

ND-LAr LArTPC component of the near detector based on technology. 13–16, 20, 28, 40, 64–68, 72–74, 77–79, 81

NP02 The CERN North Area in Experiment Hall North One (EHN1) intersected by the hadron beamline, the location of the 800 t cryostat used for ProtoDUNE-DP and for SP vertical drift tests and prototypes; also used to refer to the 800 t cryostat in this area. 47

PCB printed circuit board. 13, 30–32, 38, 39, 41, 42, 48, 50, 61, 62

photon detector (PD) The detector elements involved in measurement of the number and arrival times of optical photons produced in a detector module. 34–39, 61, 62

PDE photon detection efficiency. 38, 48, 79

photon detection system (PDS) The detector subsystem sensitive to light produced in the LAr. 24, 32, 34, 37–39, 49, 62, 68

photoelectron (PE) An electron ejected from the surface of a material by the photoelectric effect. 38

PEEK Polyether ether ketone, a colorless organic thermoplastic polymer. 39

particle ID (PID) Particle identification. 13, 53, 54, 65, 66

Proton Improvement Plan II (PIP-II) A Fermilab project for improving the protons on target delivered delivered by the LBNF neutrino production beam. This is version two of this plan and it is planned to be followed by a PIP-III. 15

power-over-fiber (PoF) a technology in which a fiber optic cable carries optical power, which is used as an energy source rather than, or as well as, carrying data; this allows a device to be remotely powered, while providing electrical isolation between the device and the power supply. 34, 35, 37, 39, 62

protons on target (POT) Typically used as a unit of normalization for the number of protons striking the neutrino production target. 17, 27, 80

parts per million (ppm) A concentration equal to one part in 10^6. 51–53, 62

ProtoDUNE Either of the two initial DUNE prototype detectors constructed at CERN. One prototype implemented SP technology and the other DP. 39

ProtoDUNE-DP The DP ProtoDUNE detector constructed at CERN in NP02. 29

ProtoDUNE-SP The horizontal drift detector module (FD1-HD) ProtoDUNE detector constructed at CERN in . 15, 29, 51

ProtoDUNE-VD ProtoDUNE with vertical drift technology. This refers to the CRP-based prototype to run in NP02 (in the phase). 15, 29, 39, 61, 63

Q-Pix A pixel-based, 3D, readout technology based on a continuously integrating low-power charge-sensitive amplifier viewed by a Schmitt trigger. 40, 42–45, 49, 61, 62, 64

Q-Pix Light Imaging in Liquid Argon (Q-Pix-LILAr) A Q-Pix pixel coated with a type of photoconductive material, to perform integrated charge/light readout on the anode.. 47, 49, 50, 61–63

quality assurance (QA) The process of ensuring that the quality of each element meets requirements during design and development, and to detect and correct poor results prior to production. 31

quality control (QC) The process (e.g., inspection, testing, measurements) of ensuring that each manufactured element meets its quality requirements prior to assembly or installation. 31

RDC Detector R&D collaborations. 16

RHC reverse horn current ($\overline{\nu_\mu} \rightarrow \overline{\nu_\mu}$ mode). 80

System for on-Axis Neutrino Detection (SAND) The beam monitor component of the near detector that remains on-axis at all times and serves as a dedicated neutrino spectrum monitor. 14–16, 64–66, 69, 73, 74, 77–80

SBND The Short-Baseline Near Detector experiment at Fermilab. 15

signal feedthrough chimney (SFT chimney) A volume above the cryostat penetration used for a signal feedthrough. 31

silicon photomultiplier (SiPM) A solid-state avalanche photodiode sensitive to single photoelectron signals. 23, 25, 34–36, 38, 48, 49, 58, 59, 61, 62, 71, 75–77, 79

Sanford Underground Low background Module (SLoMo) A dedicated low background far detector module that would enhance the physics program of DUNE.. 58, 59

Standard Model (SM) Refers to a theory describing the interaction of elementary particles. 27

supernova neutrino burst (SNB) A prompt increase in the flux of low-energy neutrinos emitted in the first few seconds of a CCSN. It can also refer to a trigger command type that may be due to this phenomenon, or detector conditions that mimic its interaction signature. 12, 14, 20–24, 29, 45, 51, 54, 56, 57

SuperNova Early Warning System (SNEWS) A global supernova neutrino burst trigger formed by a coincidence of SNB triggers collected from participating experiments. 22

signal-over-fiber (SoF) a technology in which a fiber optic cable carries detector output that has been converted from an electrical to an optical pulse. 34, 35, 37, 39, 62

Solar neutrinos in Liquid Argon (SoLAr) A new concept for a liquid-argon neutrino detector technology to extend the sensitivities of these devices to the MeV energy range. 47–49, 61–64

single-phase (SP) Distinguishes a LArTPC technology by the fact that it operates using argon in its liquid phase only; a legacy DUNE term now replaced by horizontal drift and vertical drift. 29

Solenoid with Partial return Yoke (SPY) Magnet concept currently envisaged to magnetize ND-GAr.. 72–74

Straw Tube Tracker (STT) Target/tracker system that is part of the SAND near detector.. 79, 80

Sanford Underground Research Facility (SURF) SURF is an underground laboratory in Lead, South Dakota, where the DUNE FD will be installed and operated. It is the deepest underground laboratory in the United States.. 12, 39, 57

T2K T2K (Tokai to Kamioka) is a long-baseline neutrino experiment in Japan studying neutrino oscillations. 71, 82

TDE top detector electronics. 31

Thick GEM (THGEM) High-gain gaseous electron multiplier. 45, 46, 61, 69, 70, 76

Tetra-methyl-germanium (TMG) A photosensitive hydrocarbon capable of converting VUV scintillation light into ionization charge in a LAr detector.. 52

Muon Spectrometer (TMS) A muon spectrometer for the Near Detector that will be installed for the initial running period of DUNE, before the multi-purpose detector (MPD) detector component is ready. 13, 15, 16, 20, 28, 64–66, 81

Test stand of an Overpressure Argon Detector (TOAD) A test of a high-pressure gaseous argon TPC in the Fermilab Test Beam Facility FTBF. 69, 76

tetra-phenyl butadiene (TPB) A WLS material. 45

time projection chamber (TPC) Depending on context: (1) A type of particle detector that uses an E field together with a sensitive volume of gas or liquid, e.g., LAr, to perform a 3D reconstruction of a particle trajectory or interaction. The activity is recorded by digitizing the waveforms of current induced on the anode as the distribution of ionization charge passes by or is collected on the electrode. (2) TPC is also used in LBNF/DUNE-US for "total project cost". 15, 49, 52, 63

Technology Readiness Level (TRL) A method for estimating the maturity of technologies.. 60

vertical drift single-phase, vertical drift LArTPC technology. 13, 16, 29, 30, 37, 39, 42, 59, 62, 64

VUV vacuum ultra-violet. 45–49, 52, 61, 79

Water-based Liquid Scintillator (WbLS) A scintillating material consisting of water loaded with liquid scintillator.. 56, 82

Water-based Near Detector (WbND) A possible DUNE Phase II near detector sub-system employing water as neutrino target.. 81, 82

weakly-interacting massive particle (WIMP) A hypothesized particle that may be a component of dark matter. 21, 25, 59

wavelength-shifting (WLS) A material or process by which incident photons are absorbed by a material and photons are emitted at a different, typically longer, wavelength. 34, 37, 38, 71

X-ARAPUCA Extended design with WLS coating on only the external face of the dichroic filter window(s) but with a WLS doped plate inside the cell. 32–35, 37, 38, 49, 62, 63

References

[1] T. Nakada *et al.*, "The European Strategy for Particle Physics Update 2013. La stratégie européenne pour la physique des particules Mise à jour 2013. 16th Session of European Strategy Council,". `https://cds.cern.ch/record/1567258`.

[2] S. Ritz, H. Aihara, M. Breidenbach, B. Cousins, A. de Gouvea, M. Demarteau, *et al.*, "Building for discovery: strategic plan for us particle physics in the global context." 2014. HEPAP Subcommittee.

[3] S. Asai *et al.*, "Exploring the quantum universe: Pathways to innovation and discovery in particle physics." 2023. `https://www.usparticlephysics.org/2023-p5-report`. HEPAP P5 Subcommittee.

[4] European Strategy Group, "2020 Update of the European Strategy for Particle Physics (Brochure)," CERN-ESU-015. `https://cds.cern.ch/record/2721370`.

[5] **DUNE** Collaboration, V. Hewes *et al.*, "Deep Underground Neutrino Experiment (DUNE) Near Detector Conceptual Design Report," *Instruments* **5** no. 4, (2021) 31, `arXiv:2103.13910 [physics.ins-det]`.

[6] **DUNE** Collaboration, B. Abi *et al.*, "Deep Underground Neutrino Experiment (DUNE), Far Detector Technical Design Report, Volume IV: Far Detector Single-phase Technology," *JINST* **15** no. 08, (2020) T08010, `arXiv:2002.03010 [physics.ins-det]`.

[7] R. Ainsworth *et al.*, "Report from the Fermilab Proton Intensity Upgrade Central Design Group,".

[8] **DUNE** Collaboration, B. Abi *et al.*, "Long-baseline neutrino oscillation physics potential of the DUNE experiment," *Eur. Phys. J. C* **80** no. 10, (2020) 978, `arXiv:2006.16043 [hep-ex]`.

[9] **Daya Bay** Collaboration, F. P. An *et al.*, "Precision Measurement of Reactor Antineutrino Oscillation at Kilometer-Scale Baselines by Daya Bay," *Phys. Rev. Lett.* **130** no. 16, (2023) 161802, `arXiv:2211.14988 [hep-ex]`.

[10] **JUNO** Collaboration, A. Abusleme *et al.*, "Sub-percent precision measurement of neutrino oscillation parameters with JUNO," *Chin. Phys. C* **46** no. 12, (2022) 123001, `arXiv:2204.13249 [hep-ex]`.

[11] **Super-Kamiokande** Collaboration, M. Jiang *et al.*, "Atmospheric Neutrino Oscillation Analysis with Improved Event Reconstruction in Super-Kamiokande IV," *PTEP* **2019** no. 5, (2019) 053F01, `arXiv:1901.03230 [hep-ex]`.

[12] **Theia** Collaboration, M. Askins *et al.*, "THEIA: an advanced optical neutrino detector," *Eur. Phys. J. C* **80** no. 5, (2020) 416, `arXiv:1911.03501 [physics.ins-det]`.

[13] **DUNE** Collaboration, B. Abi *et al.*, "Deep Underground Neutrino Experiment (DUNE), Far Detector Technical Design Report, Volume II: DUNE Physics," `arXiv:2002.03005 [hep-ex]`.

[14] J.-S. Lu, Y.-F. Li, and S. Zhou, "Getting the most from the detection of galactic supernova neutrinos in future large liquid-scintillator detectors," *Phys. Rev. D* **94** (Jul, 2016) 023006. `https://link.aps.org/doi/10.1103/PhysRevD.94.023006`.

[15] **Hyper-Kamiokande** Collaboration, K. Abe *et al.*, "Supernova Model Discrimination with Hyper-Kamiokande," *Astrophys. J.* **916** no. 1, (2021) 15, `arXiv:2101.05269 [astro-ph.IM]`.

[16] R. F. Lang, C. McCabe, S. Reichard, M. Selvi, and I. Tamborra, "Supernova neutrino physics with xenon dark matter detectors: A timely perspective," *Phys. Rev. D* **94** no. 10, (2016) 103009, `arXiv:1606.09243 [astro-ph.HE]`.

[17] **DarkSide 20k** Collaboration, P. Agnes *et al.*, "Sensitivity of future liquid argon dark matter search experiments to core-collapse supernova neutrinos," *JCAP* **03** (2021) 043, `arXiv:2011.07819 [astro-ph.HE]`.

[18] **The MicroBooNE Collaboration** Collaboration, P. Abratenko *et al.*, "Measurement of ambient radon progeny decay rates and energy spectra in liquid argon using the microboone detector," *Phys. Rev. D* **109** (Mar, 2024) 052007. `https://link.aps.org/doi/10.1103/PhysRevD.109.052007`.

[19] T. Bezerra *et al.*, "Large low background kTon-scale liquid argon time projection chambers," *J. Phys. G* **50** no. 6, (2023) 060502, `arXiv:2301.11878 [hep-ex]`.

[20] **DUNE** Collaboration, B. Abi *et al.*, "Supernova neutrino burst detection with the Deep Underground Neutrino Experiment," *Eur. Phys. J. C* **81** no. 5, (2021) 423, `arXiv:2008.06647 [hep-ex]`.

[21] L. Hüdepohl, B. Müller, H.-T. Janka, A. Marek, and G. G. Raffelt, "Neutrino signal of electron-capture supernovae from core collapse to cooling," *Phys. Rev. Lett.* **104** (Jun, 2010) 251101. `https://link.aps.org/doi/10.1103/PhysRevLett.104.251101`.

[22] **DUNE** Collaboration, A. Abed Abud *et al.*, "Impact of cross-section uncertainties on supernova neutrino spectral parameter fitting in the Deep Underground Neutrino Experiment," *Phys. Rev. D* **107** no. 11, (2023) 112012, `arXiv:2303.17007 [hep-ex]`.

[23] **DUNE** Collaboration, A. Abed Abud *et al.*, "Supernova Pointing Capabilities of DUNE," `arXiv:2407.10339 [hep-ex]`.

[24] **SNEWS** Collaboration, S. Al Kharusi *et al.*, "SNEWS 2.0: a next-generation supernova early warning system for multi-messenger astronomy," *New J. Phys.* **23** no. 3, (2021) 031201, `arXiv:2011.00035 [astro-ph.HE]`.

[25] B. Dasgupta and A. Dighe, "Collective three-flavor oscillations of supernova neutrinos," *Phys. Rev. D* **77** (2008) 113002, `arXiv:0712.3798 [hep-ph]`.

[26] P.-W. Chang, I. Esteban, J. F. Beacom, T. A. Thompson, and C. M. Hirata, "Toward Powerful Probes of Neutrino Self-Interactions in Supernovae," *Phys. Rev. Lett.* **131** no. 7, (2023) 071002, `arXiv:2206.12426 [hep-ph]`.

[27] F. Pompa, F. Capozzi, O. Mena, and M. Sorel, "Absolute ν Mass Measurement with the DUNE Experiment," *Phys. Rev. Lett.* **129** no. 12, (2022) 121802, `arXiv:2203.00024 [hep-ph]`.

[28] N. Ekanger, S. Horiuchi, H. Nagakura, and S. Reitz, "Diffuse supernova neutrino background with up-to-date star formation rate measurements and long-term multidimensional supernova simulations," *Phys. Rev. D* **109** (Jan, 2024) 023024. `https://link.aps.org/doi/10.1103/PhysRevD.109.023024`.

[29] L. Hudepohl, B. Muller, H. T. Janka, A. Marek, and G. G. Raffelt, "Neutrino Signal of Electron-Capture Supernovae from Core Collapse to Cooling," *Phys. Rev. Lett.* **104** (2010) 251101, `arXiv:0912.0260 [astro-ph.SR]`. [Erratum: Phys.Rev.Lett. 105, 249901 (2010)].

[30] M. Mukhopadhyay, C. Lunardini, F. X. Timmes, and K. Zuber, "Presupernova neutrinos: Directional sensitivity and prospects for progenitor identification," *The Astrophysical Journal* **899** no. 2, (Aug, 2020) 153. `https://dx.doi.org/10.3847/1538-4357/ab99a6`.

[31] F. Capozzi, S. W. Li, G. Zhu, and J. F. Beacom, "DUNE as the Next-Generation Solar Neutrino Experiment," *Phys. Rev. Lett.* **123** no. 13, (2019) 131803, `arXiv:1808.08232 [hep-ph]`.

[32] **Super-Kamiokande** Collaboration, K. Abe *et al.*, "Solar neutrino measurements using the full data period of Super-Kamiokande-IV," *Phys. Rev. D* **109** no. 9, (2024) 092001, `arXiv:2312.12907 [hep-ex]`.

[33] A. Y. Smirnov, "The MSW effect and matter effects in neutrino oscillations," *Phys. Scripta T* **121** (2005) 57–64, `arXiv:hep-ph/0412391`.

[34] C. A. J. O'Hare, "New Definition of the Neutrino Floor for Direct Dark Matter Searches," *Phys. Rev. Lett.* **127** no. 25, (2021) 251802, `arXiv:2109.03116 [hep-ph]`.

[35] L. Baudis, "DARWIN/XLZD: A future xenon observatory for dark matter and other rare interactions," *Nucl. Phys. B* **1003** (2024) 116473, `arXiv:2404.19524 [astro-ph.IM]`.

[36] **DarkSide** Collaboration, P. Agnes, "Direct Detection of Dark Matter with DarkSide-20k," *EPJ Web Conf.* **280** (2023) 06003.

[37] E. Church, C. M. Jackson, and R. Saldanha, "Dark matter detection capabilities of a large multipurpose Liquid Argon Time Projection Chamber," *JINST* **15** no. 09, (2020) P09026, `arXiv:2005.04824 [physics.ins-det]`.

[38] C. Adams *et al.*, "Neutrinoless Double Beta Decay," `arXiv:2212.11099 [nucl-ex]`.

[39] **SNO+** Collaboration, S. Andringa *et al.*, "Current Status and Future Prospects of the SNO+ Experiment," *Adv. High Energy Phys.* **2016** (2016) 6194250, `arXiv:1508.05759 [physics.ins-det]`.

[40] **KamLAND-Zen** Collaboration, S. Abe *et al.*, "Search for Majorana Neutrinos with the Complete KamLAND-Zen Dataset," `arXiv:2406.11438 [hep-ex]`.

[41] A. Mastbaum, F. Psihas, and J. Zennamo, "Xenon-doped liquid argon TPCs as a neutrinoless double beta decay platform," *Phys. Rev. D* **106** no. 9, (2022) 092002, `arXiv:2203.14700 [hep-ex]`.

[42] **nEXO** Collaboration, G. Adhikari *et al.*, "nEXO: neutrinoless double beta decay search beyond 10^{28} year half-life sensitivity," *J. Phys. G* **49** no. 1, (2022) 015104, `arXiv:2106.16243 [nucl-ex]`.

[43] **DUNE** Collaboration, B. Abi *et al.*, "Prospects for beyond the Standard Model physics searches at the Deep Underground Neutrino Experiment," *Eur. Phys. J. C* **81** no. 4, (2021) 322, `arXiv:2008.12769 [hep-ex]`.

[44] P. Coloma, E. Fernández-Martínez, M. González-López, J. Hernández-García, and Z. Pavlovic, "GeV-scale neutrinos: interactions with mesons and DUNE sensitivity," *Eur. Phys. J. C* **81** no. 1, (2021) 78, `arXiv:2007.03701 [hep-ph]`.

[45] E. Fernández-Martínez, M. González-López, J. Hernández-García, M. Hostert, and J. López-Pavón, "Effective portals to heavy neutral leptons," *JHEP* **09** (2023) 001, `arXiv:2304.06772 [hep-ph]`.

[46] P. Coloma, J. Martín-Albo, and S. Urrea, "Discovering long-lived particles at DUNE," *Phys. Rev. D* **109** no. 3, (2024) 035013, `arXiv:2309.06492 [hep-ph]`.

[47] I. Krasnov, "DUNE prospects in the search for sterile neutrinos," *Phys. Rev. D* **100** no. 7, (2019) 075023, `arXiv:1902.06099 [hep-ph]`.

[48] P. Ballett, T. Boschi, and S. Pascoli, "Heavy Neutral Leptons from low-scale seesaws at the DUNE Near Detector," *JHEP* **03** (2020) 111, `arXiv:1905.00284 [hep-ph]`.

[49] J. M. Berryman, A. de Gouvea, P. J. Fox, B. J. Kayser, K. J. Kelly, and J. L. Raaf, "Searches for Decays of New Particles in the DUNE Multi-Purpose Near Detector," *JHEP* **02** (2020) 174, `arXiv:1912.07622 [hep-ph]`.

[50] M. Breitbach, L. Buonocore, C. Frugiuele, J. Kopp, and L. Mittnacht, "Searching for physics beyond the Standard Model in an off-axis DUNE near detector," *JHEP* **01** (2022) 048, `arXiv:2102.03383 [hep-ph]`.

[51] K. J. Kelly, S. Kumar, and Z. Liu, "Heavy axion opportunities at the DUNE near detector," *Phys. Rev. D* **103** no. 9, (2021) 095002, `arXiv:2011.05995 [hep-ph]`.

[52] W. Altmannshofer, S. Gori, M. Pospelov, and I. Yavin, "Neutrino Trident Production: A Powerful Probe of New Physics with Neutrino Beams," *Phys. Rev. Lett.* **113** (2014) 091801, `arXiv:1406.2332 [hep-ph]`.

[53] P. Ballett, M. Hostert, S. Pascoli, Y. F. Perez-Gonzalez, Z. Tabrizi, and R. Zukanovich Funchal, "Z's in neutrino scattering at DUNE," *Phys. Rev. D* **100** no. 5, (2019) 055012, `arXiv:1902.08579 [hep-ph]`.

[54] P. Ballett, M. Hostert, S. Pascoli, Y. F. Perez-Gonzalez, Z. Tabrizi, and R. Zukanovich Funchal, "Neutrino Trident Scattering at Near Detectors," *JHEP* **01** (2019) 119, `arXiv:1807.10973 [hep-ph]`.

[55] W. Altmannshofer, S. Gori, J. Martín-Albo, A. Sousa, and M. Wallbank, "Neutrino Tridents at DUNE," *Phys. Rev. D* **100** no. 11, (2019) 115029, `arXiv:1902.06765 [hep-ph]`.

[56] A. De Gouvêa, K. J. Kelly, G. V. Stenico, and P. Pasquini, "Physics with Beam Tau-Neutrino Appearance at DUNE," *Phys. Rev. D* **100** no. 1, (2019) 016004, `arXiv:1904.07265 [hep-ph]`.

[57] A. Ghoshal, A. Giarnetti, and D. Meloni, "On the role of the ν_τ appearance in DUNE in constraining standard neutrino physics and beyond," *JHEP* **12** (2019) 126, `arXiv:1906.06212 [hep-ph]`.

[58] J. Rout, S. Roy, M. Masud, M. Bishai, and P. Mehta, "Impact of high energy beam tunes on the sensitivities to the standard unknowns at DUNE," *Phys. Rev. D* **102** (2020) 116018, `arXiv:2009.05061 [hep-ph]`.

[59] **NOMAD** Collaboration, P. Astier *et al.*, "Final NOMAD results on muon-neutrino —> tau-neutrino and electron-neutrino —> tau-neutrino oscillations including a new search for tau-neutrino appearance using hadronic tau decays," *Nucl. Phys. B* **611** (2001) 3–39, `arXiv:hep-ex/0106102`.

[60] **DUNE** Collaboration, A. Abed Abud *et al.*, "The DUNE Far Detector Vertical Drift Technology, Technical Design Report," `arXiv:2312.03130 [hep-ex]`.

[61] **DUNE** Collaboration, B. Abi *et al.*, "The DUNE Far Detector Interim Design Report, Volume 3: Dual-Phase Module," `arXiv:1807.10340 [physics.ins-det]`.

[62] **DUNE** Collaboration, A. A. Abud *et al.*, "Design, construction and operation of the ProtoDUNE-SP Liquid Argon TPC," *JINST* **17** no. 01, (2022) P01005, `arXiv:2108.01902 [physics.ins-det]`.

[63] A. Machado, E. Segreto, D. Warner, A. Fauth, B. Gelli, R. Maximo, A. Pissolatti, L. Paulucci, and F. Marinho, "The x-arapuca: an improvement of the arapuca device," *Journal of instrumentation* **13** no. 04, (2018) C04026.

[64] C. Brizzolari *et al.*, "Enhancement of the X-Arapuca photon detection device for the DUNE experiment," *JINST* **16** no. 09, (2021) P09027, `arXiv:2104.07548 [physics.ins-det]`.

[65] M. A. Arroyave *et al.*, "Characterization and Novel Application of Power Over Fiber for Electronics in a Harsh Environment," `arXiv:2405.16816 [physics.ins-det]`.

[66] D. A. Dwyer *et al.*, "LArPix: Demonstration of low-power 3D pixelated charge readout for liquid argon time projection chambers," *JINST* **13** no. 10, (2018) P10007, `arXiv:1808.02969 [physics.ins-det]`.

[67] **DUNE** Collaboration, A. Abed Abud *et al.*, "Performance of a modular ton-scale pixel-readout liquid argon time projection chamber," `arXiv:2403.03212 [physics.ins-det]`.

[68] D. Nygren and Y. Mei, "Q-Pix: Pixel-scale Signal Capture for Kiloton Liquid Argon TPC Detectors: Time-to-Charge Waveform Capture, Local Clocks, Dynamic Networks," `arXiv:1809.10213 [physics.ins-det]`.

[69] P. Miao, J. Asaadi, J. B. R. Battat, M. Han, K. Keefe, S. Kohani, A. D. McDonald, D. Nygren, O. Seidel, and Y. Mei, "Demonstrating the Q-Pix front-end using discrete OpAmp and CMOS transistors," `arXiv:2311.09568 [physics.ins-det]`.

[70] C. Adams, M. Del Tutto, J. Asaadi, M. Bernstein, E. Church, R. Guenette, J. M. Rojas, H. Sullivan, and A. Tripathi, "Enhancing neutrino event reconstruction with pixel-based 3D readout for liquid argon time projection chambers," *JINST* **15** no. 04, (2020) P04009, `arXiv:1912.10133 [physics.ins-det]`.

[71] **Q-Pix** Collaboration, S. Kubota *et al.*, "Enhanced low-energy supernova burst detection in large liquid argon time projection chambers enabled by Q-Pix," *Phys. Rev. D* **106** no. 3, (2022) 032011, `arXiv:2203.12109 [hep-ex]`.

[72] D. Hollywood *et al.*, "ARIADNE—A novel optical LArTPC: technical design report and initial characterisation using a secondary beam from the CERN PS and cosmic muons," *JINST* **15** no. 03, (2020) P03003, `arXiv:1910.03406 [physics.ins-det]`.

[73] A. Lowe, K. Majumdar, K. Mavrokoridis, B. Philippou, A. Roberts, C. Touramanis, and J. Vann, "Optical Readout of the ARIADNE LArTPC using a Timepix3-based Camera," *Instruments* **4** no. 4, (2020) 35, `arXiv:2011.02292 [physics.ins-det]`.

[74] A. Roberts *et al.*, "First demonstration of 3D optical readout of a TPC using a single photon sensitive Timepix3 based camera," *JINST* **14** no. 06, (2019) P06001, `arXiv:1810.09955 [physics.ins-det]`.

[75] P. Amedo, D. Gonzalez-Dıaz, *et al.*, "Letter of Intent: Large-scale demonstration of the ARIADNE LArTPC optical readout system at the CERN Neutrino Platform," tech. rep., CERN, Geneva, 2020. `https://cds.cern.ch/record/2739360`.

[76] A. Lowe, K. Majumdar, K. Mavrokoridis, B. Philippou, A. Roberts, and C. Touramanis, "A Novel Manufacturing Process for Glass THGEMs and First Characterisation in an Optical Gaseous Argon TPC," *Appl. Sciences* **11** no. 20, (2021) 9450, `arXiv:2109.02910 [physics.ins-det]`.

[77] A. J. Lowe *et al.*, "ARIADNE$^+$: Large Scale Demonstration of Fast Optical Readout for Dual-Phase LArTPCs at the CERN Neutrino Platform †," *Phys. Sci. Forum* **8** no. 1, (2023) 46, `arXiv:2301.02530 [physics.ins-det]`.

[78] M. Fiorini, J. Alozy, M. Bolognesi, M. Campbell, A. C. Ramusino, X. LLopart, T. Michel, S. F. Schifano, A. Tremsin, and J. Vallerga, "Single-photon imaging detector with O (10) ps timing and sub-10 μm position resolutions," *JINST* **13** no. 12, (2018) C12005.

[79] S. Parsa *et al.*, "SoLAr: Solar Neutrinos in Liquid Argon," in *Snowmass 2021*. 3, 2022. `arXiv:2203.07501 [hep-ex]`.

[80] N. Anfimov *et al.*, "First Demonstration of a Combined Light and Charge Pixel Readout on the Anode Plane of a LArTPC," `arXiv:2406.14121 [hep-ex]`.

[81] K. Kubodera and T.-S. Park, "The Solar HEP process," *Ann. Rev. Nucl. Part. Sci.* **54** (2004) 19–37, `arXiv:nucl-th/0402008`.

[82] M. Rooks, S. Abbaszadeh, J. Asaadi, M. Febbraro, R. W. Gladen, E. Gramellini, K. Hellier, F. M. Blaszczyk, and A. D. McDonald, "Development of a novel, windowless, amorphous selenium based photodetector for use in liquid noble detectors," *JINST* **18** no. 01, (2023) P01029, `arXiv:2207.11127 [physics.ins-det]`.

[83] A. Friedland and S. W. Li, "Understanding the energy resolution of liquid argon neutrino detectors," *Phys. Rev. D* **99** no. 3, (2019) 036009, `arXiv:1811.06159 [hep-ph]`.

[84] S. Andringa *et al.*, "Low-energy physics in neutrino LArTPCs," *J. Phys. G* **50** no. 3, (2023) 033001.

[85] **DUNE** Collaboration, N. Gallice, "Xenon doping of liquid argon in ProtoDUNE single phase," *JINST* **17** no. 01, (2022) C01034, `arXiv:2111.00347 [physics.ins-det]`.

[86] E. P. Bernard *et al.*, "Thermodynamic stability of xenon-doped liquid argon detectors," *Phys. Rev. C* **108** no. 4, (2023) 045503, `arXiv:2209.05435 [physics.ins-det]`.

[87] M. J. Dolinski, A. W. P. Poon, and W. Rodejohann, "Neutrinoless Double-Beta Decay: Status and Prospects," *Ann. Rev. Nucl. Part. Sci.* **69** (2019) 219–251, `arXiv:1902.04097 [nucl-ex]`.

[88] A. Avasthi *et al.*, "Kiloton-scale xenon detectors for neutrinoless double beta decay and other new physics searches," *Phys. Rev. D* **104** no. 11, (2021) 112007, `arXiv:2110.01537 [physics.ins-det]`.

[89] P. Cennini *et al.*, "Improving the performance of the liquid argon TPC by doping with tetramethyl germanium," *Nucl. Instrum. Meth. A* **355** (1995) 660–662.

[90] **EXO-200** Collaboration, G. Anton *et al.*, "Measurement of the scintillation and ionization response of liquid xenon at MeV energies in the EXO-200 experiment," *Phys. Rev. C* **101** no. 6, (2020) 065501, `arXiv:1908.04128 [physics.ins-det]`.

[91] **LArIAT** Collaboration, W. Foreman *et al.*, "Calorimetry for low-energy electrons using charge and light in liquid argon," *Phys. Rev. D* **101** no. 1, (2020) 012010, `arXiv:1909.07920 [physics.ins-det]`.

[92] D. F. Anderson, "New Photosensitive Dopants for Liquid Argon," *Nucl. Instrum. Meth. A* **245** (1986) 361.

[93] M. Yeh, S. Hans, W. Beriguete, R. Rosero, L. Hu, R. L. Hahn, M. V. Diwan, D. E. Jaffe, S. H. Kettell, and L. Littenberg, "A new water-based liquid scintillator and potential applications," *Nucl. Instrum. Meth. A* **660** (2011) 51–56.

[94] A. Latorre and S. Seibert, "Chroma: Ultra-fast Photon Monte Carlo," `https://www.tlatorre.com/chroma/`.

[95] T. Kaptanoglu, M. Luo, and J. Klein, "Cherenkov and Scintillation Light Separation Using Wavelength in LAB Based Liquid Scintillator," *JINST* **14** no. 05, (2019) T05001, `arXiv:1811.11587 [physics.ins-det]`.

[96] J. Caravaca, F. B. Descamps, B. J. Land, M. Yeh, and G. D. Orebi Gann, "Cherenkov and Scintillation Light Separation in Organic Liquid Scintillators," *Eur. Phys. J. C* **77** no. 12, (2017) 811, `arXiv:1610.02011 [physics.ins-det]`.

[97] M. J. Minot, M. A. Popecki, and M. J. Wetstein, "Large Area Picosecond Photodetector (LAPPD) Performance Test Results," in *2018 IEEE Nuclear Science Symposium and Medical Imaging Conference*. 11, 2018.

[98] A. V. Lyashenko *et al.*, "Performance of Large Area Picosecond Photo-Detectors (LAPPD^{TM})," *Nucl. Instrum. Meth. A* **958** (2020) 162834, `arXiv:1909.10399 [physics.ins-det]`.

[99] Z. Guo, M. Yeh, R. Zhang, D.-W. Cao, M. Qi, Z. Wang, and S. Chen, "Slow Liquid Scintillator Candidates for MeV-scale Neutrino Experiments," *Astropart. Phys.* **109** (2019) 33–40, `arXiv:1708.07781 [physics.ins-det]`.

[100] S. D. Biller, E. J. Leming, and J. L. Paton, "Slow fluors for effective separation of Cherenkov light in liquid scintillators," *Nucl. Instrum. Meth. A* **972** (2020) 164106, `arXiv:2001.10825 [physics.ins-det]`.

[101] J. R. Klein *et al.*, "Future Advances in Photon-Based Neutrino Detectors: A SNOWMASS White Paper," `arXiv:2203.07479 [physics.ins-det]`.

[102] T. Anderson *et al.*, "Eos: conceptual design for a demonstrator of hybrid optical detector technology," *JINST* **18** no. 02, (2023) P02009, `arXiv:2211.11969 [physics.ins-det]`.

[103] **ANNIE** Collaboration, A. R. Back *et al.*, "Accelerator Neutrino Neutron Interaction Experiment (ANNIE): Preliminary Results and Physics Phase Proposal," `arXiv:1707.08222 [physics.ins-det]`.

[104] G. Zhu, S. W. Li, and J. F. Beacom, "Developing the MeV potential of DUNE: Detailed considerations of muon-induced spallation and other backgrounds," *Phys. Rev. C* **99** no. 5, (2019) 055810, `arXiv:1811.07912 [hep-ph]`.

[105] **DarkSide** Collaboration, P. Agnes *et al.*, "DarkSide-50 532-day Dark Matter Search with Low-Radioactivity Argon," *Phys. Rev. D* **98** no. 10, (2018) 102006, `arXiv:1802.07198 [astro-ph.CO]`.

[106] S. S. Poudel, B. Loer, R. Saldanha, B. R. Hackett, and H. O. Back, "Subsurface cosmogenic and radiogenic production of ^{42}Ar," `arXiv:2309.16169 [physics.ins-det]`.

[107] L. Consiglio, "The cryogenic electronics for Dark Side-20k SiPM readout," *JINST* **15** no. 05, (2020) C05063.

[108] K. Scholberg, "The CEvNS Glow from a Supernova." Sept., 2019. `https://zenodo.org/records/3464639`.

[109] **DUNE** Collaboration, A. Abed Abud *et al.*, "A Gaseous Argon-Based Near Detector to Enhance the Physics Capabilities of DUNE," `arXiv:2203.06281 [hep-ex]`.

[110] A. Saá-Hernández *et al.*, "On the determination of the interaction time of GeV neutrinos in large argon gas TPCs," `arXiv:2401.09920 [physics.ins-det]`.

[111] A. Ritchie-Yates *et al.*, "First operation of an ALICE OROC operated in high pressure Ar-CO$_2$ and Ar-CH$_4$," *Eur. Phys. J. C* **83** no. 12, (2023) 1139, `arXiv:2305.08822 [physics.ins-det]`.

[112] **DUNE** Collaboration, T. A. Mohayai, "TPC Test-stands: An Overview & Future Prospects,".

[113] X. G. Lu, D. Coplowe, R. Shah, G. Barr, D. Wark, and A. Weber, "Reconstruction of Energy Spectra of Neutrino Beams Independent of Nuclear Effects," *Phys. Rev. D* **92** no. 5, (2015) 051302, `arXiv:1507.00967 [hep-ex]`.

[114] C. Grupen, "Physics of particle detection," *AIP Conf. Proc.* **536** no. 1, (2000) 3–34, `arXiv:physics/9906063`.

[115] J. Alme *et al.*, "The ALICE TPC, a large 3-dimensional tracking device with fast readout for ultra-high multiplicity events," *Nucl. Instrum. Meth. A* **622** (2010) 316–367, `arXiv:1001.1950 [physics.ins-det]`.

[116] P. Amedo, R. Hafeji, A. Roberts, A. Lowe, S. Ravinthiran, S. Leardini, K. Majumdar, K. Mavrokoridis, and D. González-Díaz, "Scintillation of Ar/CF_4 mixtures: glass-THGEM characterization with 1% CF_4 at 1–1.5 bar," *JINST* **19** no. 05, (2024) C05001, `arXiv:2312.07503 [physics.ins-det]`.

[117] M. Kuźniak *et al.*, "Development of very-thick transparent GEMs with wavelength-shifting capability for noble element TPCs," *Eur. Phys. J. C* **81** no. 7, (2021) 609, `arXiv:2106.03773 [physics.ins-det]`.

[118] S. Leardini *et al.*, "FAT-GEMs: (Field Assisted) Transparent Gaseous-Electroluminescence Multipliers," *Sci. Technol.* **2** (2024) 1373235, `arXiv:2401.09905 [physics.ins-det]`.

[119] S. Leardini, Y. Zhou, A. Tesi, M. Morales, D. González-Díaz, A. Breskin, S. Bressler, L. Moleri, and V. Peskov, "Diamond-like carbon coatings for cryogenic operation of particle detectors," *Nucl. Instrum. Meth. A* **1049** (2023) 168104, `arXiv:2209.15509 [physics.ins-det]`.

[120] A. Tesi, S. Leardini, L. Moleri, D. Gonzalez-Diaz, A. Jash, A. Breskin, and S. Bressler, "The cryogenic RWELL: a stable charge multiplier for dual-phase liquid argon detectors," *Eur. Phys. J. C* **83** no. 10, (2023) 979, `arXiv:2307.02343 [physics.ins-det]`.

[121] L. K. Emberger, *Precision Timing in Highly Granular Calorimeters and Applications in Long Baseline Neutrino and Lepton Collider Experiments.* PhD dissertation, Technische Universität München, School of Natural Sciences, 2022. `http://d-nb.info/1278551751/34`.

[122] **CALICE** Collaboration, F. Sefkow and F. Simon, "A highly granular SiPM-on-tile calorimeter prototype," *J. Phys. Conf. Ser.* **1162** no. 1, (2019) 012012, `arXiv:1808.09281 [physics.ins-det]`.

[123] Z. Yuan, K. Briggl, H. Chen, Y. Munwes, H.-C. Schultz-Coulon, and W. Shen, "KLauS: A Low-power SiPM Readout ASIC for Highly Granular Calorimeters," in *2019 IEEE Nuclear Science Symposium (NSS) and Medical Imaging Conference (MIC)*, pp. 1–4. 2019.

[124] A. Bersani *et al.*, "A Complete Magnetic Design and Improved Mechanical Project for the DUNE ND-GAr Solenoid Magnet," *IEEE Trans. Appl. Supercond.* **32** no. 6, (2022) 4500204.

[125] K. Saito, H. Tawara, T. Sanami, E. Shibamura, and S. Sasaki, "Absolute number of scintillation photons emitted by alpha-particles in rare gases," *IEEE Trans. Nucl. Sci.* **49** (2002) 1674–1680.

[126] R. Santorelli, E. Sanchez Garcia, P. G. Abia, D. González-Díaz, R. L. Manzano, J. J. M. Morales, V. Pesudo, and L. Romero, "Spectroscopic analysis of the gaseous argon scintillation with a wavelength sensitive particle detector," *Eur. Phys. J. C* **81** no. 7, (2021) 622, arXiv:2012.08262 [physics.ins-det].

[127] D. Gonzalez-Diaz, F. Monrabal, and S. Murphy, "Gaseous and dual-phase time projection chambers for imaging rare processes," *Nucl. Instrum. Meth. A* **878** (2018) 200–255, arXiv:1710.01018 [physics.ins-det].

[128] P. Amedo, S. Leardini, A. Saá-Hernández, D. González, and D. González-Díaz, "Primary scintillation yields of α particles in pressurized Argon-CF_4 mixtures," https://indico.physics.ucsd.edu/event/1/contributions/62/. In preparation, preliminary results in LIDINE 2021.

[129] P. Amedo, D. González-Díaz, F. M. Brunbauer, D. J. Fernández-Posada, E. Oliveri, and L. Ropelewski, "Observation of strong wavelength-shifting in the argon-tetrafluoromethane system," arXiv:2306.09919 [physics.ins-det]. https://www.frontiersin.org/articles/10.3389/fdest.2023.1282854/full.

[130] M. D'Incecco, C. Galbiati, G. K. Giovanetti, G. Korga, X. Li, A. Mandarano, A. Razeto, D. Sablone, and C. Savarese, "Development of a Novel Single-Channel, 24 cm^2, SiPM-Based, Cryogenic Photodetector," *IEEE Trans. Nucl. Sci.* **65** no. 1, (2017) 591–596, arXiv:1706.04220 [physics.ins-det].

[131] M. Blatnik *et al.*, "Performance of a Quintuple-GEM Based RICH Detector Prototype," *IEEE Trans. Nucl. Sci.* **62** no. 6, (2015) 3256–3264, arXiv:1501.03530 [physics.ins-det].

[132] B. Bersani, Andrea, B. Alan D., *et al.*, "SPY: A Magnet System for a High-pressure Gaseous TPC Neutrino Detector," arXiv:2311.16063 [hep-ex].

[133] R. Petti, "Probing free nucleons with (anti)neutrinos," *Phys. Lett. B* **834** (2022) 137469, arXiv:2205.10396 [hep-ph].

[134] R. Petti, "Precision Measurements of Fundamental Interactions with (Anti)Neutrinos," in *27th International Workshop on Deep Inelastic Scattering and Related Subjects*. 10, 2019. `arXiv:1910.05995 [hep-ex]`.

[135] H. Duyang, B. Guo, S. R. Mishra, and R. Petti, "A Precise Determination of (Anti)neutrino Fluxes with (Anti)neutrino-Hydrogen Interactions," *Phys. Lett. B* **795** (2019) 424–431, `arXiv:1902.09480 [hep-ph]`.

[136] R. Petti, "An Oxygen Target for (Anti)neutrinos," `arXiv:2301.04744 [hep-ex]`.

[137] R. L. Talaga, J. J. Grudzinski, S. Phan-Budd, A. Pla-Dalmau, J. E. Fagan, C. Grozis, and K. M. Kephart, "PVC Extrusion Development and Production for the NOvA Neutrino Experiment," *Nucl. Instrum. Meth. A* **861** (2017) 77–89, `arXiv:1601.00908 [physics.ins-det]`.

[138] **LiquidO** Collaboration, A. Cabrera *et al.*, "Neutrino Physics with an Opaque Detector," *Commun. Phys.* **4** (2021) 273, `arXiv:1908.02859 [physics.ins-det]`.

[139] A. Cabrera, J. Hartnell, and J. Ochoa-Ricoux, "Liquido: an appetizer." 2019. `https://indico.fnal.gov/event/21535/contributions/63272/attachments/39670/48008/LiquidO_MOD2019_OchoaRicoux.pdf`.